



**Characterization of Ultra-high Temperature Ceramics
via Transmission Electron Microscopy Relevant ZrB₂-
based composites, TaC-based composites and oxides
containing SiC chopped fibers**

**Laura Silverstroni
Diletta Sciti**

**Institute of Science and Technology for Ceramics
Via Granarolo 64
FAENZA, 48018 ITALY**

EOARD GRANT #FA8655-12-1-3004

Report Date: March 2015

Final Report from 8 December 2013 to 07 March 2015

Distribution Statement A: Approved for public release distribution is unlimited.

**Air Force Research Laboratory
Air Force Office of Scientific Research
European Office of Aerospace Research and Development
Unit 4515, APO AE 09421-4515**

REPORT DOCUMENTATION PAGE

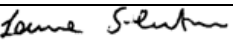
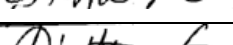
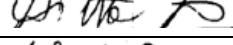
Form Approved OMB No. 0704-0188

Public reporting burden for this collection of information is estimated to average 1 hour per response, including the time for reviewing instructions, searching existing data sources, gathering and maintaining the data needed, and completing and reviewing the collection of information. Send comments regarding this burden estimate or any other aspect of this collection of information, including suggestions for reducing the burden, to Department of Defense, Washington Headquarters Services, Directorate for Information Operations and Reports (0704-0188), 1215 Jefferson Davis Highway, Suite 1204, Arlington, VA 22202-4302. Respondents should be aware that notwithstanding any other provision of law, no person shall be subject to any penalty for failing to comply with a collection of information if it does not display a currently valid OMB control number.

PLEASE DO NOT RETURN YOUR FORM TO THE ABOVE ADDRESS.

1. REPORT DATE (DD-MM-YYYY) 6 March 2015			2. REPORT TYPE Final Report		3. DATES COVERED (From – To) 8 December 2013 – 7 March 2015	
4. TITLE AND SUBTITLE Characterization of Ultra-high Temperature Ceramics via Transmission Electron Microscopy Relevant ZrB₂-based composites, TaC-based composites and oxides containing SiC chopped fibers			5a. CONTRACT NUMBER 5b. GRANT NUMBER FA8655-12-1-3004			
			5c. PROGRAM ELEMENT NUMBER 61102F			
6. AUTHOR(S) Laura Silverstroni Diletta Sciti			5d. PROJECT NUMBER 5d. TASK NUMBER 5e. WORK UNIT NUMBER			
7. PERFORMING ORGANIZATION NAME(S) AND ADDRESS(ES) Institute of Science and Technology for Ceramics Via Granarolo 64 FAENZA, 48018 ITALY				8. PERFORMING ORGANIZATION REPORT NUMBER RT-2015/13		
9. SPONSORING/MONITORING AGENCY NAME(S) AND ADDRESS(ES) EOARD Unit 4515 APO AE 09421-4515				10. SPONSOR/MONITOR'S ACRONYM(S) AFRL/AFOSR/IOE (EOARD)		
				11. SPONSOR/MONITOR'S REPORT NUMBER(S) AFRL-AFOSR-UK-TR-2015-0012		
12. DISTRIBUTION/AVAILABILITY STATEMENT Distribution A: Approved for public release; distribution is unlimited.						
13. SUPPLEMENTARY NOTES						
14. ABSTRACT <p>The work herein described is the <i>final report</i> of the third year of activity in the frame of the contract No. FA8655-12-1-3004 between the US Air Force Research Laboratory and the Institute of Science and Technology of Ceramics, National Research Council of Italy (ISTEC-CNR). Materials production and first microstructural characterization have been carried out at ISTEC-CNR in Faenza (Italy), transmission electron microscopy analyses have been performed at the Institute of Microelectronic and Microsystems, National Research Council of Italy (IMM-CNR) in Bologna, mechanical characterization has been performed at ISTEC-CNR in Faenza (Italy). This report deals with the production and characterization of relevant ZrB₂ composites, with high refractory properties or containing short and long SiC fibers, TaC-based composites containing various types of reinforcement and at last oxides of Al and Zr containing short Hi-Nicalon fibers. Transmission electron microscopy has been used as fundamental technique to disclose the reinforcement features and their modification upon sintering of the composite. In addition some mechanical properties, like fracture toughness, strength from room temperature to 1500°C and nanoindentation, have been measured and correlated to the microstructural characteristics.</p>						
15. SUBJECT TERMS EOARD, Materials, microstructural characterization, high temperature						
16. SECURITY CLASSIFICATION OF: a. REPORT UNCLAS			17. LIMITATION OF ABSTRACT SAR	18. NUMBER OF PAGES 93	19a. NAME OF RESPONSIBLE PERSON Matthew Snyder	
					19b. TELEPHONE NUMBER (Include area code) +44 (0)1895 616420	

TECHNICAL REPORT

Protocol	 ISTECA - CNR - ISTECA Tit. VII 4 - CL. ATTIVITA' PEF N. 0000573 06/03/2015		
Title	Characterization of Ultra-high Temperature Ceramics via Transmission Electron Microscopy Relevant ZrB₂-based composites, TaC-based composites and oxides containing SiC chopped fibers		
Customer:	EOARD European Office of Aerospace Research and Development 4515 Box 14, APO AE 09421 USA		
Reference:	Award No.: FA8655-12-3004		
Compiled by:	Authors	Laura Silvestroni Diletta Sciti	 
Approved by:	Principal investigator	Diletta Sciti	
Verified by:	Quality manager	V. Biasini	

Institute of Science and Technology for Ceramics

Via Granarolo 64, I- 48018 FAENZA (Ra)

Tel. +39 0546 699711, Fax +39 0546 699719

<https://www.istec.cnr.it>

DATE	03/06/15
------	----------

Characterization of Ultra-high Temperature Ceramics via Transmission Electron Microscopy

Relevant ZrB₂-based composites, TaC-based composites and oxides containing SiC chopped fibers

Principal Investigator: Diletta Sciti

Co-Principal Investigator: Laura Silvestroni

Period of Performance: December 8th 2013 - March 7th 2015 (15 months)

ISTEC-CNR, Institute for Science and Technology for Ceramics,
Via Granarolo 64
I-48018 Faenza, Italy

March 6th 2015

DATE	03/06/15	
------	----------	--

	 <p>National Research Council of Italy istec Institute of Science and Technology for Ceramics</p>	
RT - 2015/13	TECHNICAL REPORT: FA8655-12-1-3004	Pag. 3/91

Foreword

The work herein described is the *final report* of the third year of activity in the frame of the contract No. FA8655-12-1-3004 between the US Air Force Research Laboratory and the Institute of Science and Technology of Ceramics, National Research Council of Italy (ISTEC-CNR).

Materials production and first microstructural characterization have been carried out at ISTEC-CNR in Faenza (Italy), transmission electron microscopy analyses have been performed at the Institute of Microelectronic and Microsystems, National Research Council of Italy (IMM-CNR) in Bologna, mechanical characterization has been performed at ISTEC-CNR in Faenza (Italy).

The contract was initiated on December 2011 with Dr. Ali Sayir as contract monitor, Dr. Diletta Sciti as Principal Investigator and Dr. Laura Silvestroni as Co- Principal Investigator.

This report deals with the production and characterization of relevant ZrB_2 composites, with high refractory properties or containing short and long SiC fibers, TaC -based composites containing various types of reinforcement and at last oxides of Al and Zr containing short Hi-Nicalon fibers.

Transmission electron microscopy has been used as fundamental technique to disclose the reinforcement features and their modification upon sintering of the composite. In addition some mechanical properties, like fracture toughness, strength from room temperature to $1500^\circ C$ and nanoindentation, have been measured and correlated to the microstructural characteristics.

The work herein presented has been performed by:

- Daniele Dalle Fabbriche (ISTEC - CNR) – hot pressing cycles;
- Laura Silvestroni (ISTEC - CNR) – ceramic processing, SEM and TEM analyses;
- Stefano Guicciardi (ISMAR – CNR) and Cesare Melandri (ISTEC – CNR) – mechanical characterization.

The authors wish to express their sincere gratitude to those who kindly enabled the realization of the composites:

- Alejandro Castro Linares (Mitsui & Co. Italia S.p.A.) for supplying Hi-Nicalon S fiber;
- UHTCs group in MS&T (Rolla), for the production of long fiber- ZrB_2 -composite.

This report was released by the authors in March 2015.

DATE	03/06/15
------	----------

Contents

SUMMARY OF THE RESEARCH EFFORT	6
LIST OF PUBLICATIONS AND CONTRIBUTES TO CONGRESSES	12
LIST OF TABLES	16
ABSTRACT	17
1. INTRODUCTION	18
2. METHODS, ASSUMPTIONS AND PROCEDURES	18
2.1. MATERIALS.....	18
2.2. MICROSTRUCTURAL CHARACTERIZATION	20
2.3. MECHANICAL CHARACTERIZATION	21
3. RESULTS AND DISCUSSION	22
ZRB₂-BASED CERAMICS	22
3.1. ZRB₂ + WSi₂	22
3.1.1. <i>Densification behavior</i>	23
3.1.2. <i>Microstructural features of ZBW</i>	23
3.1.3. <i>Microstructure evolution during densification</i>	29
3.1.4. <i>Mechanical properties</i>	31
3.1.5. <i>Conclusions on ZBW</i>	33
3.2. ZRB₂ + SiC FIBER	33
3.2.1. <i>ZrB₂ + short Hi-Nicalon S</i>	34
3.2.2. <i>ZrB₂ + long (BN)Hi-Nicalon</i>	40
3.2.3. <i>Mechanical properties</i>	46
3.2.4. <i>Crossed comparisons among fiber-containing ZrB₂-composites</i>	46
<i>Sintering additive: Si₃N₄ vs ZrSi₂</i>	46
<i>Fiber crystallinity: Hi-Nicalon vs Hi-Nicalon S</i>	48
<i>Fiber coating: naked vs BN</i>	48
<i>Fiber length: short vs long</i>	49
3.2.5. <i>Conclusions on ZrB₂ + fibers</i>	49
TAC-BASED CERAMICS	50
3.3. TAC BASELINES.....	51
3.4. REINFORCED TAC-COMPOSITES	52
3.4.1. <i>TaC + SiC particle</i>	52
3.4.2. <i>TaC + TaSi₂</i>	53
3.4.3. <i>TaC + SiC platelet</i>	53
3.4.4. <i>TaC + Hi-Nicalon fiber</i>	57
3.4.5. <i>TaC + Tyranno SA3 fiber</i>	60
3.4.6. <i>TaC + C fiber</i>	64
3.5. MORPHOLOGY EVOLUTION OF FIBERS AND PLATELETS	68
3.6. MECHANICAL PROPERTIES	71
3.7. EFFECT OF REINFORCING PHASE ON FRACTURE TOUGHNESS AND STRENGTH TRADEOFF	72
3.8. CONCLUSIONS ON TAC BASED CERAMICS	77
OXIDE-BASED CERAMICS	77
3.9. REINFORCED OXIDES.....	77

3.9.1.	<i>Al₂O₃ + Hi-Nicalon</i>	78
3.9.2.	<i>ZrO₂ + Hi-Nicalon</i>	81
3.9.3.	<i>Nanoindentation</i>	85
3.10.	CONCLUSIONS ON OXIDES	87
4.	CONCLUSIVE REMARKS	87
REFERENCES		89
LIST OF SYMBOLS, ABBREVIATIONS AND ACRONYMS		91
DISCLAIMER		91

Summary of the research effort

The contract contract No. FA8655-12-1-3004 between the US Air Force Research Laboratory and the Institute of Science and Technology of Ceramics, National Research Council of Italy (ISTEC-CNR) started in December 2011 with duration of 39 months.

The main purpose of the contract was the microstructural investigation through high resolution transmission electron microscopy of various ultra-high temperature ceramics (UHTCs) containing reinforcing phases.

One of the most urgent problems to solve for UHTCs is the improvement of fracture toughness. So far, research has successfully fabricated high density composites possessing good strength (500-1000 MPa). However, the low fracture toughness remains one of the major concerns for the application of these materials under severe environment. Toughness of ceramics can be improved by incorporation of suitable reinforcing phases provided that the chemistry of the system, i.e. the interaction between the matrix and the reinforcement during the thermal treatment, is properly controlled. The study of the intergranular phases developed at the matrix/reinforcement interface is then of paramount importance, because intergranular phase features affect the way the crack propagates through the matrix and hence the fracture toughness.

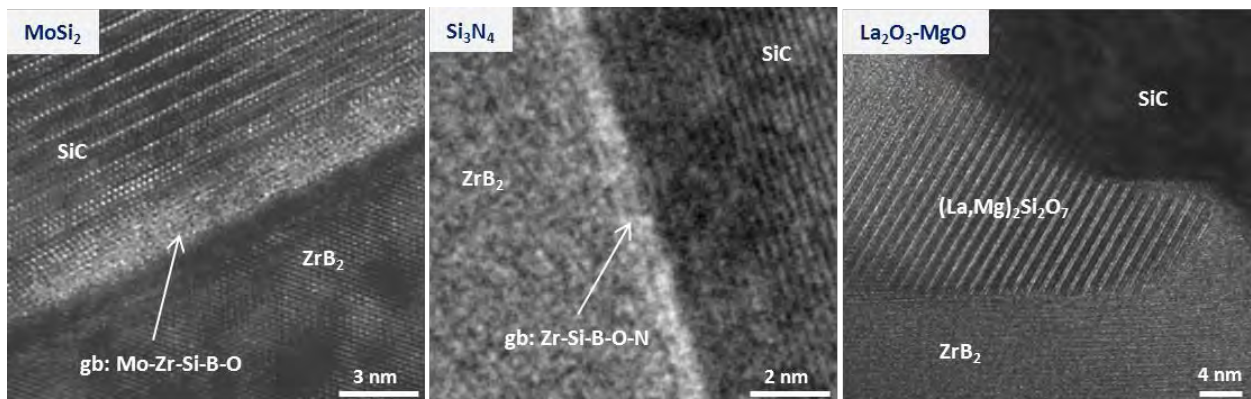
The activity included the production of ceramics and microstructural and mechanical characterization. Transmission electron microscopy was employed as fundamental technique to disclose the sintering mechanisms, microstructure evolution and toughening phenomena occurring in the materials. For selected materials mechanical properties, like fracture toughness, strength and nanoindentation, were measured and correlated to the microstructural features.

The investigations conducted so far greatly increased the knowledge and comprehension of the interactions between fibre and matrix and helped in the understanding of the most important toughening mechanisms. The main results achieved are summarized in the following.

1. In the first year, the research effort was focused on the production and microstructural analysis of ceramics based on ZrB₂ or HfB₂ containing SiC platelets or Hi-Nicalon SiC fibers.
- 1.1. The first approach exploited the irreversible $\beta \rightarrow \alpha$ transformation of SiC particles, occurring at temperature above 1900°C. Two were the routes covered: the first method consisted in sintering the composite at temperatures high enough to enable SiC transformation from rounded particle (β -polytype) to elongated platelet (α -polytype) in a conventional sintering furnace. Depending on the sintering additive, MoSi₂ or Si₃N₄, and the secondary phases formed upon sintering, different grain morphologies developed resulting in notably different mechanical properties. MoSi₂ enabled to increase the toughness from 3 to 5 MPa·Vm, thanks to the presence of a Mo-Zr-Si-B-O of amorphous phases at the grain junctions which favoured the intergranular fracture. The second route consisted in hot pressing the ceramic containing La₂O₃-MgO as sintering additives

and the subsequent annealing at higher temperature in a pressureless furnace in order to promote the SiC polytypic transformation and crystallize the glassy phases. In this case, several annealing cycles were explored to identify the most promising microstructure, displaying the right compromise between SiC platelets development and ZrB₂ unavoidable grains coarsening. For both approaches a model for the microstructure evolution was proposed.

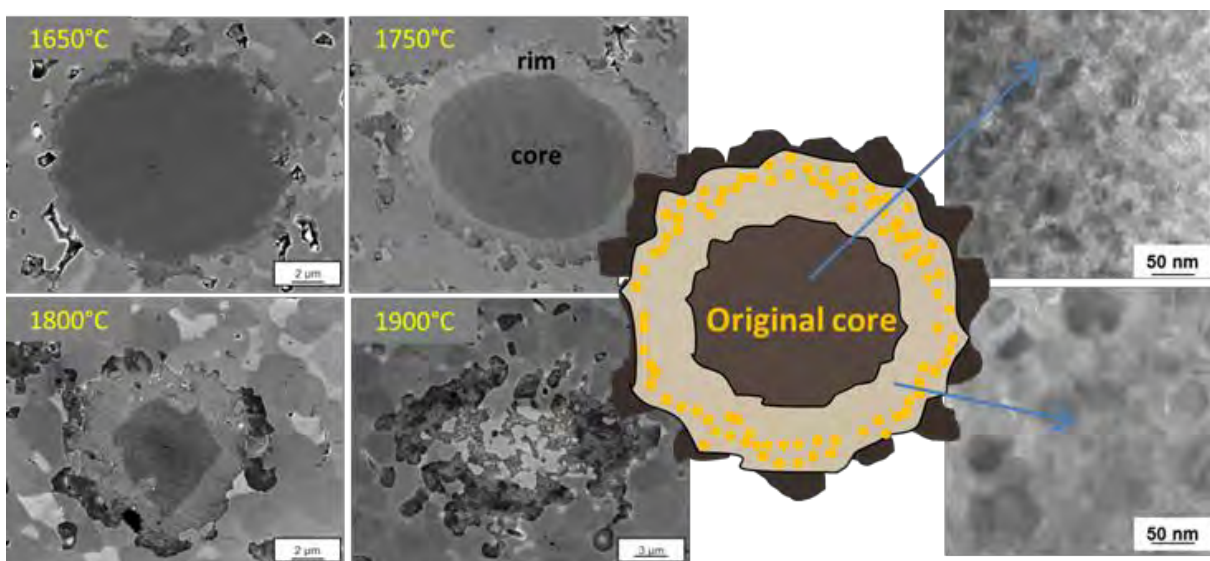
[Characterization of Ultra-high Temperature Ceramics via Transmission Electron Microscopy - In situ toughened ZrB₂ composites through SiC platelets, TR-2012/16, March 8th 2012; Publication n°1]



1.2. The second approach to increase the toughness of Zr- and Hf- borides was through introduction of chopped Hi-Nicalon fibers, i.e. SiC fiber belonging to the second generation. The purpose of the activity was a thorough comprehension of the chemistry of interaction between fiber, matrix and sintering additive, the effect of the sintering temperature on the fiber morphology evolution and its influence on the mechanical properties. To this aim, different sintering additives (Si₃N₄, MoSi₂ or ZrSi₂), sintering techniques (hot pressing and spark plasma sintering) and sintering temperatures (1550-1720°C), were explored. The extended investigations pointed out that Hi-Nicalon fibers are not inert in the boride matrix already from 1550°C and tend to react with the surrounding chemical environment, to collect impurities from the boride matrices or from the sintering additive and incorporate them. Independently of the sintering additive, the fiber evolves towards a multilayered configuration with an unreacted core comprising a Si-C-O amorphous phase, turbostratic graphite and ~30 nm SiC crystallites, a surrounding transformed shell with coarsened SiC crystallites and embedded particles deriving from the sintering aids or impurities from the matrix, and an outermost layer of SiC platelets. The sintering additive has an indirect role in the fiber transformation, since it dictates the sintering temperature. This is indeed the most important parameter influencing the fiber final structure and when sintering occurs above 1700°C, the fiber progressively loses its reinforcing action, becoming a secondary phase. Nanoindentation was employed to locally study the fibers' properties revealing the fiber SiC core softer and less stiff than the fiber rim, owing to the presence of residual amorphous Si-C-O phase and graphite. The

composites sintered with $ZrSi_2$ achieved the highest fracture toughness, 5.4-6.2 MPa·Vm, and the room temperature strength was around 400 MPa. No pullout was observed in any composite and the main toughening mechanism was presumed to be crack bowing. Strength around 400 MPa is maintained up to 1200°C, but at high temperature the unavoidable fiber degradation causes a strength collapse to 80-200 MPa.

[Characterization of Ultra-high Temperature Ceramics via Transmission Electron Microscopy - ZrB_2 and HfB_2 composites containing Hi-Nicalon SiC fibers, RT- 2012/88, December 4th 2012; Publications n°2,4]

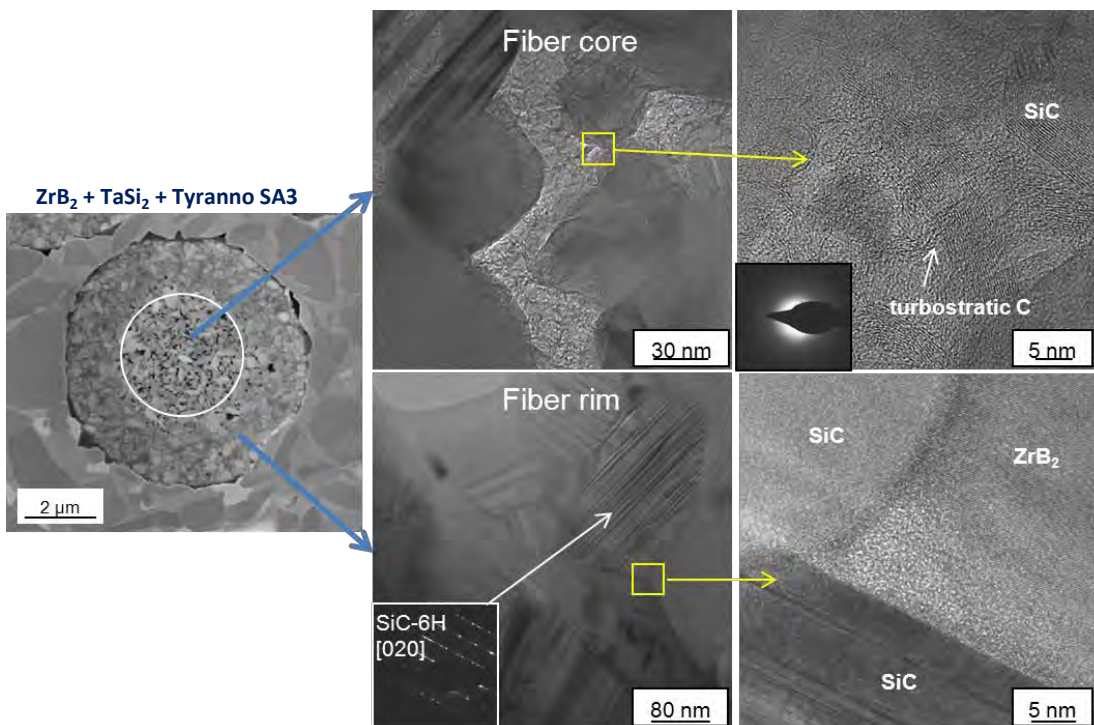


2. In the second year, the activities moved to the study of borides containing more refractory SiC fibers or C fibers.
- 2.1. Proved the high reactivity of Hi-Nicalon fibers towards the borides and the various sintering additives, we investigated Tyranno SA3 SiC fibers, possessing higher stability at elevated temperature and better performances in extreme environment.

ZrB_2 -based composites were produced with various sintering agents ($ZrSi_2$, Si_3N_4 , $TaSi_2$, $MoSi_2$) and sintered at different temperatures (1550-1800°C). As general feature, Tyranno SA3 fiber upon sintering showed a well-rounded shape with sharp interface with the matrix. TEM investigations revealed that the fiber is made of β -SiC crystallites surrounded by intergranular pockets, in turn composed by partially amorphous phase and turbostratic carbon. Moving from the core of the fiber outwards, a progressive removal of these intergranular pockets occurs accompanied with a coarsening of the SiC crystallites and crystallization of amorphous Si-C. The interfaces were clean only when $ZrSi_2$ was employed, but in the other cases wetted interfaces were generally observed. The sintering temperature limit for this kind of fiber is 1750°C, higher as compared to the Hi-Nicalon type. For these composites, the fracture toughness increased of 20-35% as compared to the unreinforced ceramics. The main toughening mechanism was identified as pinning, similar to other composites containing chopped Hi-Nicalon fibers, but secondary toughening mechanisms, like crack deflection and bridging were

envisioned from the study of low advancing crack and the fracture surface. The room temperature strength was around 420-460 MPa and the failure was dictated by the maximum fiber length. These values were maintained at 1200°C, thanks to the formation of thin silica layer healing small defects, but at 1500°C the strength dropped to 80-280 MPa, owing to the fiber degradation.

[Characterization of Ultra-high Temperature Ceramics via Transmission Electron Microscopy - ZrB₂ composites containing Tyranno SA3 SiC fibers: data collection, RT-2013/12, March 7th 2013; Publication n°6]



2.2. Subsequently, other ZrB₂ composites containing coated short fibers (C-coated Tyranno ZMI, B(Si)N-coated Hi-Nicalon S and carbon fibers), were sintered and investigated through scanning and transmission electron microscopy to study the fiber evolution and the fiber/matrix interface in presence of a protective film.

C-coated Tyranno ZMI fiber. This fiber displayed quite high tendency to react with the matrix during sintering and the fiber itself resulted notably altered with multilayered morphology, similar to Hi-Nicalon fiber. No evident trace of the pyrolytic carbon coating was found in the final microstructure, evidencing its high reactivity with the oxides covering the matrix powder. Despite the altered fiber structure, toughness values above 5 MPa·m^{0.5} were obtained, probably also due to the little fiber pull out observed on the fracture surface.

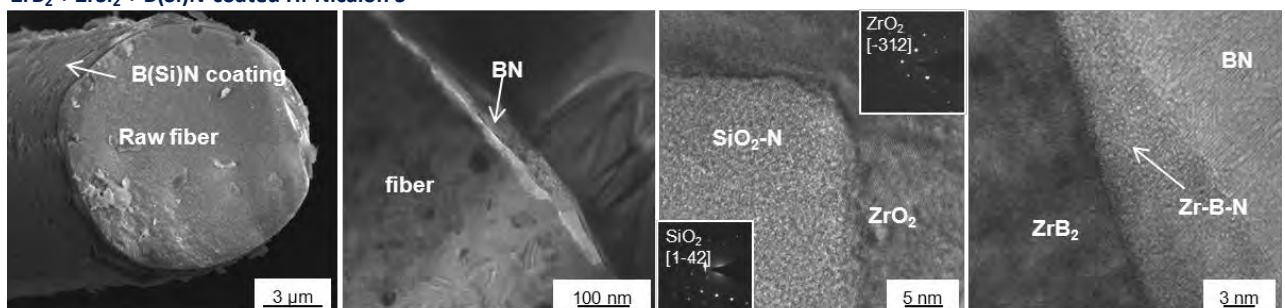
B(Si)N-coated Hi Nicalon fiber, type S. This kind of fiber showed very good stability as no multilayered morphology or interaction with the fiber was observed upon sintering. TEM analyses revealed no different chemistry, crystallinity or mean grain size of the SiC crystallites in the fiber core and edge. At the fiber/matrix

interface, additional phases coming from the sintering aids, such as $ZrSi_2$ and ZrO_2 , were found. The BN coating did not survive the processing, as most of it detached from the fiber, coarsened and developed in hexagonal BN with wetted amorphous phase in contact with ZrB_2 . In addition, adjacent to the fiber, crystobalite was found, probably deriving from the Si-doping of the BN coating exuded during sintering and crystallized during cooling. Modification of the process should be envisaged in order to maintain the Si-doped BN coating around the fiber and preventing its detachment and crystallization along the matrix. Another critical point is the formation of crystalline silica diffused along the matrix and around the fiber, which weakens the composite's properties and it is a possible cause of the low strength at high temperature, 40-90 MPa.

C fiber. Si_3N_4 used as sintering agent reacted with the carbon fiber and formed a homogeneous SiC layer around it. The interface between the newly formed SiC and the C fiber was weak, as testified by small cracks, and induced inner fiber pullout. TEM observation revealed that the fiber maintained its original structure, typical of PAN-derived fiber. ZrC particles were regularly embedded in the SiC layer and generally wet interfaces were found both at fiber/SiC interfaces and SiC/ ZrB_2 ones. The presence of little amount of SiC around the fiber also preserved a strength at 1500°C, around 270 MPa, from a steep drop due to the fiber oxidation.

[Characterization of Ultra-high Temperature Ceramics via Transmission Electron Microscopy - ZrB_2 composites containing different kinds of fibers, RT-2013/105, December 3rd 2013]

$ZrB_2 + ZrSi_2 + B(Si)N$ -coated Hi-Nicalon S

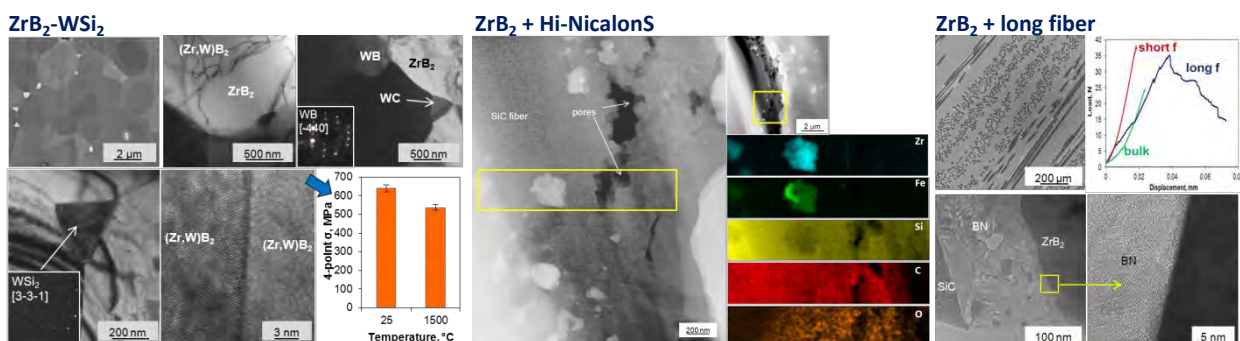


3. The third year was devoted to the study of two groups of UHTCs, ZrB_2 and TaC , and to the analysis of oxides, Al_2O_3 and ZrO_2 , containing SiC short fibers.

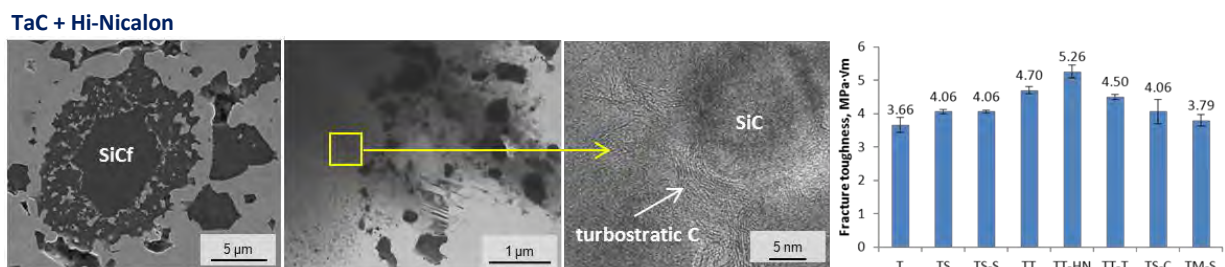
3.1 Among ZrB_2 , one first composite was produced through addition of WSi_2 to increase its high temperature performances. The microstructure was homogeneous and flaw-less with matrix grain displaying core-shell morphology, refractory Zr , W -silicides, -borides and -carbides segregated at the triple points and clean grain boundaries. This composite displayed strength retention of 84% at 1500°C in air.

Then another group of ZrB_2 -based ceramics was produced aiming at improving the fracture toughness of through the introduction of various kinds of SiC fibers (short, long, naked or BN-coated). Despite

remarkable differences among the fibers used, no major variations in toughness were measured, thus setting the limits of such kinds of composites.



3.2. As for TaC-based composites, several ceramics were designed in order to study the relationships between strength and toughness. The effect of different secondary phases was explored: (I) the addition of a transition metal silicide with suited thermo-elastic properties, $TaSi_2$, (II) the addition of SiC particles, platelets or fibers, and (III) chopped carbon fibers. TEM investigations revealed fundamental characteristics of fiber modifications or stress state in the matrix and the correlation of microstructural features, mechanical properties and existing models enabled to identify the residual tensional state in TaC matrix as the major obstacle to allow notable toughness improvements.



3.3. Then two oxide-based composites, namely Al_2O_3 and ZrO_2 containing 15 vol% of Hi-Nicalon SiC chopped fiber, were produced and characterized in order to study interface reactions between fiber and matrix and to understand the load transfer from the reinforce and a matrix possessing lower Young's modulus. These materials, which fall outside of the UHTC family, revealed interesting features concerning the effect of the fiber-matrix reactions, stability and bonds, not predictable from previous studies on non-oxide ceramics.

[Characterization of Ultra-high Temperature Ceramics via Transmission Electron Microscopy - Relevant ZrB_2 -based composites, TaC-based composites and oxides containing SiC chopped fibers, RT-2015/13, March 6th 2015; Publications n°3,5,7,9]

List of Publications and Contributions to Congresses

Journals

1. L. Silvestroni, D. Sciti, Microstructure evolution upon annealing of a ZrB_2 –SiC composite containing lanthana and magnesia, *J. Eur. Ceram. Soc.* 33 (2013) 403–412.
2. L. Silvestroni, S. Guicciardi, M. Nygren, C. Melandri, D. Sciti. “Effect of the sintering additive on the microstructure and thermo-mechanical properties of Hi-NicalonTM SiC fibers in a HfB_2 matrix”, *Journal of the American Ceramic Society*, 96 [2] 643-650 (2013).
3. L. Silvestroni, D. Sciti, L. Charpentier, M. Balat-Pichelin, “Zirconium carbide doped with Tantalum Silicide: microstructure, mechanical properties and high temperature oxidation”, *Materials Chemistry and Physics*, 143 [1] 407-415 (2013).
4. D. Sciti, S. Guicciardi, L. Silvestroni, “Are short Hi-Nicalon SiC fibers a secondary or a toughening phase for UHTCs?”, *Materials and Design*, 55, 821-829 (2014).
5. L. Silvestroni, D. Sciti, “TEM analysis, mechanical characterization and oxidation resistance of a highly refractory ZrB_2 -composite”, *Journal of Alloys and Compounds*, 602, 346-355 (2014).
6. L. Silvestroni, D. dalle Fabbriche, D. Sciti, “Tyranno SA3 fiber - ZrB_2 composites Part I: Microstructure and Densification”, *Materials & Design*, 65, 1253-1263 (2015).
7. L. Silvestroni, L. Pienti, S. Guicciardi, D. Sciti, “Strength and toughness: the challenging case of TaC-based composites”, *Composites B*, 72, 10-20 (2015).
8. L. Silvestroni, E. Landi, K. Bejtka, A. Chiodoni, D. Sciti, “Oxidation and kinetics of ZrB_2 containing chopped SiC fibers”, submitted to *Corrosion Science*.
9. L. Silvestroni, J. Watts, G. E. Hilmas, W. G. Fahrenholtz, D. Sciti, “Effect of a weak interface in ZrB_2 composite reinforced with long SiC fibers”, to be submitted to *Composites B*.

Chapter in books

1. L. Silvestroni, D. Sciti, Chapter 11: “Ultra-high temperature ceramics reinforced with SiC short fiber or whisker” in “Fiber-Reinforced Composites”, Ed. by F. Columbus, Nova Science Publishers, Inc., Hauppauge, NY, (2011).
2. L. Silvestroni, D. Sciti, Chapter 5: “Effect of transition metal silicides on microstructure and mechanical properties of ultra-high temperature ceramics” in “MAX Phases and Ultra-High Temperature Ceramics for Extreme Environments”, Ed. by J. Low, Y. Sakka and C. Hu, IGI Global. Hershey, PA, pp. 125-179 (2013).
3. D. Sciti, L. Silvestroni, V. Medri, F. Monteverde, Chapter 6: “Sintering and densification of ultra-high temperature ceramics” in “Ultra-High Temperature Ceramics: Materials for Extreme Environment

Applications", Ed. by W. G. Fahrenholtz, E. J. Wuchina, W. E. Lee and Y. Zhou, Wiley, Inc., ISBN 0-471-9781118700785 (2014).

Oral presentations

1. D. Sciti, "Sintering and densification of UHTCs". Presented at *Ultra-High Temperature Ceramics:Materials for Extreme Environment Applications II (ECI)*, Hernstein-A, May 13-18, 2012 – Invited.
2. L. Silvestroni, D. Sciti, S. Guicciardi, "ZrB₂ and HfB₂ toughened with Hi-Nicalon SiC chopped fibers". Presented at the *Workshop on the Design of Ceramic–Fiber Based Composites for Service Above 1400°C*, Boulder- CO, June 10-16, 2012 – Invited.
3. D. Sciti, L. Silvestroni, S. Guicciardi, A. Bellosi, "Potential and limits of SiC chopped fiber-reinforced Ultra High Temperature Ceramics". Presented at the *4th International Congress of Ceramics (ICC4), Chicago –IL, July 15-19, 2012 - Invited*.
4. D. Sciti, L. Silvestroni, L. Pienti, D. Dalle Fabbriche, C. Melandri, C. Capiani, "Ultra-high temperature borides reinforced with SiC short fibers". Presented at *4th Sino-Italian Conference on Space Aerothermodynamics and Hot Structures*, November 28-30 2012, Capua (NA) – I.
5. L. Silvestroni, D. Sciti, "Study of SiC fiber-matrix interaction in ultra-high temperature ceramics by transmission electron microscopy". 37 th International Conference and Exposition on Advanced Ceramics and Composites (ICACC), Daytona Beach- FL, January 27-February 1, 2013.
6. D. Sciti, S. Guicciardi, L. Silvestroni, "Ultrahigh temperature Ceramics for Thermal Protection systems, Propulsion and Energy: From densification to thermo mechanical properties", 12th International Conference on Ceramic Processing Science, Portland-OR, August 4-7, 2013 – Invited.
7. D. Sciti, L. Silvestroni, L. Zoli, V. Medri, "Processing, sintering and characterization of fiber-containing UHTCs". Presented at CIMTEC 2014, Montecatini Terme, Italy, June 8-13, 2014 – Invited.
8. L. Silvestroni, D. Sciti, "Characterization of UHTCs containing various kinds of fibers". Presented at CIMTEC 2014, Montecatini Terme, Italy, June 8-13, 2014 – Invited.
9. D. Sciti, L. Zoli, A. Natali Murri, V. Medri, C. Melandri, "Processing of continuous fiber ZrB₂ composites", A Workshop: Review of the NHSC Program and Future of High Temperature Structural Ceramics, Univ. of Boulder, Colorado, July 26-August 2, 2014.
10. D. Sciti, L. Silvestroni, L. Zoli, A. Bellosi, "UHTCMCs: short vs continuous fibers", to be presented to the ECI conference: Ultra-high Temperature Ceramics: Materials For Extreme Environment Applications III, Surfer's Paradise Gold Coast, Australia, April 12-17, 2015 – Plenary speaker.
11. D. Sciti, L. Silvestroni, V. Medri, L. Zoli, "UHTC-CMCs for thermal protection systems and propulsion". To be presented at 14th ECERS, Toledo, Spain, June 21-25, 2015.

List of Figures

Figure 1: Sketch of cut directions for testing the composites containing short or long fibers.....	21
Figure 2: a) Densification curve recorded during hot pressing. T_{ON} : temperature at which shrinkage begins, T_{LP} : temperature at which liquid phase forms. In the inset: plot of the maximum densification rate as a function of the temperature for different silicides; Z: $ZrSi_2$, T: $TaSi_2$, M: $MoSi_2$, W: WSi_2 . b) X-ray diffraction pattern of the sintered composite showing the crystalline phases and c) ZrB_2 peaks splitting at high 2-Theta angles... ..	24
Figure 3: SEM images of the sintered ceramic showing a) the overall microstructure, b) the matrix morphology with c) EDX spectra of core and shell. d) Elemental mapping of the matrix showing the distribution of W in the shell. e)-g) secondary W-based phases.....	25
Figure 4: a)-c) TEM images showing the core-shell structure of the matrix of the sintered ceramic with EDX spectra at low and high voltage and SAEDP taken from a) confirming epitaxy between ZrB_2 and $(Zr,W)B_2$. The inset in c) shows a W-rich precipitate occasionally found at the core-shell interface. ppt=precipitate.....	26
Figure 5: TEM images of the secondary phases with EDX spectra and diffraction patterns showing the presence of WB, WC, WSi_2 and residual ZrO_2	27
Figure 6: TEM and HRTEM images of the triple point junctions showing clean grain boundaries between a)-f) adjacent $(Zr,W)B_2$ grains and g)-i) between WB and $(Zr,W)B_2$	28
Figure 7: HR-TEM images showing clean grain boundaries between $(Zr,W)B_2$, $(Zr,W)C$, $(W,Zr)Si_2$ and WB.....	29
Figure 8: a) Load-displacement curves for flexural strength at room temperature and at 1500°C in air. b) SEM images of the cross section of a bar after flexural strength testing at 1500°C showing the presence of acicular BO-based crystals.....	32
Figure 9: a) Low and b) high magnification of Hi-Nicalon S fiber after in house chopping and mixing with ZrB_2 powder.....	33
Figure 10: a) Fracture surface and b)-d) polished surfaces of ZrB_2 composite containing Hi-Nicalon S fiber and Si_3N_4 as sintering additive. b) Overview of a fiber section, c) magnification of fiber-matrix interface and d) reaction products trapped inside the fiber	35
Figure 11: TEM images showing a)-c) secondary phases in the matrix and d)-i) examples of BN/ ZrB_2 wetted interfaces with e) diffraction patterns and f) EDS spectra of the amorphous phase and BN.....	36
Figure 12: a)-d) TEM images showing particles trapped in the fiber identified as $ZrSi_2$, Si. e)-f) Si_3N_4 residuals are also found at the fiber-matrix interface.....	36
Figure 13: STEM image of a fiber edge in ZBS-HS with EDS elemental mapping.....	37
Figure 14: a)-d) Microstructure of a SiC fiber in ZBS-HS moving from the core outwards with corresponding diffraction patterns showing improved crystallinity. e)-h) magnification of fiber core showing triple point junctions and partially amorphous C-rich phase.....	38
Figure 15: Examples of matrix/fiber interfaces in ZBS-HS showing wetted grain boundaries.....	39
Figure 16: a) Fracture surface and b)-f) polished surfaces of ZrB_2 composite containing Hi-Nicalon S fiber and $ZrSi_2$ as sintering additive. b) Overview of the material microstructure, c) magnification of a fiber section, d) formation of SiC between two fibers, e) fiber-matrix interface and f) reaction products at the fiber edge... ..	40
Figure 17: Sketch of the experimental procedure for the fabrication of 0/90° long-fiber ZrB_2 composite.....	41
Figure 18: a) Fracture surface and b)-f) polished surfaces of ZrB_2 composite containing long BN-coated Hi-Nicalon fiber and $ZrSi_2$ as sintering additive. b) Overview of the material architecture, c) magnification of the matrix showing ZrO_2 and SiC aggregates, d) fiber distribution with trapped porosity, e) homogeneous BN coating around the fibers and f) efficient blockage of secondary phases at the coating interface.	41
Figure 19: Examples of HR-TEM images of the matrix in ZBZ-iH* showing the interfaces between ZrB_2 - SiO_2 - ZrO_2 with EDS spectra of SiO_2 and ZrO_2 containing N traces.....	42
Figure 20: TEM images of fiber matrix interfaces in ZBZ-iH* at a) low and b) high magnification. c) Morphology of the coating with d) HR-image of BN with diffraction pattern and e) EDS spectra of the particles trapped within the coating	43

Figure 21: HR-TEM images of fiber-coating-matrix interfaces in ZBZ-iH*. a)-c) coating-ZrB ₂ interfaces and d)-f) coating-fiber interfaces.....	44
Figure 22: STEM image of a fiber edge in ZBZ-iH* with EDS elemental mapping.....	45
Figure 23: Morphology of a SiC fiber in ZBZ-iH* a) in the core and b) in the edge with corresponding diffraction patterns showing similar crystallinity degree and mean grain size. c)-d) HR-TEM of crystallites and partially amorphous C-rich phase.....	45
Figure 24: Examples of fiber section in various ZrB ₂ -based composites sintered with ZrSi ₂ or Si ₃ N ₄ as additive and containing Hi-Nicalon or Hi-Nicalon S, naked or BN-coated, long or short fiber, like indicated in the sketch on the left. For each composite, the sintering temperature and the fracture toughness are reported.	47
Figure 25: a) Load-displacement curves recording during CNB tests of unreinforced, chopped- or long-fiber reinforced ZrB ₂ composites and b) fiber pullout in ZBZ-iH* after flexural test.	49
Figure 26: SEM image of reinforcing phases: a) SiC particles, b) Hi-Nicalon, c) Tyranno SA3, d) C fiber.....	51
Figure 27: SEM images of a) pure TaC (T), b) TaC+Si ₃ N ₄ (TS), c) TaC+Si ₃ N ₄ +SiC particles (TS-S), d) TaC+ TaSi ₂ (TT).	52
Figure 28: SEM images of polished section of TM-S showing a) platelets distribution, b) platelets pullout occurred during polishing and c) magnification of a platelet with Co and Si phases at the triple junctions.	53
Figure 29: TEM images of TM-S showing adjacent SiC platelets and secondary phases at the triple junctions.	54
Figure 30: Examples of a),b) SiC platelets with corresponding EDS spectra in c) showing the core-rim morphology and chemistry.	54
Figure 31: a) TEM and b) HR-TEM images of adjacent SiC platelets with EDS spectra and diffraction pattern in the insets.....	55
Figure 32: Examples of SiC-TaC interfaces in TM-S showing clean boundaries with diffraction patterns inset.	56
Figure 33: SEM images of polished section of TT-H showing a) the overall microstructure, b) fiber deterioration and TaSi ₂ aspect, c) a fiber section and d) the magnification fiber/matrix interface.	57
Figure 34: a) SEM image of a fiber section in TT-HN and b)-d) TEM images of a fiber at the interface with the matrix showing SiC coarsening and trapped dark TaC particles between core and rim.....	58
Figure 35: TEM images of fiber core with diffraction pattern showing the presence of amorphous phase and turbostratic carbon.	59
Figure 36: a) TEM image TaC particles at the core/rim interface with b) EDS and diffraction pattern, c) SiC platelets around the fiber with d) EDS spectra showing Ta traces.....	60
Figure 37: SEM images of polished section of TT-T showing a) the fiber distribution, b) the overall microstructure, c) formation of SiC , d) TaSi ₂ cracking, e) a fiber section and f) metal impurities trapped in fiber debris.	61
Figure 38: TEM images of b) fiber core and c) fiber rim with diffraction pattern showing similar crystallinity degree....	61
Figure 39: a)-c) TEM images of the fiber core showing partially amorphous Si-C, and turbostratic carbon and d)-f) fiber rim showing clean grain boundaries.....	62
Figure 40: HR-TEM images of a)-c) TaC/SiC interfaces or d)-f) fiber/Ta ₅ Si ₃ /TaSi ₂ interfaces.....	63
Figure 41: SEM images of polished section of TS-C showing a) the fiber distribution, b) the overall microstructure, c) scattered SiC in the matrix , d) a fiber section, e) a magnification of the fiber/matrix interface with arrows indicating graphite flakes and f) graphite sheets throughout TaC grains.	64
Figure 42: a), b) TEM images of fiber debris with HR-TEM of c) C fiber with diffraction pattern showing graphite reflections and d) TaC matrix showing lattice strain.	65
Figure 43: HR-TEM images of Cf/TaC interfaces showing a)-c) clean grain boundaries or d)-e) wetted interfaces with EDS spectrum of the amorphous Ta-Si-C-O phase.....	66
Figure 44: Examples of HR-TEM images of SiC/TaC interfaces showing clean grain boundaries.	67
Figure 45: SEM images of fracture surfaces of TaC-based materials a) TM-S, b) TT-HN, c) TT-T, d) TS-C.	68
Figure 46: Sketch of the morphology evolution of platelets and fibers in the TaC-matrix during sintering. a) SiC particles, b) Hi-Nicalon fiber, c) Tyranno SA3 fiber and d) C fiber.	70
Figure 47: Plots of a) CNB fracture toughness and b) 4-point flexural strength for TaC-based composites.	71
Figure 48: Calculated thermal residual stresses in the TaC-based composites. ⁵² Δt=1400°C.	73
Figure 49: SEM images of slow advancing cracks in: a) TS-S, b) TM-S, c) TT-HN, d) TT-T, e) TS-C. Arrows indicate crack deflection by fibers or platelets.	74

Figure 50: Plot of fracture toughness and strength of TaC-based composites.	76
Figure 51: SEM images of the AO-H sample showing a)-c) fracture surfaces and d)-f) polished surfaces.	78
Figure 52: TEM images of the AO-H sample showing clean grain boundaries in the Al_2O_3 matrix.	79
Figure 53: TEM images of the AO-H sample showing clean grain boundaries in the Al_2O_3 matrix.	80
Figure 54: TEM images of the AO-H sample showing example of fiber/matrix interface with EDS spectra in c)....	80
Figure 55: a) HR-TEM image of a SiC fiber in the AO-H sample with EDS spectrum and diffraction pattern in b).....	81
Figure 56: SEM images of the ZO-H sample showing a)-c) fracture surfaces and d)-g) polished surfaces with EDS of the interface in h).....	81
Figure 57: HR-TEM images of the ZO-H sample showing a)-b) clean grain boundaries and c) a triple point junction free of other phases, as confirmed by the EDS spectra in d).	82
Figure 58: TEM images of the fiber in ZO-H sample showing the fiber morphology with β -SiC crystallites, turbostratic C and partially amorphous Si-C-O phase	83
Figure 59: TEM images of the fiber/Matrix interface in ZO-H sample with HR-images and EDS spectra as indicated.	84
Figure 60: HR-TEM images of the fiber/matrix interface in ZO-H sample showing the presence of turbostratic carbon indicated by arrows.	85
Figure 61: Nanoindentation results of the oxide reinforced composites. a), b) Young's modulus (E), d), e) nanohardness (H) with peak load equal to 200 and 5 mN. c) Example of a 200 mN indentation on a fiber in ZO-H and f) of an indentation grid in AO-H.	86

List of Tables

Table 1: Label and compositions of the composites produced and analyzed.	19
Table 2: Composition, mean grain size and mechanical properties of $\text{ZrB}_2\text{-WSi}_2$ ceramic compared to other ZrB_2 -composites containing either transition metal silicides or W-compounds. m.g.s.: mean grain size, K_{IC} : fracture toughness measured by chevron notch technique, HV: microhardness (1 kg), σ : 4-point flexural strength at room temperature or at 1500°C in air, PS: pressureless sintering.	31
Table 3: Composition, sintering parameters, relative density and mechanical properties of SiC fiber-reinforced ZrB_2 ceramics.	34
Table 4: Overview of thermo-mechanical properties of Hi-Nicalon and Hi-Nicalon S fibers. ³⁴	48
Table 5: Label, composition, sintering parameters, density, mean grain size (m.g.s.) and size of the reinforcing phases before and after sintering. HP: hot pressing, PS: pressureless sintering, AR: aspect ratio.	51
Table 6: Composition, sintering conditions, main microstructural features and mechanical properties of Al_2O_3 - and ZrO_2 -based composites. ρ : density, m.g.s.: mean grain size, E: indentation modulus, H: hardness.	78

Abstract

The materials described in the present report are based on ultra-high temperature ceramics, ZrB_2 and TaC , and on oxides, Al_2O_3 and ZrO_2 .

Among ZrB_2 , one first composite was produced with the purpose of obtaining a refractory ceramic with high strength up to high temperature, whilst another group of ceramics were produced aiming at improving the fracture toughness, through the introduction of various kinds of SiC fibers (short, long, naked or BN-coated).

As for TaC -based composites, several ceramics were designed in order to study the relationships between strength and toughness. The effect of different secondary phases was explored: (I) the addition of a transition metal silicide with suited thermo-elastic properties, $TaSi_2$, (II) the addition of SiC particles, platelets or fibers, and (III) chopped carbon fibers.

Then two oxide-based composites, namely Al_2O_3 and ZrO_2 containing 15 vol% of Hi-Nicalon SiC chopped fiber, were produced and characterized in order to study interface reactions between fiber and matrix and to understand the load transfer from the reinforce and a matrix possessing lower Young's modulus.

All the materials produced were examined through scanning electron microscope (SEM), to study the distribution of the secondary phases, and high resolution transmission electron microscope (HR-TEM), to analyse the microstructure at nanoscale level, with particular attention to the evolution of the fiber morphology and to the study of the interfaces with the matrix.

This study allowed understanding of the fiber chemical stability towards different sintering additives and matrices at different temperatures. TEM analyses revealed to be essential to investigate the nanostructured arrangement of fiber and crystalline organization of the matrices.

The mechanisms leading to the final microstructure have been proposed and the mechanical properties have been correlated to the microstructural features.

1. Introduction

In this final report three classes of materials are investigated: ZrB₂-based composites with particular refractoriness or damage tolerant properties, TaC-based composites containing secondary phases aiming at improving the fracture toughness, and oxide-based ceramics containing SiC short fibers.

A ZrB₂-based material was produced through addition of WSi₂ to increase its high temperature performances. Conventional ball milling and hot pressing procedure led to a composite with homogeneous and flaw-less microstructure with refractory Zr,W-silicides, -borides and -carbides segregated at the triple points and clean grain boundaries. This composite displayed strength retention of 84% at 1500°C in air.

Following previous results on borides toughened through introduction of short SiC or C fibers,¹ another group of ZrB₂-based composites was processed with introduction of different kinds of SiC fiber (partially amorphous/crystalline, short/long, naked/coated) in order to study the stability of the fiber and its effect on fracture and strength of the composite. Despite remarkable differences among the fiber used, no major variations in toughness were measured, thus setting the limits of such kinds of composites.

TaC-based ceramics were manufactured with addition of specific secondary phases again aiming at achieving fracture toughness above 5 MPa·√m. The nature of the reinforcing phases spanned from ductile particles, SiC particles, platelets or fibers and to C fibers. TEM investigations revealed fundamental characteristics of fiber modifications or stress state in the matrix and the correlation of microstructural features, mechanical properties and existing models enabled to identify the residual tensional state in TaC matrix as the major obstacle to allow notable toughness improvements.

As for Oxides, Al₂O₃ and ZrO₂ were chosen as baseline materials in order to investigate the interface reactions with Hi-Nicalon chopped fiber and to study eventual different behavior when coupling such fibers with lower modulus matrices. These materials, which fall outside of the UHTC family, revealed interesting features concerning the effect of the fiber-matrix reactions, stability and bonds, not predictable from previous studies on non-oxide ceramics.

2. Methods, Assumptions and Procedures

2.1. Materials

The following commercial powders were used to produce the composites, whose compositions and sintering parameters are reported in Table 1.

Matrices:

- hexagonal ZrB₂ (H.C. Starck, Grade B, Munich, Germany), specific surface area 1.0 m²/g, particle size range 0.1-8 µm, impurities (wt%): 0.25 C, 2 O, 0.25 N, 0.1 Fe, 0.2 Hf;
- cubic TaC (Treibacher Industrie AG, Althofen, Austria), mean particle size 1.1 µm;

- α -Al₂O₃ (Baikalox CR30, Baikowski, Cedex, France), 99.99% α : γ =80:20, specific surface area 26 m²/g, particle size range 300 nm, impurities (ppm): 22 K, 16 Si, 13 Na, 3 Fe, 2 Ca.
- tetragonal ZrO₂ (TZ-3YS-E Tosoh Co., Yamaguchi-ken, Japan), specific surface area 6.8 m²/g, particle size range 38 nm, impurities (wt%): 5.15 Y₂O₃, 0.252 Al₂O₃, 0.02 SiO₂, 0.002 Fe₂O₃, 0.008 Na₂O;

Table 1: Label and compositions of the composites produced and analyzed.

Label	Matrix	Secondary phase, vol%	Sint. add., vol%	TEM
ZBW	ZrB ₂	15 WSi ₂	-	X
ZBS-HS		10 Hi-Nicalon S	5 Si ₃ N ₄	X
ZBZ-HS		10 Hi-Nicalon S	10 ZrSi ₂	-
ZBZ-iH*		25 BN-Hi Nicalon*	10 ZrSi ₂	X
T	TaC	-	-	-
TS		-	5 Si ₃ N ₄	-
TS-S		15 β -SiC	5 Si ₃ N ₄	-
TM-S		15 β -SiC	5 MoSi ₂	X
TT		15 TaSi ₂	-	X
TT-H		15 Hi-Nicalon	10 TaSi ₂	X
TT-T		15 Tyranno SA3	10 TaSi ₂	X
TS-C		15 Cfiber	5 Si ₃ N ₄	X
AO	Al ₂ O ₃	-	-	-
AO-H		20 Hi-Nicalon	-	X
ZO	ZrO ₂	-	-	-
ZO-H		20 Hi-Nicalon	-	X

*continuous fiber

Secondary phases:

- tetragonal WSi₂ (Sigma Aldrich, Milano, Italy), 99.5%, -325 mesh, traces of metals <6000 ppm.
- β -SiC (BF-12 Starck, Germany), specific surface area 11-13 m²/g, mean particle size 0.60 μ m, impurities (wt%): 0.88 O.
- Hi-Nicalon chopped fibers (COI Ceramics Inc., Magna, UT), diameter: 15 μ m, composition (wt%) Si:C:O= 63.7:35.8:0.5;
- Hi-Nicalon S (NGS Advanced Fibers Co., Ltd., Toyama, Japan), diameter: 13 μ m, chopped length: 100-200 μ m, 1.2 wt% PVA sizing, impurities (wt%): 0.5 O;
- Tyranno SA3 SiC fibers (UBE Europe GmbH, Dusseldorf, Germany), diameter: 7.5 μ m, chopped length: 100-200 μ m, composition (wt%) Si:C:O= 67:31:<0, Al<2;.
- C fiber (supplied by Aeronautical Service, Italy) diameter: 7 μ m, chopped length: 250 μ m.
- BN-coated Hi-Nicalon fibers (supplied by MST, Rolla, US), see pag. 40 for further details.

Sintering additives:

- hexagonal TaSi₂ 99.0%, (ABCR, GmbH & Co. Karlsruhe, Germany), 5-10 μ m FSSS, mean particle size 6.82 μ m, impurities (wt%): 0.05 C, 0.21 O, 0.03 Fe;

- tetragonal MoSi₂ (Aldrich, Germany), specific surface area 1.60 m²/g, mean particle size 1 µm, impurities (wt%): 1 O;
- orthorhombic ZrSi₂-F (Japan New Metals Co., LTD, Osaka, Japan) particle size 2-5 µm, impurities (wt%): 0.15 C, 0.30 Fe, 1.00 O;
- α-Si₃N₄ Baysinid (Bayer, Germany), specific surface area 12.2 m²/g, mean particle size 0.15 µm, impurities (wt%): 1.5 O;

In the case of Tyranno SA3, Hi-Nicalon S and C fiber, we started from a continuous spool, which was in house chopped. The chopped fibers were mixed to the powders through ball milling for 24 h in absolute ethanol using ZrO₂ milling media. Subsequently the slurries were dried in a rotary evaporator. After de-agglomeration of the powder mixtures, 30 mm-diameter pellets were shaped by uniaxial pressing with 20 MPa.

The pellets were then either hot pressed in low vacuum (~100 Pa) using an induction-heated graphite die with an uniaxial pressure of 30 MPa during the heating and increased up to 40-50 MPa at the maximum temperature, or pressureless sintered in a resistance-heated graphite furnace under a flowing argon atmosphere (~1 atm). For all the composites, the maximum sintering temperature was set on the basis of the shrinkage curve. Free cooling followed. The schedule of each sintering runs is reported in Table 1. The process for production of long-fiber reinforced ZrB₂ will be described separately in Section 3.2.2.

2.2. Microstructural Characterization

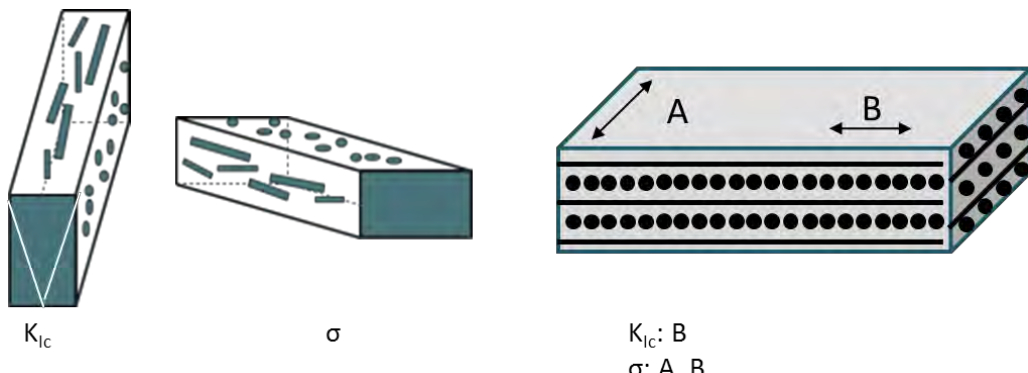
The bulk densities were measured by Archimedes' method and confirmed by SEM inspection.

The microstructure was analysed on fractured and polished surfaces by scanning electron microscopy (FE-SEM, Carl Zeiss Sigma NTS GmbH, Oberkochen, DE) and energy dispersive x-ray spectroscopy (EDS, INCA Energy 300, Oxford instruments, UK). In order to limit lateral spreading of the electron beam, EDS analysis was carried out at acceleration voltages of 6-10 KeV. TEM samples were prepared by cutting 3 mm discs from the bulk of the sintered pellets. These were mechanically ground down to about 20 µm and then further ion beam thinned until small perforations were observed by optical microscope. Local phase analysis was performed using transmission electron microscopy (TEM, FEI Tecnai F20 ST) equipped with a Schottky emitter and operating at a nominal voltage of 200 keV, combined with a EDAX EDS X-ray liquid nitrogen cooled spectrometer PV9761/II with a super ultra-thin window. Scanning Transmission Electron Microscopy (STEM) measurements have been performed on selected composites with the same TEM in nanoprobe mode providing a point resolution 0.19 nm. Quantitative calculations of the microstructural parameters, like residual porosity, mean grain size and secondary phase content, were carried out via image analysis with a commercial software package (Image-Pro Plus® version 7, Media Cybernetics, Silver Springs, MD, USA).

2.3. Mechanical Characterization

The fracture toughness (K_{Ic}) was evaluated using chevron notched beam (CNB) in flexure. The test bars, $25 \times 2 \times 2.5 \text{ mm}^3$ (length by width by thickness, respectively), were notched with a 0.1 mm-thick diamond saw; the chevron-notch tip depth and average side length were about 0.12 and 0.80 of the bar thickness, respectively. The direction of testing is sketched in Fig. 1. The specimens were fractured using a semi-articulated silicon carbide four-point fixture with a lower span of 20 mm and an upper span of 10 mm using a screw-driven load frame (Instron mod. 6025). The specimens, three for each composite, were loaded with a crosshead speed of 0.05 mm/min. The “slice model” equation of Munz et al.² was used to calculate K_{Ic} .

Figure 1: Sketch of cut directions for testing the composites containing short or long fibers.



On the same machine and with the same fixture, the flexural strength was measured at room temperature (σ_{RT}) and up to 1500°C in air or in partially protective argon atmosphere in order to reduce any oxidation effect; for each material five chamfered bars with dimensions $25 \times 2.5 \times 2 \text{ mm}^3$ (length by width by thickness, respectively) were tested.

On selected composites, the *in situ* properties of the fibers and matrices were evaluated by nanoindentation tests (Nanoindenter XPTM, MTS Systems Corporation, Oak Ridge, TN, USA) using a Berkovich diamond tip. Peak loads of 5 and 200 mN were used to investigate the indentation hardness and indentation modulus of the different phases. The load-unload cycles consisted in a continuous loading up to the peak value with a loading rate of $\Delta p/p=0.05$ followed by an immediate unloading with no holding time. For each position of interest, i.e. matrix and fiber, at least thirty indentations were made. Hardness and indentation modulus were calculated by the data acquisition software of the nanoindenter (TestWorksTM ver. 4.06A), which is based on the model of Oliver and Pharr.³ The software automatically corrected the raw load-displacement data for the machine compliance and thermal drift. Before the tests, the area function of the indenter tip was calibrated on a standard fused silica specimen. SEM was employed to correlate the data to the corresponding indented location. For the indentation modulus calculation, Poisson ratio values of 0.24⁴, 0.27⁵ and 0.13⁶ were used for Al_2O_3 , ZrO_2 and Hi-Nicalon fiber, respectively.

DATE	03/06/15
------	----------

3. Results and Discussion

ZrB₂-based ceramics

3.1. ZrB₂ + WSi₂

The impelling demand of reusable and long lasting materials, able to operate at high temperature and for long time pushes the scientific research towards continuous search of materials possessing a combination of properties always more challenging. The new concept of hypersonic vehicles actually lies on the availability of these new materials. Like most of parts of motors, the components of propulsion or hypersonic vehicles are exposed to significant heating flux where mechanical solicitations are present too. Therefore the main requirement that a material for such applications should satisfy is a combination of refractoriness at high temperature in oxidizing environment and sufficient mechanical resistance in such environment. The class of compounds commonly known as ultra-high temperature ceramics (UHTCs) has been identified as potential candidate for operating in harsh conditions owing to their melting point exceeding 3000°C and their resistance to ablation.⁷

It has been shown that ZrB₂-based composites can achieve strength up to 1 GPa⁸ upon a tailored design of composition and processing. A recent work reported that texturing of ZrB₂ by magnetic field during slip casting process enabled to achieve strength overcoming 800 MPa at 1600°C.⁹ It has been further demonstrated that the addition of dopants, in particular silicides and carbides of transition metals in groups V and VI, can induce a strength retention at high temperature by altering the microstructural features.^{10,11} For example, strength of 640 MPa at 1500°C in argon has been reported after introduction of WC.¹¹ In another paper, WC-doping was introduced in ZrB₂-SiC composite in amounts ranging from 3 to 7 vol% and again increased oxidation performances of the W-doped ceramics as compared to pure ZrB₂-SiC were reported.¹² The reasons for this improvement were ascribed to the formation of a eutectic between WO₃ and ZrO₂ at 1275°C, that acted as liquid phase sintering and decreased the porosity of the scale, or WO₃ acted as barrier itself due to the volume increase associated with oxidation of W to WO₃. In a dedicated study, the oxidation behavior of ZrB₂ with 0, 4, 6, or 8 mol% W was studied at 800–1600°C and pointed out that the addition of W into B₂O₃ increased the stability of the protective glassy layer, which resulted in higher oxidation resistance.¹³ Other authors suggested that tungsten oxide species form strong acid sites on ZrO₂ and inhibit ZrO₂ tetragonal to monoclinic structural transformations.¹⁴

In this study, a ZrB₂ ceramic was hot pressed through addition of WSi₂. WSi₂, with a tetragonal structure, has been the focus of considerable attention as an attractive material for electronics and high temperature application, as its properties provide the desirable combination of high melting temperature (2160°C), good strength at high temperature, good creep resistance and high oxidation resistance which relies on the formation of vitreous, dense, adherent SiO₂ scale.¹⁵ Following previous positive results obtained with other transition metal silicides¹⁶ and in view of

the above mentioned physic-chemical features, WSi_2 could be an adequate sintering additive for ZrB_2 for applications in ultra-high temperature environments.

3.1.1. Densification behavior

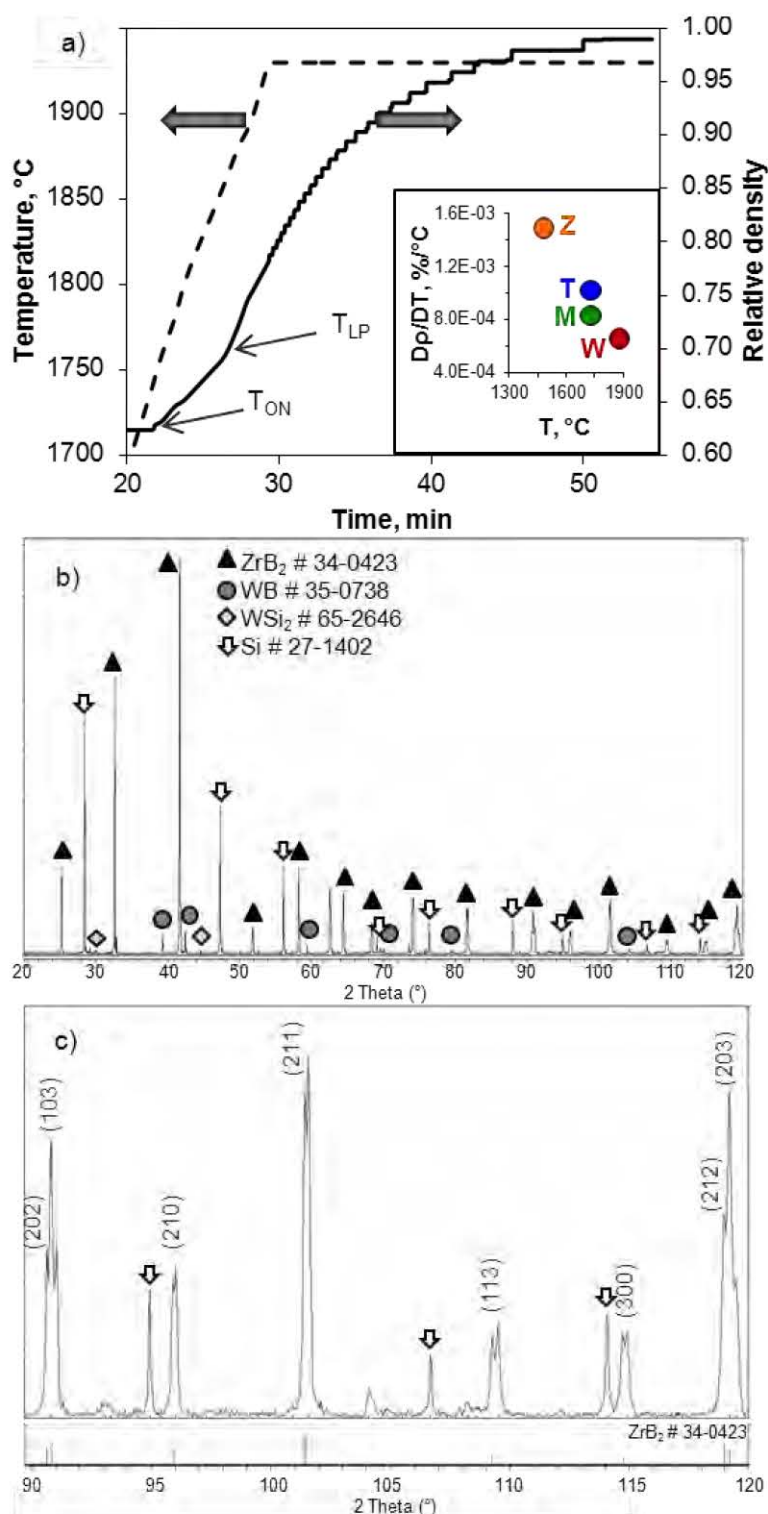
The densification curve recorded during hot pressing run is depicted in Fig. 2a where density and temperature are reported as a function of time.

It can be read that significant shrinkage started just above 1750°C (T_{ON}), which is a relatively high temperature as compared to other transition metal silicides (ZrSi_2 : 1350°C , MoSi_2 : 1500°C).^{16,17} The inset in Fig. 2a shows the maximum densification rate for different ZrB_2 composites containing the same amount of various silicides, i.e. ZrSi_2 , MoSi_2 , TaSi_2 and WSi_2 .^{16,17} It is evident that WSi_2 , besides favoring the sintering process at the highest temperature, also enables the densification at the lowest speed. The sintering process proceeded at the same rate up to 1850°C , after which a steeper slope indicated the improvement of densification mechanisms, possibly assisted by liquid phases (T_{LP}). At 1930°C the relative density was around 87% of the theoretical value, but a dwell at this temperature for 25 minute enabled the achievement of the fully density.

3.1.2. Microstructural features of ZBW

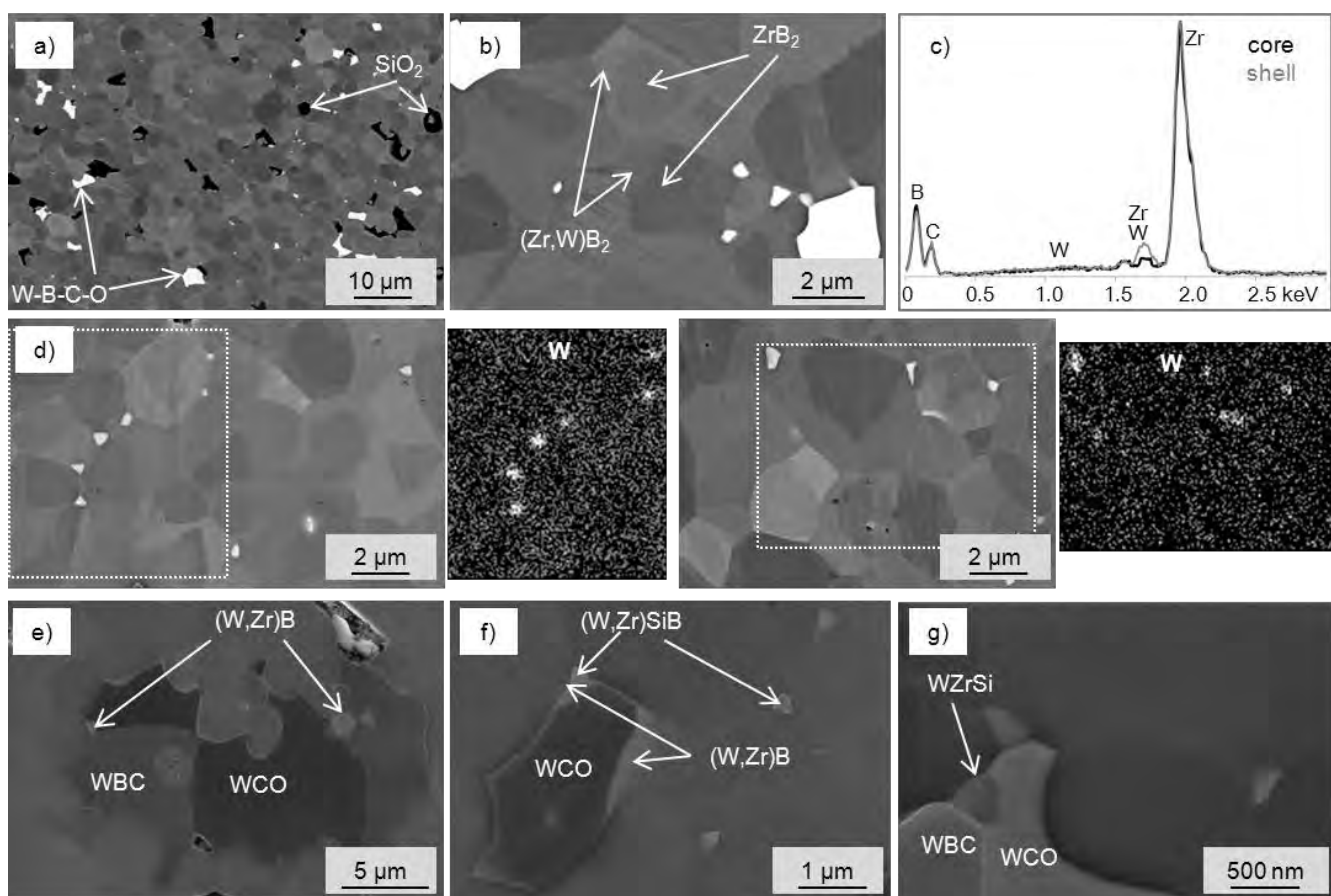
The x-ray diffraction pattern of the composite is reported in Fig. 2b; a Si standard was placed on the top of the specimen in order to detect any peak shift. In the whole 2-Theta range, ZrB_2 was the main crystalline phases, but reflections of tetragonal WB were found too, whilst WSi_2 was present just in traces. At high 2-Theta angles, above 80° (Fig.2c), another phase is clearly visible on the right of ZrB_2 (PDF# 34-0423). The unit cell parameters of this newly formed phase were $a=3.1653$ and $c=3.5244$ Å, i.e. slightly shorter than those of pure ZrB_2 ($a=3.1690$ and $c=3.5300$ Å), which indicates a contraction of the unit cell. The presence of these additional reflections was interpreted as due to the formation of a $(\text{Zr},\text{W})\text{B}_2$ solid solution. However, the exact composition of this new phase was not computable through Vegard's rule, owing to the too small amount of W entered into ZrB_2 lattice, within the instrumental error.

Figure 2: a) Densification curve recorded during hot pressing. T_{ON} : temperature at which shrinkage begins, T_{LP} : temperature at which liquid phase forms. In the inset: plot of the maximum densification rate as a function of the temperature for different silicides; Z: $ZrSi_2$, T: $TaSi_2$, M: $MoSi_2$, W: WSi_2 . b) X-ray diffraction pattern of the sintered composite showing the crystalline phases and c) ZrB_2 peaks splitting at high 2-Theta angles.



Images of the microstructure by SEM are shown in Fig.3. Fig. 3a shows an overall view of the polished section: the grains are rounded with average dimensions of $3.1 \pm 0.8 \mu\text{m}$ and are homogeneously surrounded by a brighter gray phase. Different grey levels in the matrix are due to different grains orientation.

Figure 3: SEM images of the sintered ceramic showing a) the overall microstructure, b) the matrix morphology with c) EDX spectra of core and shell. d) Elemental mapping of the matrix showing the distribution of W in the shell. e)-g) secondary W-based phases.

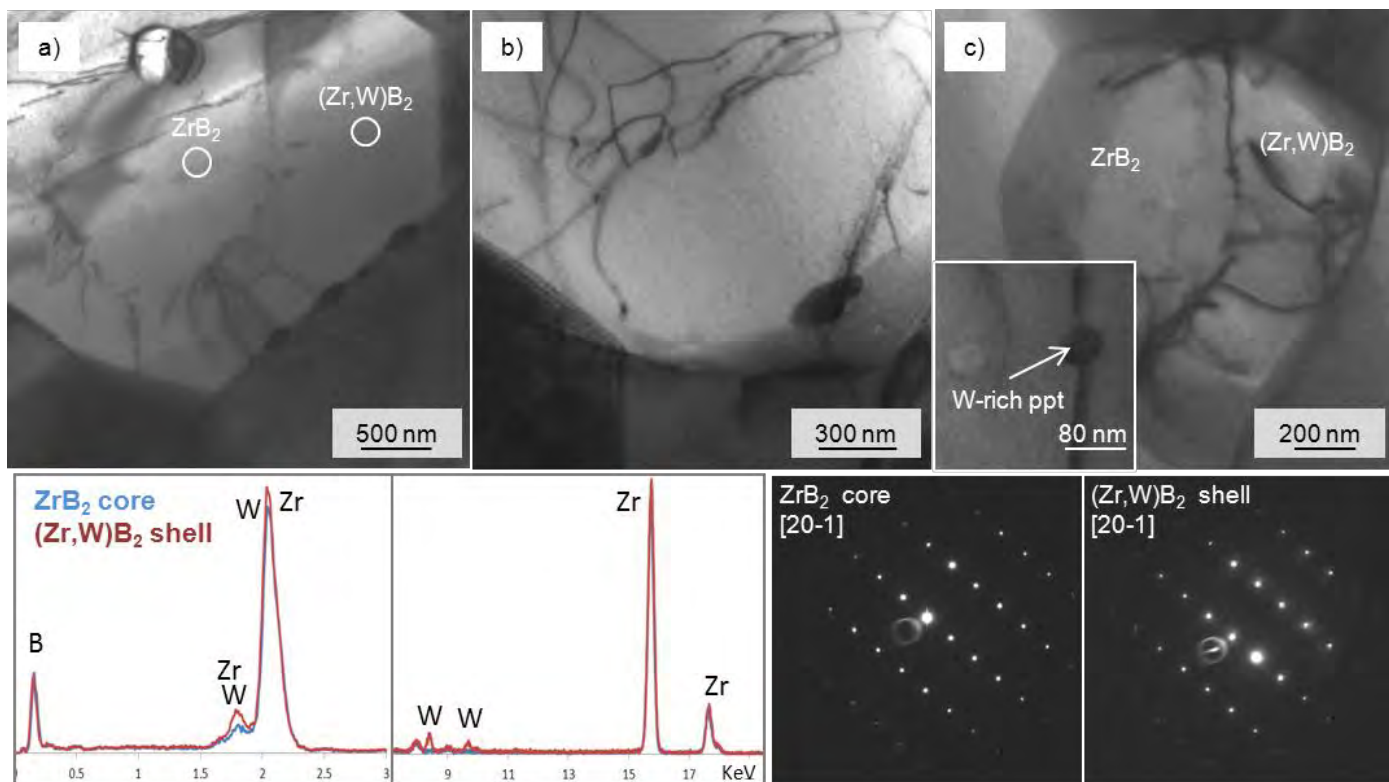


The main secondary phases are about 2 vol% of silica, with dark contrast, and 3.5% of a white phase containing W,B,C,O. Small SiC grains were often found next to silica pockets. No major defects or porosity were observed. Fig. 3b discloses the morphology of the matrix: the core is ZrB_2 , whilst the outer brighter region, the shell, is ZrB_2 containing 2 at% of W, resulting in a solid solution like $(\text{Zr}_{0.98}\text{W}_{0.02})\text{B}_2$, as the EDS spectra and elemental mapping in Fig. 3c and 2d demonstrate. The presence of carbon in the spectra is due to beam contamination. Images acquired with in lens electrons, Figs. 3e-g, revealed that the bright phase observed by backscattered electrons in Fig. 2a is actually composed of several other phases: the largest areas are WCO and WBC, always adjacent to each other's and with low dihedral angles suggesting solidification from liquid phase. At the extremities, brighter regions with generally elongated shape are WB with Zr traces, Fig. 3e,f, whilst the bright phases found at the triple points with concave

shape are mixed Zr,W-silicides with stoichiometry difficult to identify owing to the superimposition of W and Si lines, Fig. 3g.

TEM investigations enabled a more precise definition of the constituent phases. Examples of the matrix grain morphology are reported in Fig. 4a-c. A peculiar feature of the diboride grains was the presence of dislocations in the shell. Similarly to previous study on analogous composites,^{16,17} core and shell were epitaxial, as disclosed by electron diffraction patterns, Fig. 4. In spite of that, no modification of lattice parameters was detected by SAEDP technique, owing to the small differences in atomic radii of Zr and W (0.160 and 0.137 nm, respectively) and to the little W content in the shell. The boundary between core and shell was quite sharp and defined by dislocations pile up, as depicted in Fig.4a-c. TEM EDS quantitative analyses performed on core and shell, confirmed around 2 wt% of W in the solid solution, Fig. 4.

Figure 4: a)-c) TEM images showing the core-shell structure of the matrix of the sintered ceramic with EDX spectra at low and high voltage and SAEDP taken from a) confirming epitaxy between ZrB_2 and $(Zr,W)B_2$. The inset in c) shows a W-rich precipitate occasionally found at the core-shell interface. ppt=precipitate.



The study of secondary phases and triple points by electron diffraction and EDS confirmed the formation of large WB grains, with WC or WSi_2 smaller grains at the apical parts, Fig. 5a-e and the segregation of ZrO_2 or impurities, like Fe-rich phases, at the triple junctions, Fig. 5f. Analyses of the interfaces revealed non wetted grain boundaries between

adjacent $(\text{Zr},\text{W})\text{B}_2$ grains, Fig. 6a-f, and between WB and $(\text{Zr},\text{W})\text{B}_2$, Fig. 6g-i. Clean interfaces were found both in case of simple triple junctions, Fig. 6a-c, and in case of segregation of secondary phases at the triple points, Fig. 6d-f. Strain contrasts were generally observed in ZrB_2 grains when other phases crystallized at the junctions, Figs. 5a,e and 6d. To obtain statistically valid results, several interfaces were analyzed and no amorphous film was found between $(\text{Zr},\text{W})\text{B}_2$, $(\text{Zr},\text{W})\text{C}$, $(\text{W},\text{Zr})\text{Si}_2$ and WB grains, as confirmed in Fig. 7.

Figure 5: TEM images of the secondary phases with EDX spectra and diffraction patterns showing the presence of WB, WC, WSi_2 and residual ZrO_2 .

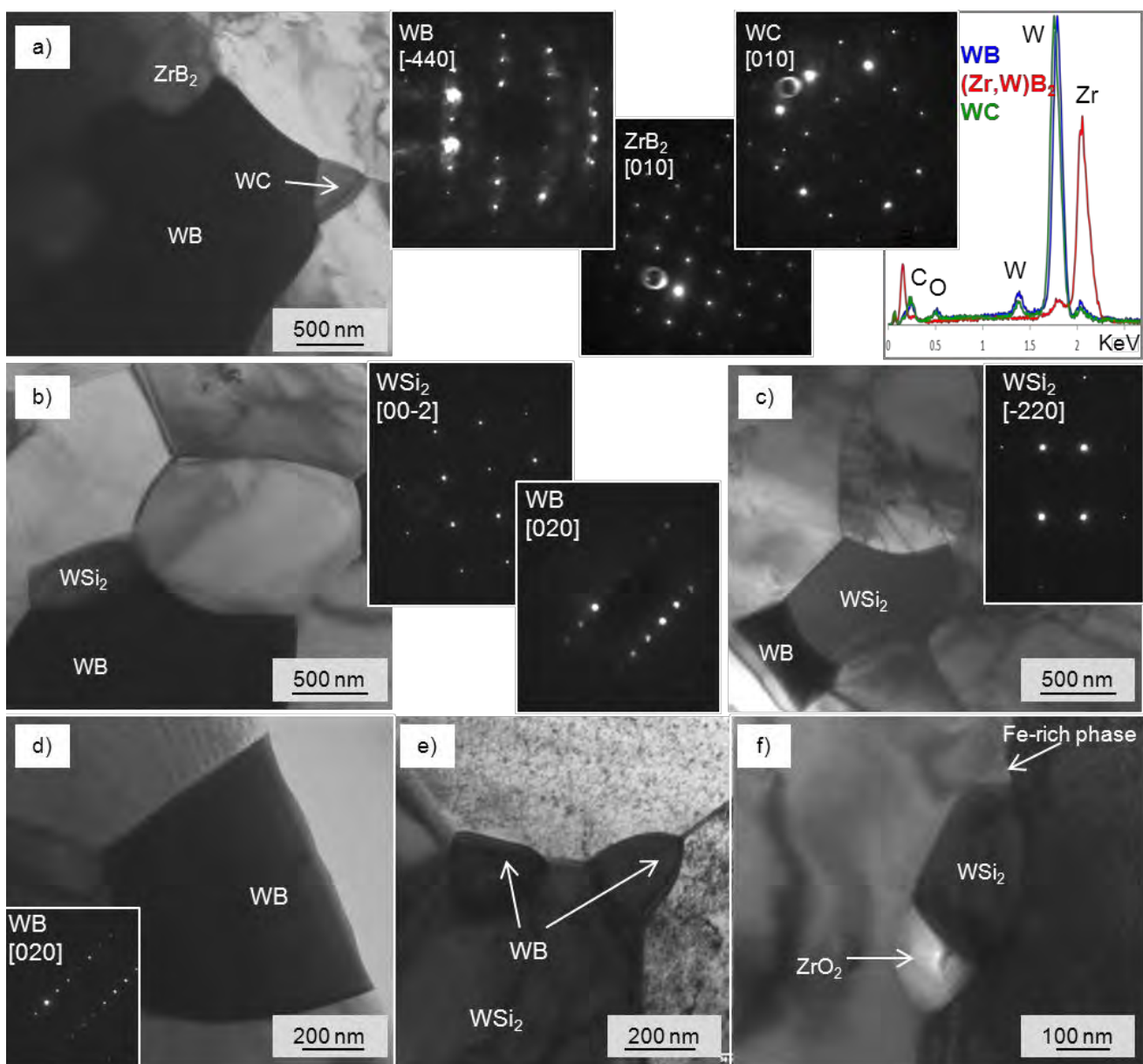


Figure 6: TEM and HRTEM images of the triple point junctions showing clean grain boundaries between a)-f) adjacent $(\text{Zr},\text{W})\text{B}_2$ grains and g)-i) between WB and $(\text{Zr},\text{W})\text{B}_2$.

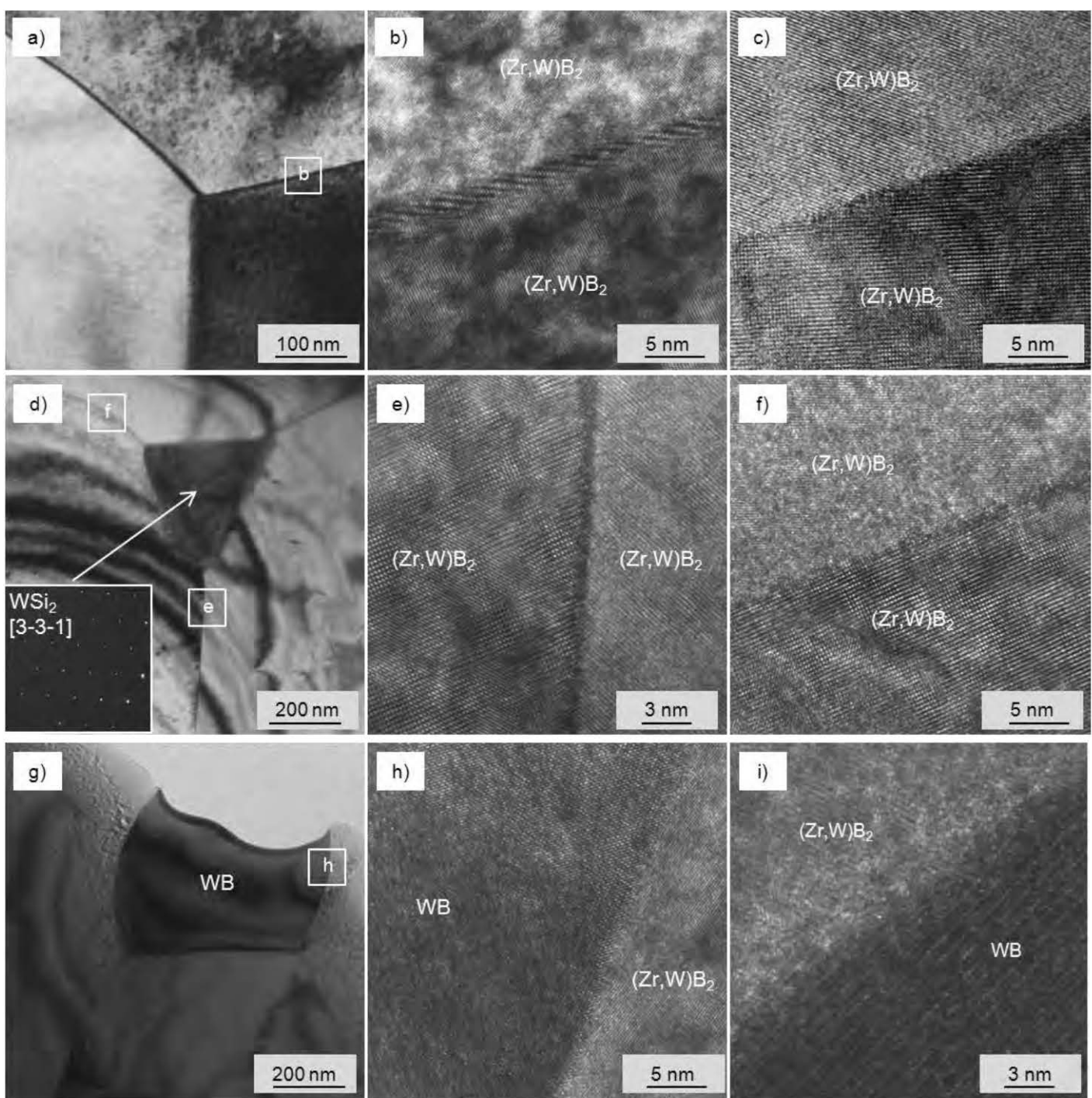
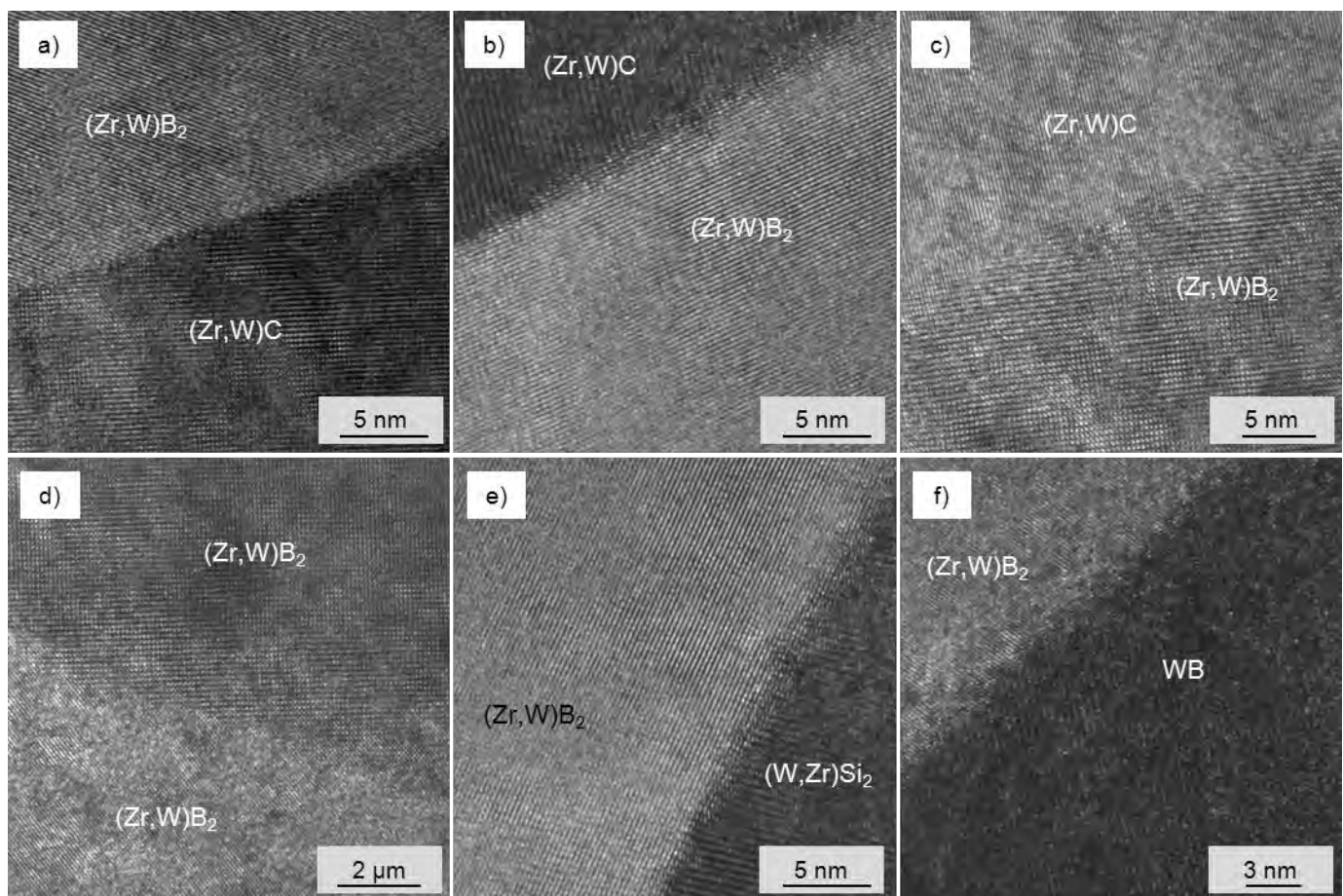


Figure 7: HR-TEM images showing clean grain boundaries between $(\text{Zr},\text{W})\text{B}_2$, $(\text{Zr},\text{W})\text{C}$, $(\text{W},\text{Zr})\text{Si}_2$ and WB .



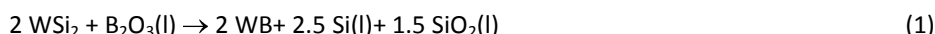
3.1.3. Microstructure evolution during densification

In the sintered material, a notable change of the microstructural features occurred, which is strictly related to the densification mechanisms activated by WSi_2 . Addition of metal disilicides, MeSi_2 ($\text{Me} = \text{Ti, Cr, Zr, Mo, Ta, W}$), to TiB_2 and ZrB_2 was first investigated by Pastor and Meyer in 1974¹⁸ and, according to their studies, densification of borides with MeSi_2 was successful because it was conducted at temperatures close to the MeSi_2 melting point. For WSi_2 , however, full densification is achieved although the temperature range is well below its melting point, 2160°C.¹⁵ However, low dihedral angles suggest WSi_2 was ductile at the sintering temperature.

According to the phase diagrams involving W-Si ,¹⁹ W-B ,²⁰ W-C ,²⁰ no liquid phases are predicted to form below 1930°C. Also the eutectic at 1275°C between the oxides covering the particles, WO_3 and ZrO_2 ,²¹ doesn't seem to affect the start of the shrinkage occurring at 1750°C, T_{ON} in Fig. 2a. Only Si , SiO_2 and B_2O_3 are liquid below the sintering temperature. However, the presence of W-based phases at the triple junctions containing Zr traces suggests the existence of some liquid phases in which ZrB_2 is partially soluble in. Similar to MoSi_2 , and TaSi_2 ,^{16,17} the densification of

DATE	03/06/15
------	----------

$\text{ZrB}_2\text{-WSi}_2$ composite is presumed to be assisted by a transient liquid phase, due to the reaction between WSi_2 and the surface oxide impurities covering the diboride particles, according to reaction (1):



Reaction (1) implies removal of B_2O_3 from boride particle surface, formation of Si- and Si-O-based liquids and is favorable in the whole sintering temperature range, -48 kJ/mol at 1700°C. Reaction (1) is not exhaustive and, in the reducing environment of the hot pressing chamber, it is likely that variants of the same reaction locally occur, for example resulting in the formation of WO_3 , according to reaction (2):



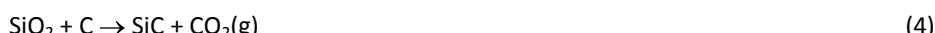
which has a negative Gibbs free energy as well, -36 kJ/mol at 1700°C.

Nevertheless, all these intermediate phases concur to the formation of liquid phase at temperature around 1850°C, T_{LP} in Fig. 1a, that promotes mass transfer mechanisms, by partial dissolution of the boride matrix.

A distinctive feature of the $\text{ZrB}_2\text{-WSi}_2$ composites is the formation of $(\text{Zr,W})\text{B}_2$ solid solution around ZrB_2 grains, which was already found for other $\text{ZrB}_2\text{-MeSi}_2$ and it was also assessed that $(\text{Zr,Me})\text{B}_2$ shells grow epitaxially onto ZrB_2 cores.^{16,17} This grains morphology suggests again a solution re-precipitation mechanism, summarized by reaction (3), even if diffusion of W into the diboride lattice and Zr into the silicide cannot be ruled out, as previously observed for analogous systems involving different transition metal cations which are close in the periodic table:^{16,17}



During cooling, the transient liquid-phase solidifies, resulting in the formation of discrete crystalline phases, such as the observed WB, WC. At the same time, the carbo-reduction of SiO_2 - and WO_3 -based species to SiC and WC is favorable too:



The chemistry of the crystalline phases at the triple point junction seems to confirm the above reactions to occur.

We can state that, compared to previously studied systems, the densification of this one with WSi_2 proceeds through more sluggish mechanisms even if the sintering temperatures is higher, see the inset in Fig. 2a. This can be determined by combination of factors: the initial liquid amount is limited and more refractory, its viscosity progressively increases owing to the incorporation of higher and higher amount of cations from boride and silicides, and also silica glass at such high temperatures tends to be carbo-reduced to SiC. In addition, the study of the interfaces also reveals that the liquid doesn't wet the matrix, as all the grain boundaries were clean from any intergranular phases.

DATE	03/06/15
------	----------

RT - 2015/13	TECHNICAL REPORT: FA8655-12-1-3004	Pag. 31/91
--------------	---	------------

3.1.4. Mechanical properties

The mechanical properties measured on the $\text{ZrB}_2\text{-WSi}_2$ composite are reported in Table 2 together with properties of other ZrB_2 ceramics sintered with addition of silicides (MoSi_2 , TaSi_2) or W-compounds (WC).^{11,16,22}

Table 2: Composition, mean grain size and mechanical properties of $\text{ZrB}_2\text{-WSi}_2$ ceramic compared to other ZrB_2 -composites containing either transition metal silicides or W-compounds. m.g.s.: mean grain size, K_{Ic} : fracture toughness measured by chevron notch technique, HV: microhardness (1 kg), σ : 4-point flexural strength at room temperature or at 1500°C in air, PS: pressureless sintering.

Composition vol%	ZrB_2 m.g.s. μm	K_{Ic} MPa·Vm	HV GPa	σ_{RT} MPa	σ_{1500} MPa	Ref.
$\text{ZrB}_2\text{+15 WSi}_2$	3.1 ± 0.8	3.62 ± 0.35	18.3 ± 0.4	641 ± 19	537 ± 16	this work
$\text{ZrB}_2\text{+15 MoSi}_2$	2.4	3.50 ± 0.60	14.9 ± 0.5	704 ± 98	333 ± 31	16
$\text{ZrB}_2\text{+15 TaSi}_2$	2.0	3.80 ± 0.10	17.8 ± 0.5	840 ± 33	374 ± 5	16
$\text{ZrB}_2\text{+3 WC (PS)}$	9.1 ± 5.6	-	14.5 ± 2.6	444 ± 30	-	16
$\text{ZrB}_2\text{+3 WC}$	4.0 ± 1.2	-	23.0 ± 0.9	565 ± 53	-	16
$\text{ZrB}_2\text{+20SiC+5WC}$	1.1	-	-	605^{b}	640^{bc}	11
($\text{ZrB}_2\text{+20SiC})\text{+10WC}$	-	$6.5\pm0.2^{\text{a}}$	13.9 ± 0.2	$518\pm10^{\text{b}}$		22

^aSEVNB

^b3-pt bending strength

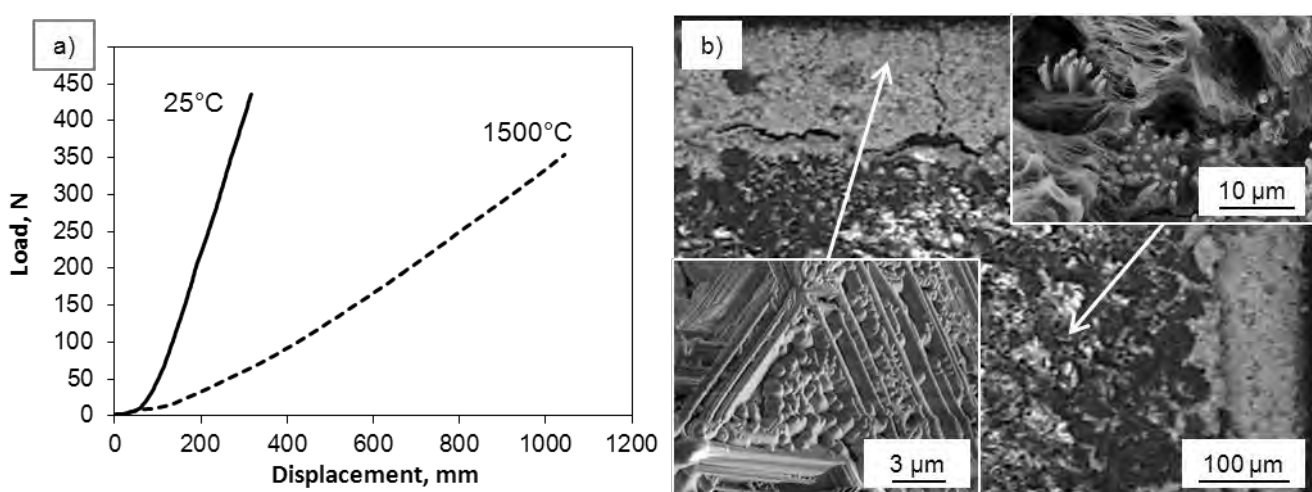
^cAr

As expected, the fracture toughness of this composite was in the range of other ZrB_2 -based ceramics measured with the same chevron v-notched method, $3.6 \text{ MPa}\cdot\text{m}^{1/2}$.¹⁶ The hardness, around 18 GPa, resulted higher than other ZrB_2 -ceramics sintered with addition of other transition metal silicides,¹⁶ despite the higher grain size and 2 vol% of silica, probably thanks to the presence of other hard secondary phases, like WB and WC. The room temperature flexural strength was 640 with very low standard deviation, less than 3%, confirming a uniform microstructure without large flaws.

The featuring characteristic of this composite is its very high refractoriness at 1500°C in air, as testified by fracture strength of 540 MPa at this temperature, namely 84% of the room temperature value, and the linearity of the load-displacement curve, displayed in Fig. 8a. Excellent results were obtained also by Zhou and co-workers¹¹ who even measured a strength increase, however those data are not directly comparable with those of the present work, since their tests were performed in argon and in 3-point bending. An example of the fracture surface after bending test at 1500°C is shown in Fig. 8b. On the cross section, about 150 μm of material underwent oxidation and this layer was formed by ZrO_2 rounded grains containing W traces and covered by H_3BO_3 acicular crystals deriving from hydration of B_2O_3 after exposure to humidity in the environment. This feature is quite surprising, since B_2O_3 has low vapor tension and evaporates above 1000°C. The fact that we still see crystalline boron oxide in the oxide scale could be due to the presence of tungsten oxide which reduced the volatility of the borate glass, as previously stated in a dedicated study.¹³

DATE	03/06/15
------	----------

Figure 8: a) Load-displacement curves for flexural strength at room temperature and at 1500°C in air. b) SEM images of the cross section of a bar after flexural strength testing at 1500°C showing the presence of acicular BO-based crystals.



The strength retention at high temperature is usually attributed to the formation of a protective oxide scale,²³ crack healing or to the release of internal residual stresses.²⁴ In this system, neither amorphous phase nor glassy phases were found in the microstructure. Crack healing can be therefore ruled out as strengthening mechanism. Regarding the relaxation of the internal residual stresses, the test temperature of our specimens, 1500°C, was not close to the material sintering temperature, 1930°C, so that the relaxation could not have been truly effective.

In a recent TEM study conducted upon high temperature flexural strength on ZrB₂-B₄C composites with clean grain boundaries like in the present case,⁹ it was pointed out that, below a testing temperature of 1600°C, no interconnected cavities developed at the grain junctions and that the stress induced by the load was progressively accommodated by ZrB₂ grains plastic deformation, due to the generation and flow of dislocations. This mechanism promoted a strength increase at high temperature in that composite.⁹ In the ceramic of the present work, we observed dislocation networks already after sintering, as Fig. 3 clearly shows. The absorption of small amount of mechanical energy during the flexural test by dislocation flow and multiplication could give a partial contribution to the remarkable high temperature strength of ZrB₂-WSi₂ composite. Also the clean grain boundaries and the presence of highly refractory secondary phases at the triple points, like WB, possessing a melting point of 2655°C,²⁰ or WC, 2870°C,²⁰ Fig. 5, could be beneficial for the high temperature strength by preventing grain boundary sliding at high temperature.

In conclusion, the high refractoriness of the ZrB₂-WSi₂ ceramic is very likely a combination of multiple factors: the formation of a stable and protective borate glass on the surface during oxidation, the intrinsic refractoriness of the crystalline compounds, the absence of amorphous phases at the grain boundaries and the tendency of the matrix grain to absorb energy by plastic deformation due to dislocations flow.

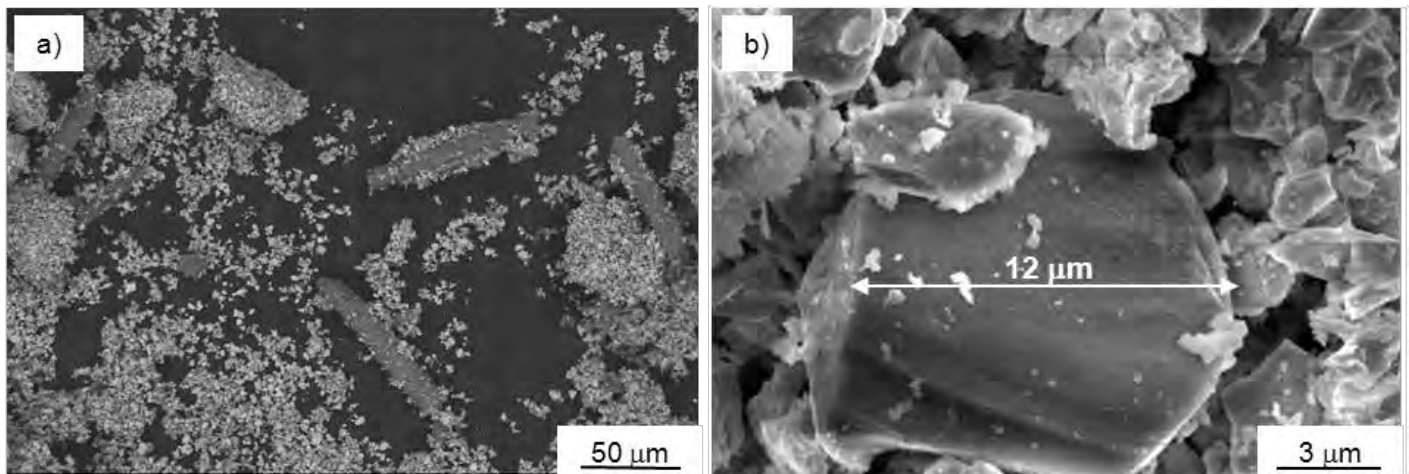
3.1.5. Conclusions on ZBW

A ZrB₂-based ceramic was hot pressed to full density at 1930°C through addition of WSi₂. Although the high sintering temperature, the microstructure resulted fine and homogeneous, thanks to the beneficial effect of WSi₂ and its derivative products. Core-shell structures were found in the boride matrix and TEM analyses revealed the segregation of highly refractory compounds at the triple points, like WB, WC and W-Si phases with clean grain boundaries. These features resulted favorable for the high temperature performances. In particular, the mechanical strength at 1500°C in air was 540 MPa, about 84% of the room temperature value. Possible reasons explaining this behavior were the incorporation of W in the borate glass during oxidation, which increased the oxide layer stability and protective action, and to the presence of clean grain boundaries and highly refractory secondary phases at the triple junctions.

3.2. ZrB₂ + SiC fiber

Following previous results on the addition of chopped fiber to borides,^{1,28} the effect of another type of chopped SiC fiber (Hi-Nicalon S) in a ZrB₂ matrix fiber was studied, Fig. 9. Two different sintering additives were explored: Si₃N₄ and ZrSi₂. Then, preliminary studies were conducted on a composite containing long BN-coated Hi-Nicalon fiber with 0/90°C architecture. A summary of the ZrB₂ reinforced ceramics object of this work is reported in Table 3.

Figure 9: a) Low and b) high magnification of Hi-Nicalon S fiber after in house chopping and mixing with ZrB₂ powder.



DATE	03/06/15
------	----------

Table 3: Composition, sintering parameters, relative density and mechanical properties of SiC fiber-reinforced ZrB₂ ceramics.

Label	s.a. vol%	Fiber, vol%	Type	Sintering, °C, MPa, min	Rel. density %	K _{IC} MPa·Vm	σ _{RT} , MPa	σ ₁₂₀₀ , MPa	σ ₁₅₀₀ , MPa	Ref.
ZBS-H	5 Si ₃ N ₄	10 Hi-Nicalon	short	1730,40,11	97.8	5.32±0.33	389±37	409±9	-	1
ZBS-HS	5 Si ₃ N ₄	10 Hi-Nicalon S	short	1720,40,9	96.5	4.61±0.06	455±14	362	54	pw
ZBZ-HS	10 ZrSi ₂	10 Hi-Nicalon S	short	1550,40,10	98.0	4.49±0.10	480±12	367	47	pw
ZBZ-iH*	10 ZrSi ₂	25 (BN)Hi-Nicalon	long	1450,32,40	98.0	4.54±0.48* ^B	192±53 ^A 127±55 ^B	-	-	pw
ZBZ-H	10 ZrSi ₂	20 Hi-Nicalon	short	1650,50,8	99.0	6.24±0.35	385±13	379±15	-	1
ZBZ-T	10 ZrSi ₂	15 Tyranno SA3	short	1600,50,11	99.0	5.07±0.19	457±14	417±11	110±8	28
ZBZ-iHS	10 ZrSi ₂	10 (BN)Hi-Nicalon S	short	1500,50,12	99.0	5.15±0.32	535±18	391±11	91±21	28

*40x3x4

^A bar cut A side^B bar cut B side

3.2.1. ZrB₂ + short Hi-Nicalon S

The composite sintered with Si₃N₄, ZBS-HS in Table 3, achieved a density higher than 96% after sintering at 1720°C for 9 min. The fracture surface reported in Fig. 10a displays a dense microstructure with protruding fiber, indicating a weak fiber-matrix bonding. SEM images of the fiber aspect are reported in Fig. 10b-d and evidence strong microstructural modification despite the high refractoriness of the Hi-Nicalon S fiber, they maintained a rounded shape but irregular edges developed. The matrix was scattered of secondary phases like ZrO₂, SiC, BN and ZrN and SiO-based glass (Fig. 11a-c) and, similar to analogous composites, the interfaces BN-ZrB₂ were often found to be wetted, Fig. 11d-i.

Looking closer at the matrix-fiber interface in Fig. 12 it can be noticed that about 1-2 μm around the fiber diameter underwent morphological changes, the edges were curly, indicating liquid phase exudation and solidification, reaction phases were trapped inside the fiber and the SiC crystallites coarsened and coalesced. The particles trapped in the fiber were identified as Si and ZrSi₂ with Co, Fe and O traces, as confirmed by EDS and diffraction pattern in Fig. 12. STEM analyses across a fiber are displayed in Fig. 13 and underline the presence of Fe in the particles, probably coming from impurities in the starting powders, homogeneous distribution of Si, slight C impoverishment toward the edge and simultaneous O enrichment. Porosity areas running around the fiber are visible too in Fig. 10d and 13, which probably caused the fiber pullout during fracture. The microstructural evolution of the fiber structure is visible in Fig. 14a-d, where it can be rapidly observed that SiC crystallites coarsened from the core towards the edge and passed from around 24 nm to around 140 nm and evolved to platelets in contact with the matrix. Magnifications of fiber core in Fig. 14e-h show triple point junctions and partially amorphous C-rich phase.

Examples of fiber-matrix interfaces are reported in Fig. 15, even if most of the time, SiC platelets were found interposed between the actual fiber and ZrB₂.

Figure 10: a) Fracture surface and b)-d) polished surfaces of ZrB_2 composite containing Hi-Nicalon S fiber and Si_3N_4 as sintering additive. b) Overview of a fiber section, c) magnification of fiber-matrix interface and d) reaction products trapped inside the fiber

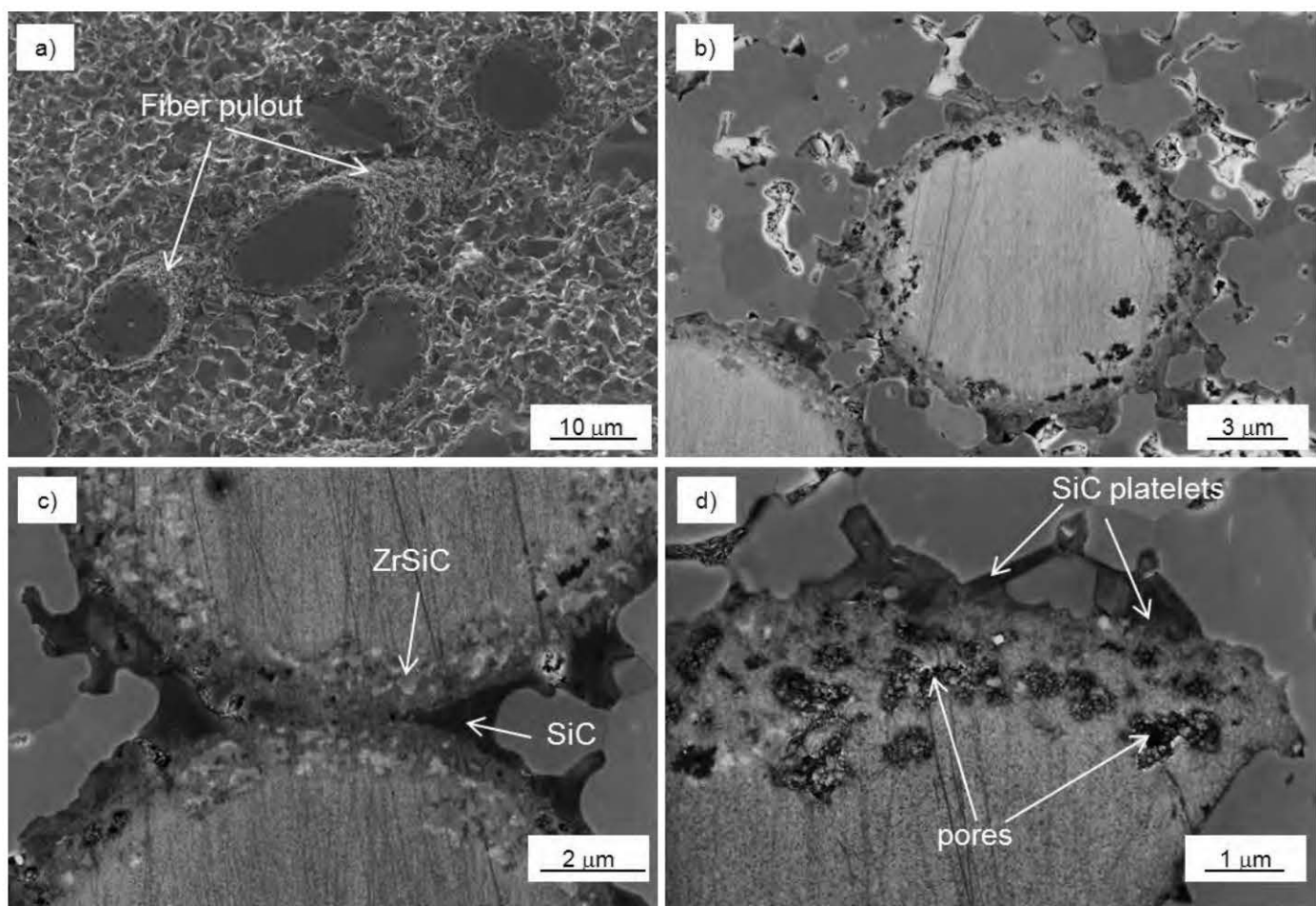


Figure 11: TEM images showing a)-c) secondary phases in the matrix and d)-i) examples of BN/ZrB₂ wetted interfaces with e) diffraction patterns and f) EDS spectra of the amorphous phase and BN.

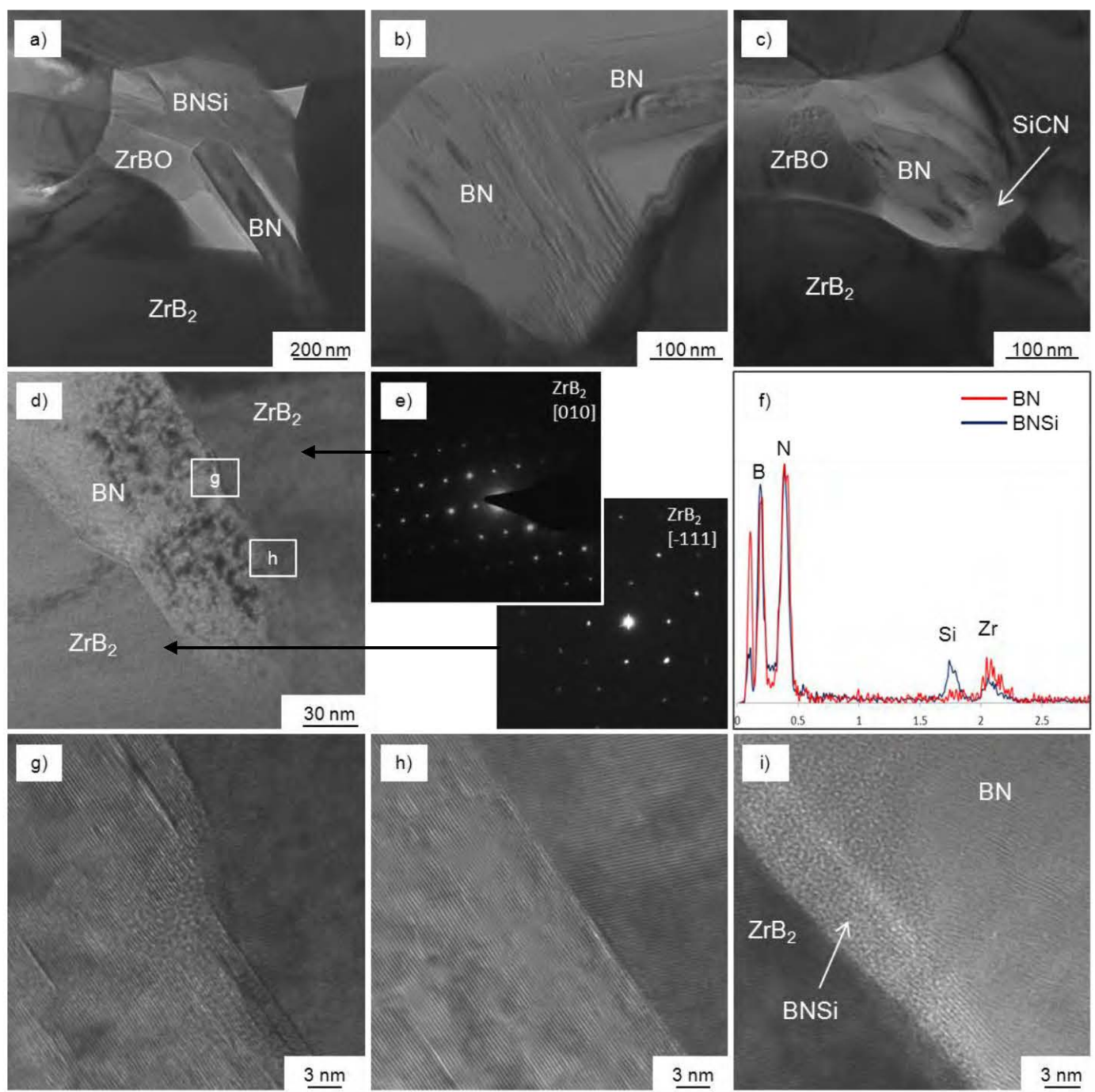


Figure 12: a)-d) TEM images showing particles trapped in the fiber identified as $ZrSi_2$, Si. e)-f) Si_3N_4 residuals are also found at the fiber-matrix interface.

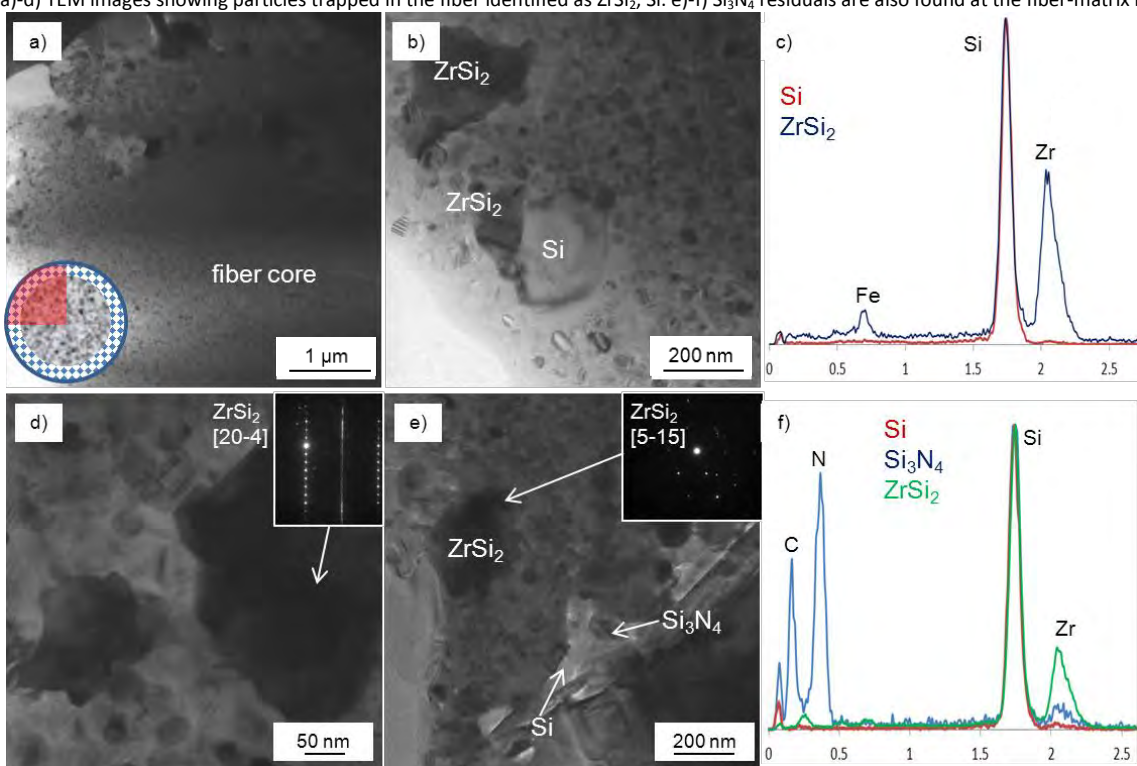


Figure 13: STEM image of a fiber edge in ZBS-HS with EDS elemental mapping.

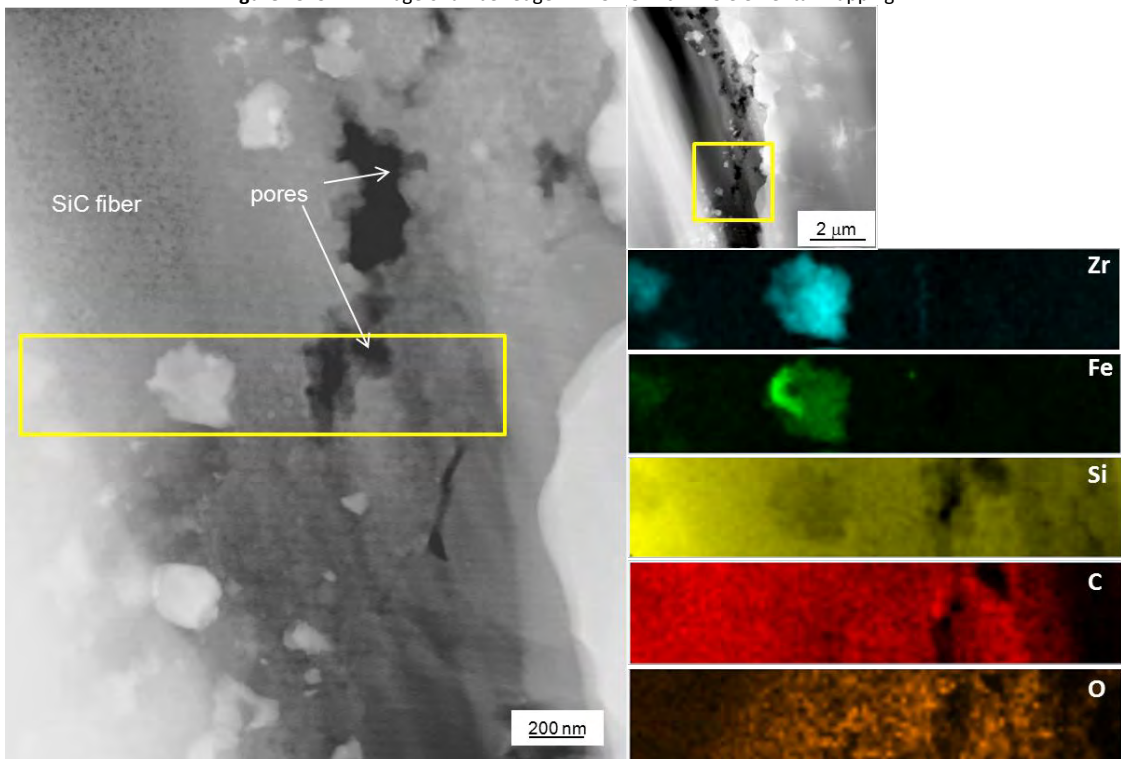


Figure 14: a)-d) Microstructure of a SiC fiber in ZBS-HS moving from the core outwards with corresponding diffraction patterns showing improved crystallinity. e-h) magnification of fiber core showing triple point junctions and partially amorphous C-rich phase.

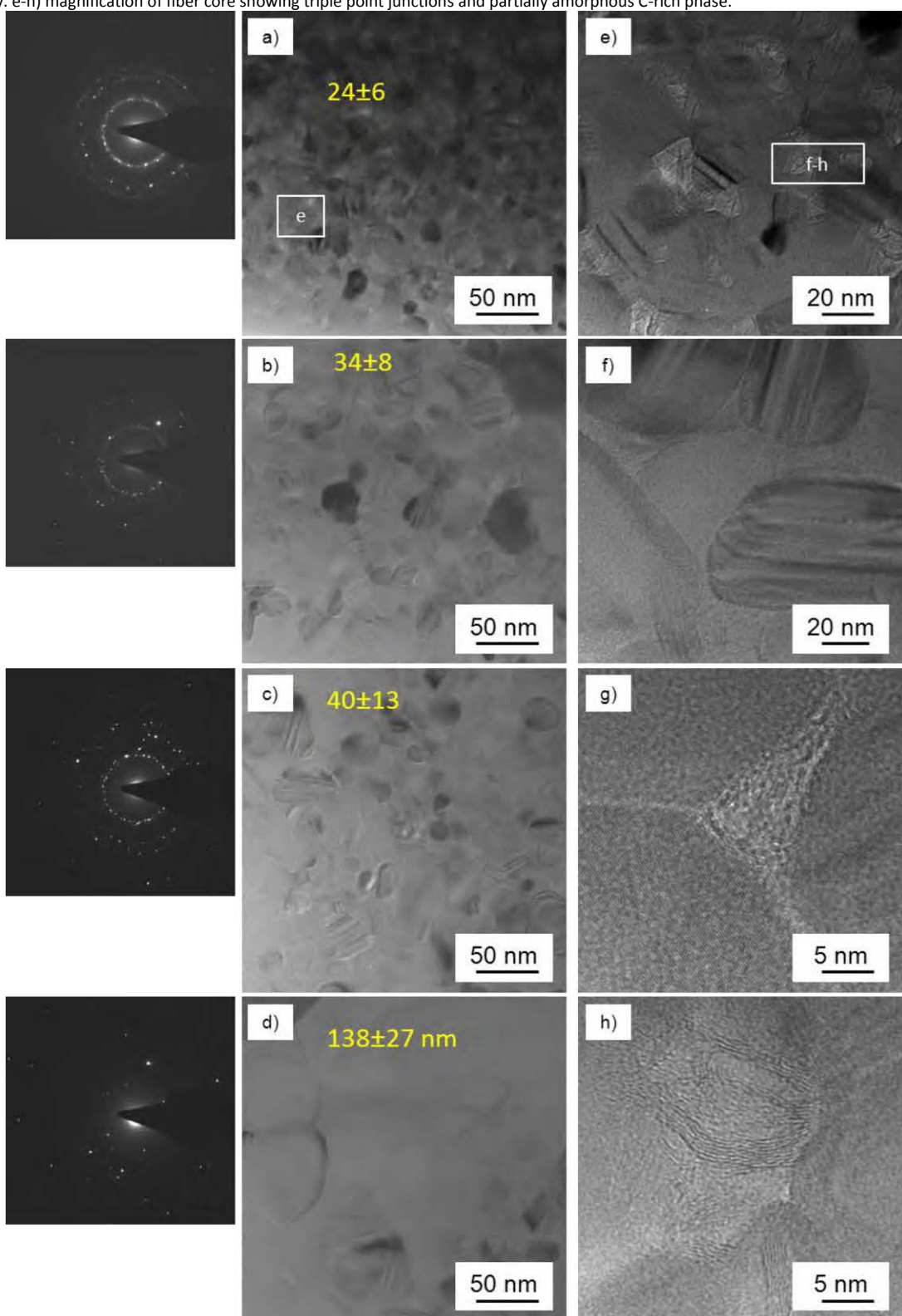
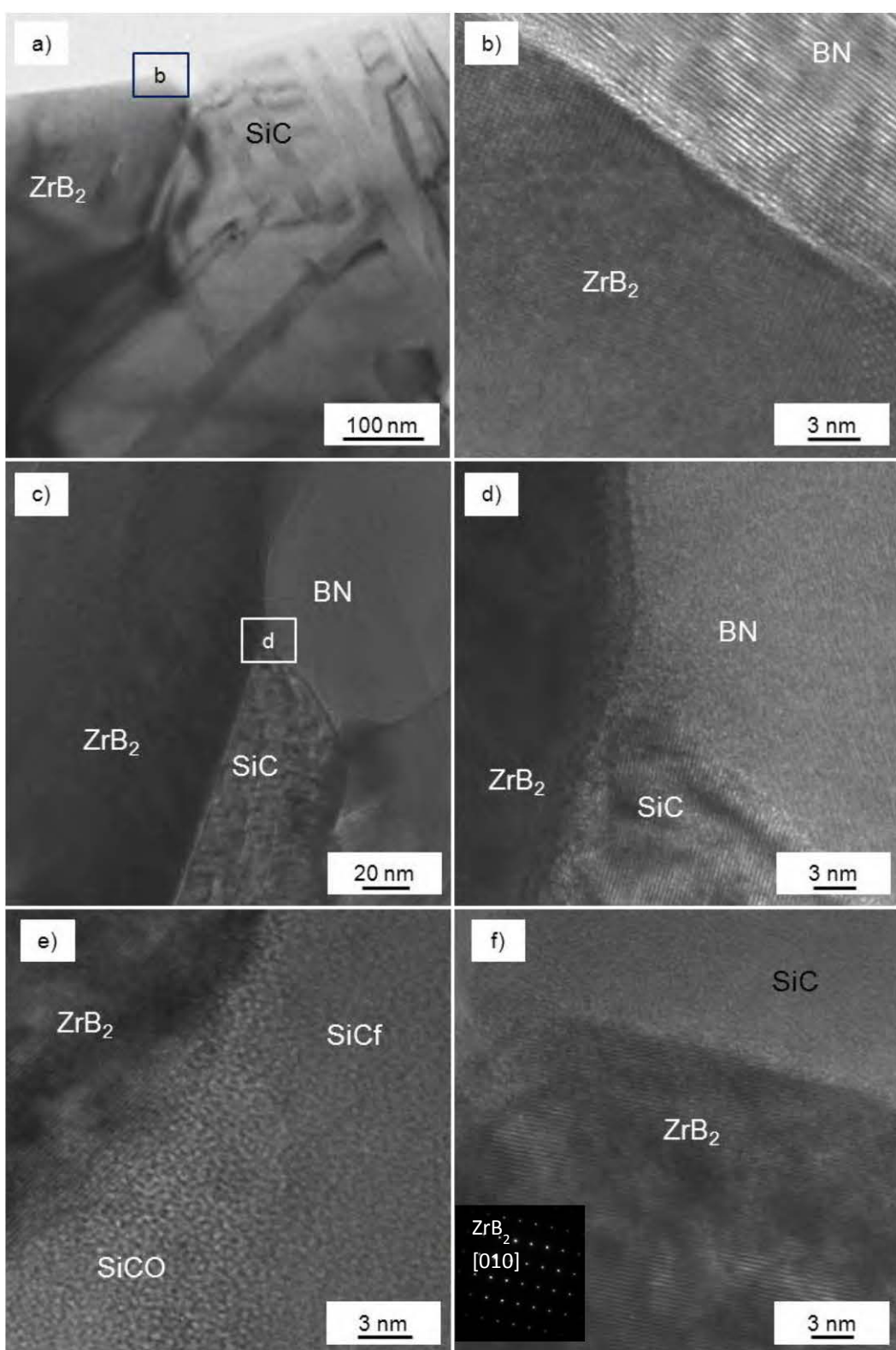
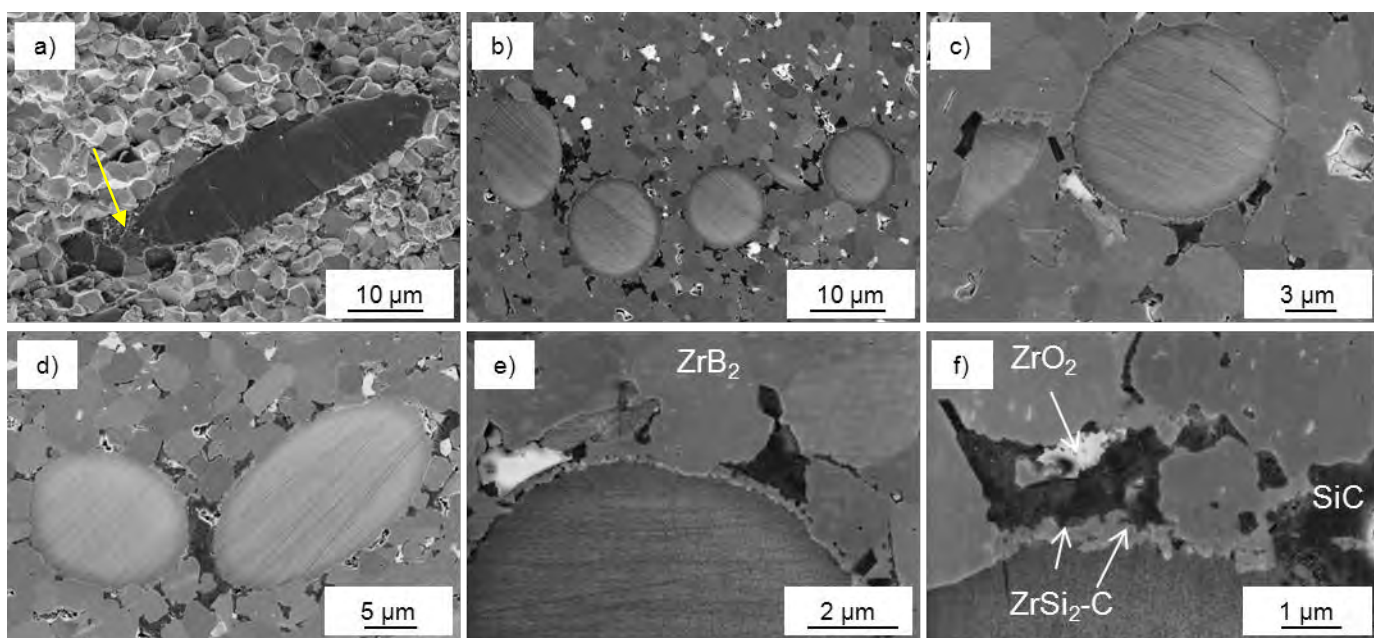


Figure 15: Examples of matrix/fiber interfaces in ZBS-HS showing wetted grain boundaries.



The composite based on ZrB_2 with Hi-Nicalon S and sintered with ZrSi_2 , ZBZ-HS in Table 3, achieved a density of 98% after sintering at 1550°C for 10 min. Also for this material fiber detachment from the matrix occurred, as indicated by the arrow in Fig. 16a, but on the other hand the fiber maintained the pristine aspect and shape, Fig. 16b. Often, when the fiber touched each other, areas of SiC with elongated platelets developed, as that depicted in Fig. 16d. An interphase was found around the fiber also with this additive, with white contrast and composed by ZrSi_2 -based phase, Fig. 16e-f. The size of the crystallites was in this case more homogeneous throughout the fiber.

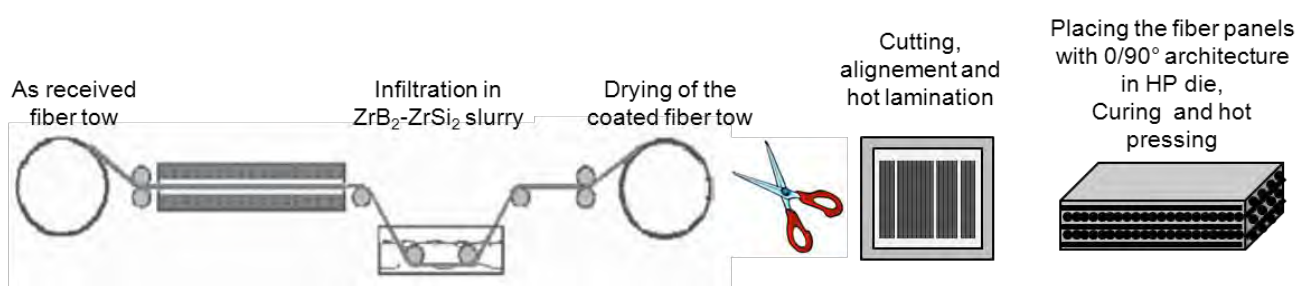
Figure 16: a) Fracture surface and b)-f) polished surfaces of ZrB_2 composite containing Hi-Nicalon S fiber and ZrSi_2 as sintering additive. b) Overview of the material microstructure, c) magnification of a fiber section, d) formation of SiC between two fibers, e) fiber-matrix interface and f) reaction products at the fiber edge.



3.2.2. ZrB_2 + long (BN)Hi-Nicalon

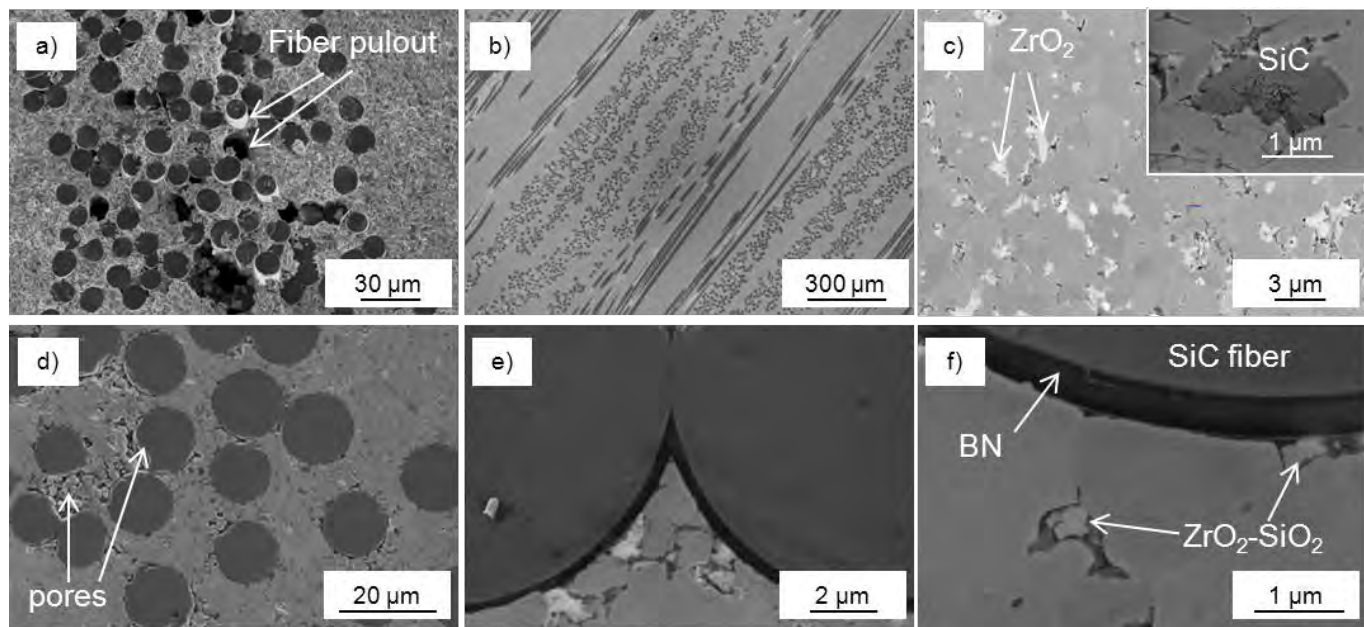
A long fiber composite was produced in MS&T, Rolla Labs, with a matrix of ZrB_2 with 10 vol% of ZrSi_2 as sintering additive and 25 vol% of BN-coated Hi-Nicalon fiber. A sketch of the fiber spool coating process with the ZrB_2 - ZrSi_2 slurry and following lamination and sintering is displayed in Fig. 17. Further details on the experimental procedure are provided in²⁹. A temperature of 1450°C was enough to enable full densification of this composite, that is 100°C lower than other ZrB_2 - ZrSi_2 - SiCf composites produced with conventional ball milling and hot pressing route.

Figure 17: Sketch of the experimental procedure for the fabrication of 0/90° long-fiber ZrB₂ composite.



The fracture surface of this composite is shown in Fig.18a and shows promising features, with notable fiber outer pullout. An overview at low magnification of the composite is shown in Fig. 18b, which confirm a good infiltration process and 0/90° fiber packing. Far from the fibers, the matrix is dense, Fig. 18c, but contains a high amount of ZrO₂, probably resulting from the long exposure to air during process. No free Si was found, but areas of dendritic SiC and SiO-based phases were observed, inset in Fig. 18c. In addition, microcracking was frequently seen, especially around the fiber. Close to the fiber, some porosity could be found, Fig. 18d. The BN coating well survived the process, was continuously surrounding each fiber for a thickness around 400 nm and was effecting in preventing any interaction between fiber and matrix or sintering additive, Fig. 18e-f.

Figure 18: a) Fracture surface and b-f) polished surfaces of ZrB₂ composite containing long BN-coated Hi-Nicalon fiber and ZrSi₂ as sintering additive. b) Overview of the material architecture, c) magnification of the matrix showing ZrO₂ and SiC aggregates, d) fiber distribution with trapped porosity, e) homogeneous BN coating around the fibers and f) efficient blockage of secondary phases at the coating interface.



TEM images collected in the matrix confirmed the presence of large amount of ZrO_2 and revealed the crystallinity of SiO_2 , which generally showed clean grain boundaries, Fig. 19a-c. However, SiO_2 was also found in amorphous state, trapped among ZrB_2 and ZrO_2 and containing N traces, Fig. 19d-f. The fiber-coating-matrix morphology was disclosed by TEM analysis in Fig. 20. The coating had a homogeneous thickness and was composed by BN with scattered dark particles identified as Si_3N_4 and Si-C-B-N, Fig. 20c-e. Examples of interfaces in high resolution mode between coating and matrix or between coating and fiber are reported in Fig. 21. It can be observed that the interface between coating and matrix is sharp and clean, Fig. 21a-c, whilst the boundary between fiber and coating is not so clear and amorphous phase is present, Fig. 21d-f. STEM analyses performed at the interface, Fig. 22, confirmed no diffusion of Zr through the coating or the fiber, whilst Si and C were detected in the coating and oxygen enrichment was distinguished in the fiber, close to the coating, indicating that even if new phases didn't form, some atom diffusion occurred as well. Fig. 23 shows the microstructure of the fiber in the center and in the periphery and it can be stated that SiC crystallites didn't coarsen notably and no significant differences in mean grain size could be measured, only higher amount of amorphous phase could be seen in the center, Fig. 23a, as compared to the rim, Fig. 23b.

The composites ZBZ-H, ZBZ-T, ZBZ-iHS listed Table 3 were described in previous reports.^{1,28}

Figure 19: Examples of HR-TEM images of the matrix in ZBZ-iH* showing the interfaces between ZrB_2 - SiO_2 - ZrO_2 with EDS spectra of SiO_2 and ZrO_2 containing N traces.

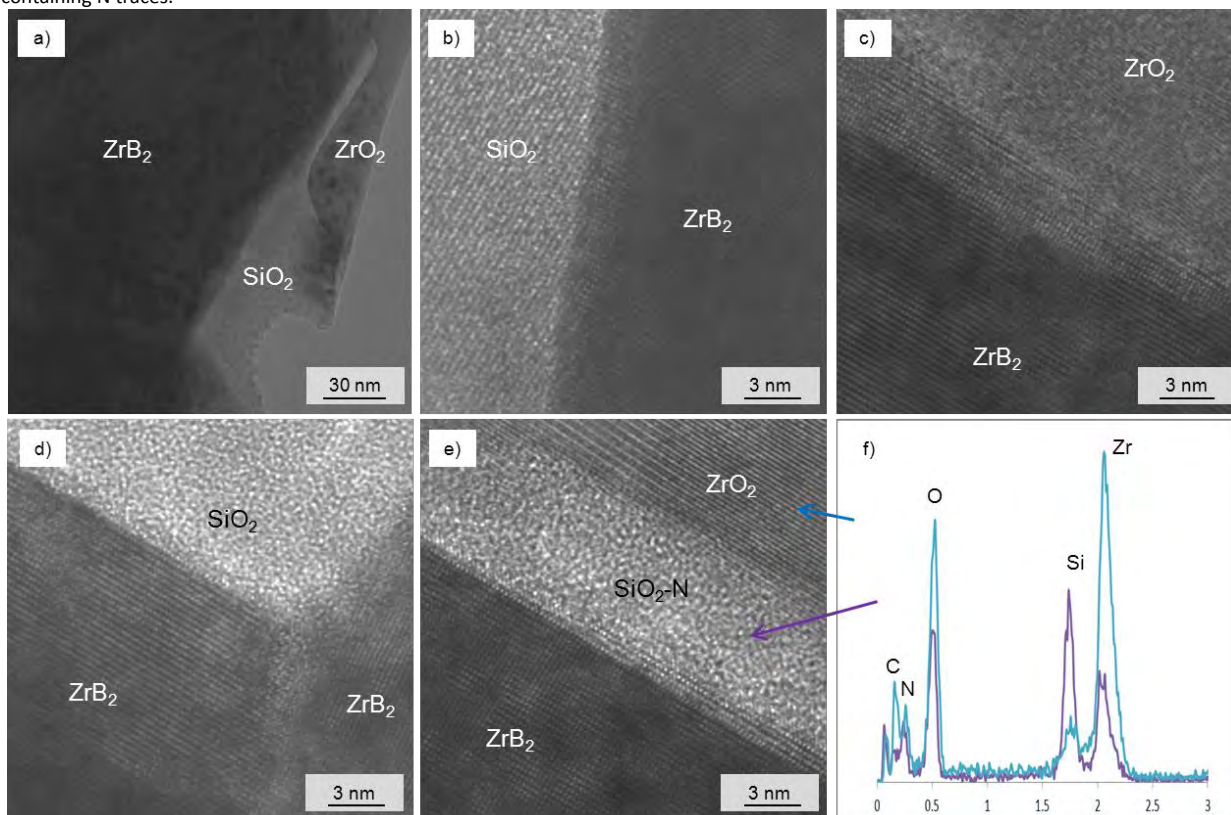


Figure 20: TEM images of fiber matrix interfaces in ZBZ-iH* at a) low and b) high magnification. c) Morphology of the coating with d) HR-image of BN with diffraction pattern and e) EDS spectra of the particles trapped within the coating.

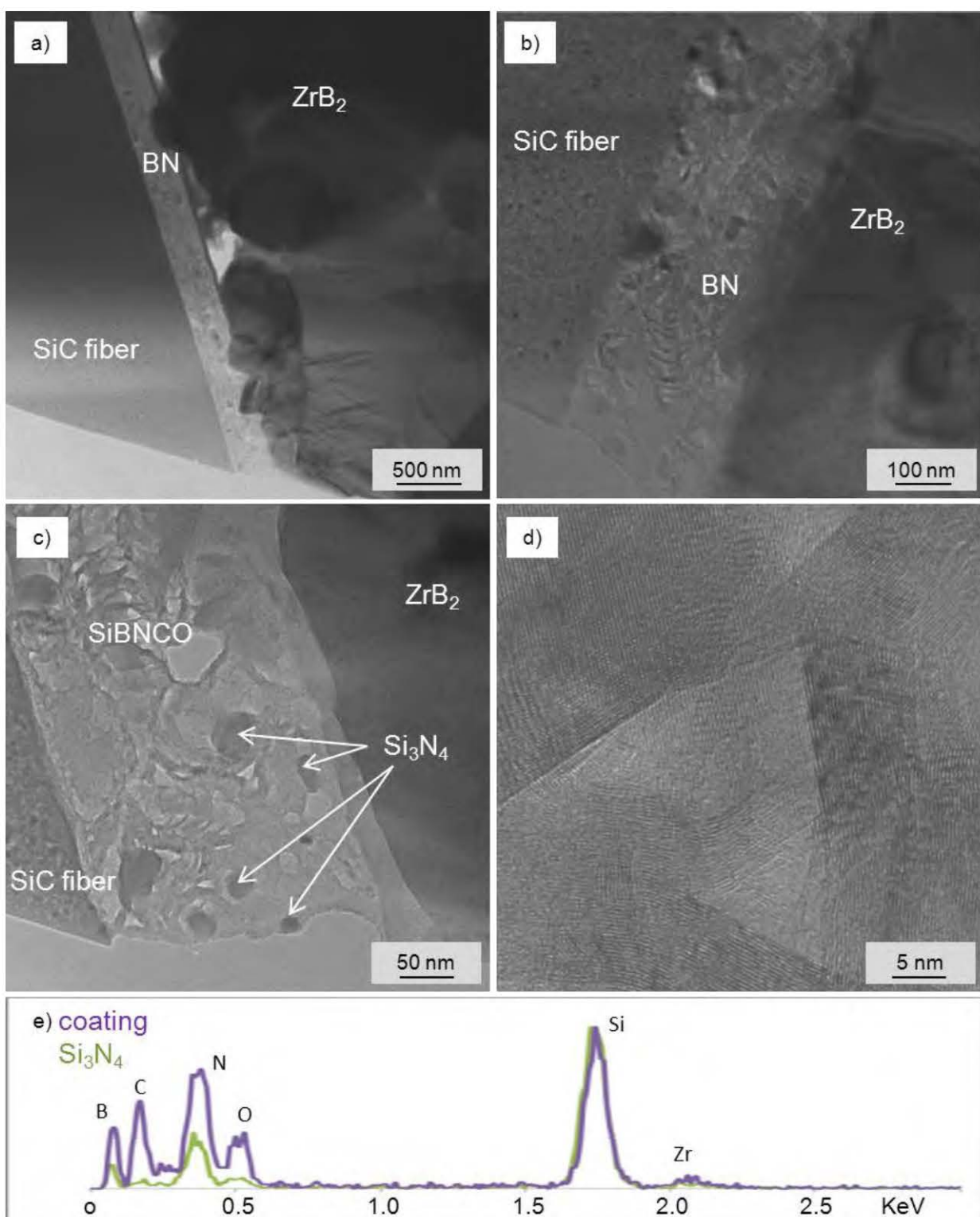


Figure 21: HR-TEM images of fiber-coating-matrix interfaces in ZBZ-iH*. a-c) coating-ZrB₂ interfaces and d-f) coating-fiber interfaces.

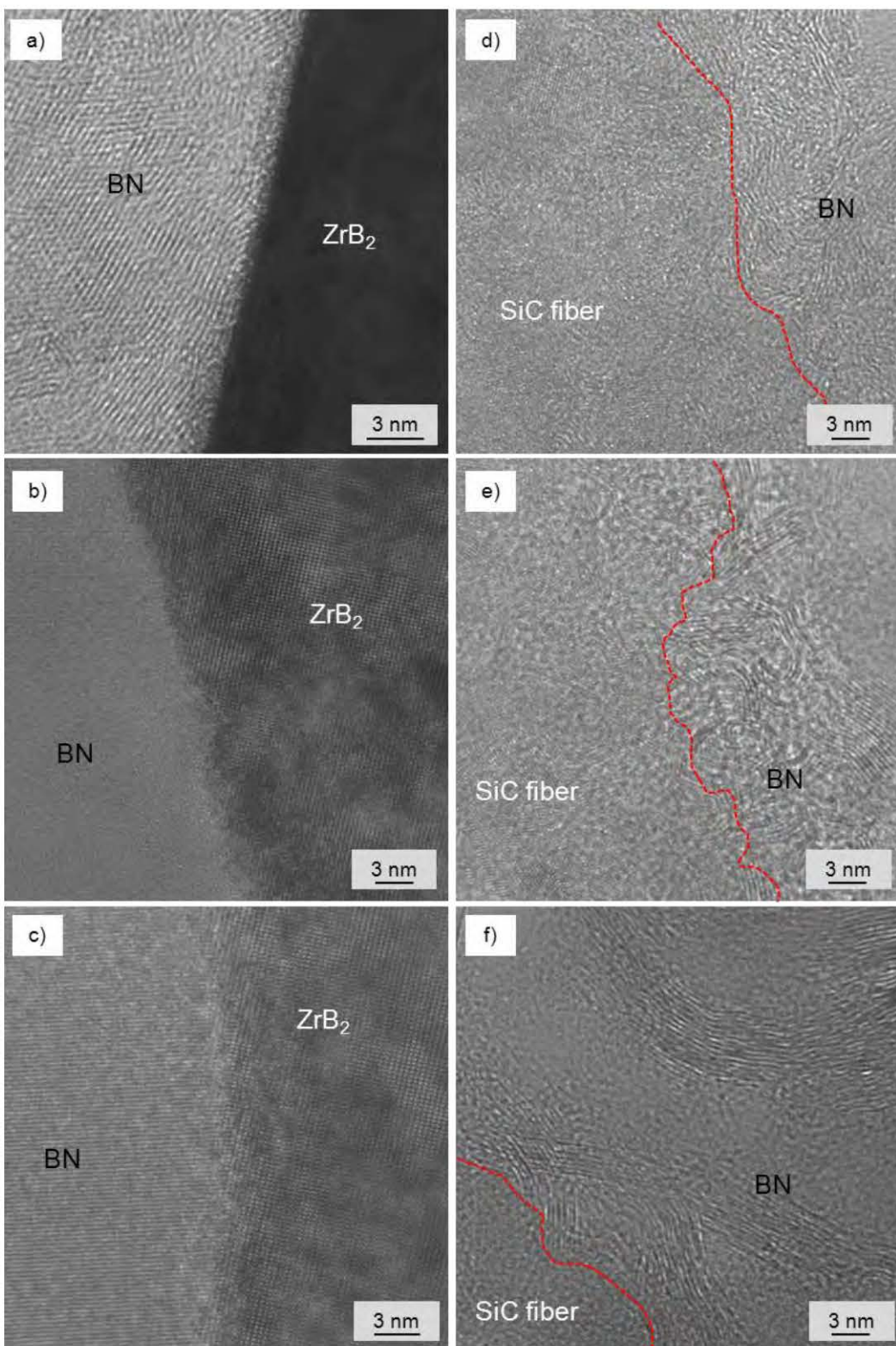


Figure 22: STEM image of a fiber edge in ZBZ-iH* with EDS elemental mapping.

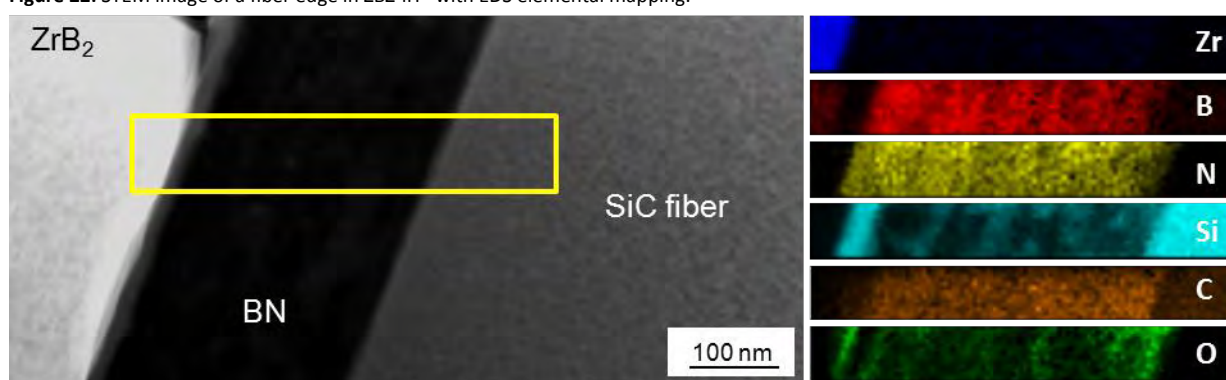
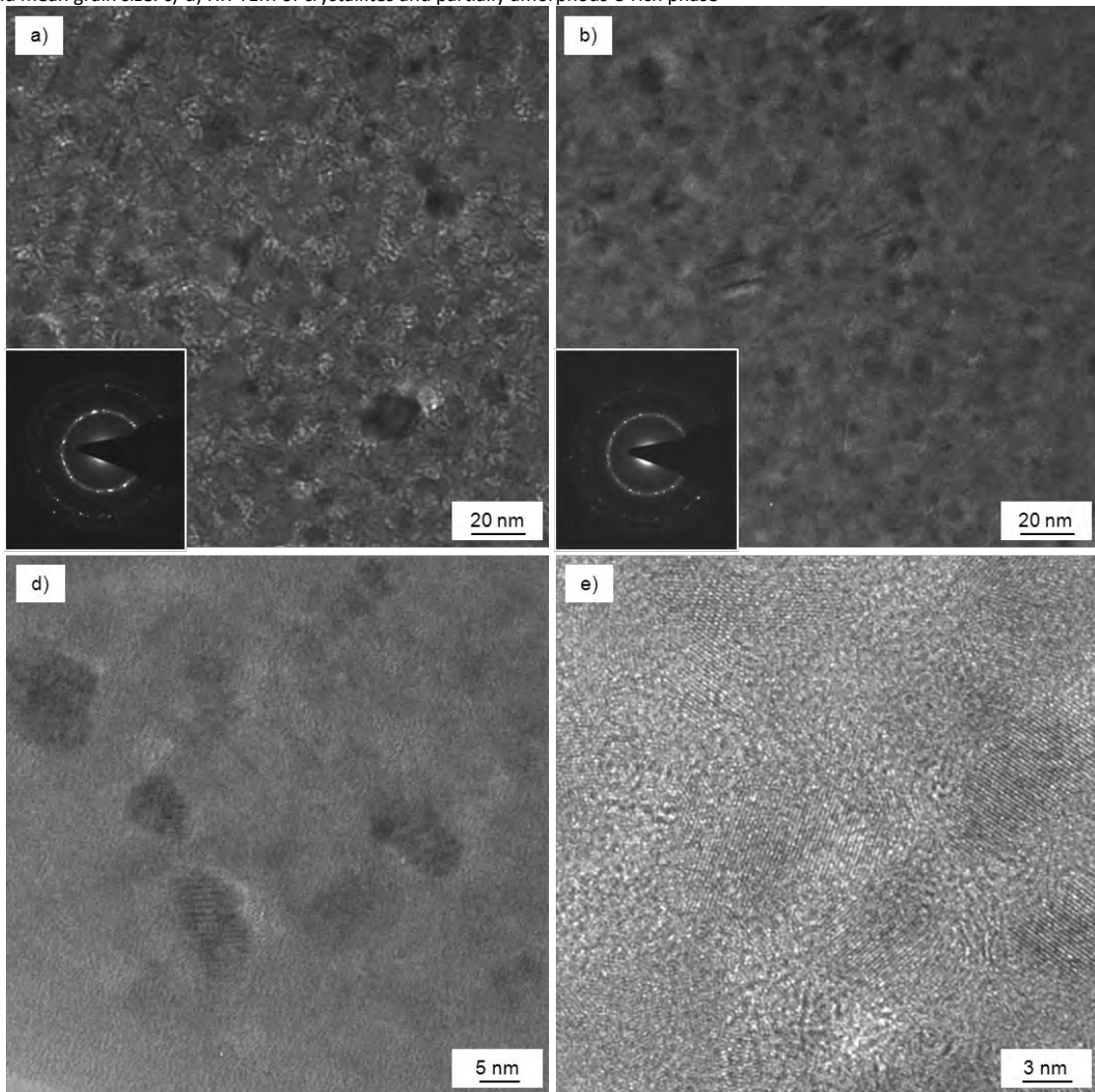


Figure 23: Morphology of a SiC fiber in ZBZ-iH* a) in the core and b) in the edge with corresponding diffraction patterns showing similar crystallinity degree and mean grain size. c)-d) HR-TEM of crystallites and partially amorphous C-rich phase



3.2.3. Mechanical properties

The mechanical properties for ZrB_2 ceramics with various kinds of chopped or long SiC fibers (Hi-Nicalon, Hi-Nicalon S, BN-coated Hi-Nicalon S, Tyranno SA3) studied in the present report or in previous works^{1,28} are reported in Table 3. All fracture toughness values vary from 4.5 to 6.2 $\text{MPa}\cdot\sqrt{\text{m}}$, whilst room temperature strength for chopped fiber goes from 390 to 535 MPa. A separate discussion is reserved for the 0/90°C long fiber composite.

Considering just the chopped fiber composites, what emerges immediately is that there is no obvious relationship between the quality of the fiber and an improvement of fracture or strength, that is more crystalline fibers with lower oxygen content (Tyranno SA3 or Hi-Nicalon S) do not necessarily lead to the highest toughness, in fact it seems that fiber with lower crystallinity level enables better toughening. Also the coating, although not continuous in material ZBZ-iHS²⁸ doesn't play an effective role in increasing the pullouts contribute.

As for the strength, slight fluctuations are due to the length of the fibers, which can undergo little variations depending on the milling media type and amount, time and speed.³⁰ At high temperature, the composites maintain the room temperature strength in all cases up to 1200°C, but at 1500°C an abrupt collapse prevents their use owing to the unavoidable oxidation of the fiber to liquid silica.³¹

3.2.4. Crossed comparisons among fiber-containing ZrB_2 -composites

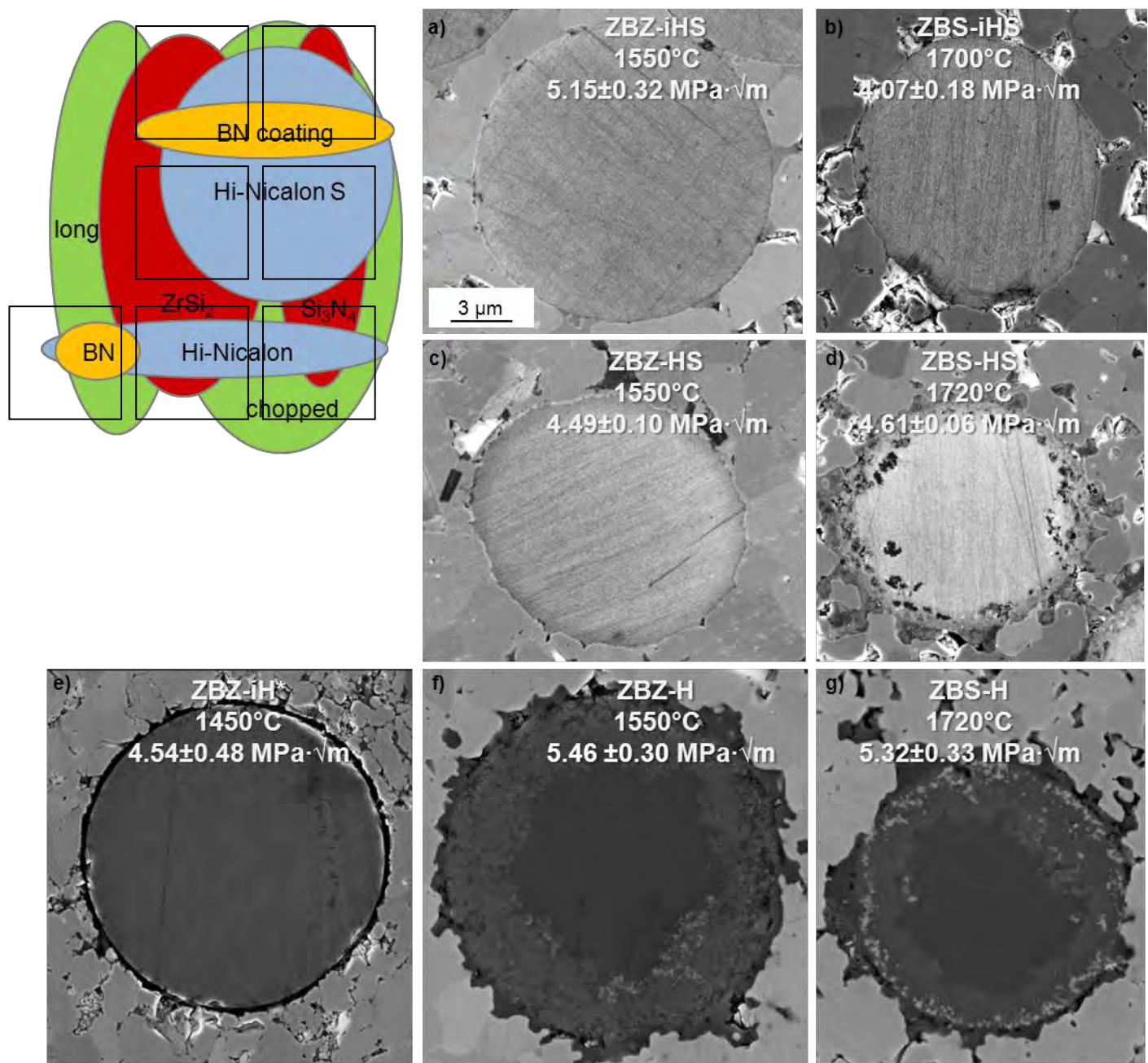
Sintering additive: Si_3N_4 vs ZrSi_2

It has been proved in previous studies^{1,28} that ZrSi_2 enables sintering of ZrB_2 at lower temperature as compared to Si_3N_4 , owing to the formation of liquid phases above 1400°C for the first, compared to 1590°C for the second. The liquid phase formed determines the maximum sintering temperature necessary to achieve full density, which in turn has notable effect on the evolution of the fiber morphology. Variation of crystallinity, formation of core-rim region, coarsening and coalescence of SiC crystals has been observed to be a continuous dynamic process and to be strongly dependent on the sintering temperature, in the case of Hi-Nicalon fiber,¹ but also for Tyranno SA3.²⁸ Comparing Fig. 24c and 24d, it is apparent that also for the refractory Hi-Nicalon S the same holds true: above 1700°C opening of the fiber occurs and reaction products remain trapped inside the fiber. Hi-Nicalon S fibers are reported to be the best technological product in terms of commercial SiC fibers, with respect to thermo-chemical properties and reliability.³² This general instability inside the ZrB_2 matrix confirms that at the state of the art, there are no real suitable SiC fibers for ultra-high temperature composites, given their non-equilibrium state with continuous evolution during exposure to high temperature and their detrimental effect on strength at 1500°C.

The use of one specific sintering additive has effects also on the chemistry of the secondary phases, in particular wetted grain boundaries are found when Si_3N_4 is employed. This has generally led to lower toughness,^{1,28} but in this case similar values are obtained for ZBS-HS and ZBZ-HS, 4.61 and 4.49 $\text{MPa}\cdot\sqrt{\text{m}}$ respectively. It is possible that higher

fiber modification, especially formation of porosity inside the fiber in ZBS-HS, Fig. 13, has weakened the generally strong fiber-matrix bond resulting in more fiber pullout.

Figure 24: Examples of fiber section in various ZrB_2 -based composites sintered with ZrSi_2 or Si_3N_4 as additive and containing Hi-Nicalon or Hi-Nicalon S, naked or BN-coated, long or short fiber, like indicated in the sketch on the left. For each composite, the sintering temperature and the fracture toughness are reported.



DATE	03/06/15
------	----------

Fiber crystallinity: Hi-Nicalon vs Hi-Nicalon S

Table 4 reports a comparative overview between the physical and thermo-mechanical properties of Hi-Nicalon and Hi-Nicalon S fiber. These two fiber types have similar diameter, 12-14 μm , both contain turbostratic carbon and the main difference is the crystallinity: the first type still contains a notable amount of amorphous Si-C-O phase and SiC crystals are in the order of 5-10 nm. For the second fiber type, the amount of partially amorphous Si-C is remarkably reduced together with the oxygen amount, and SiC crystallites are in the order of 20 nm. What follows these variances in microstructural features are significant differences in elastic constant, strength and thermal conductivity. In Fig. 24c,d,f,g a fiber section of composites containing the two fiber types are shown for two additives. For Hi-Nicalon, Fig. 24f-g, we always have development of irregular edges and the fiber assumes a core-shell-platelet morphology, the same happens for Hi-Nicalon S coupled with Si_3N_4 , Fig. 24d. For ZrSi_2 addition, the fiber maintains a rounded shape and the crystallites coarsen homogeneously throughout the fiber, Fig. 24c. Therefore it seems that even the more refractory fiber tends to lose its original shape and properties above 1700°C, similarly to what was observed for 2° generation fiber.¹ Higher microstructural stability was instead observed for Tyranno SA3 fiber.²⁸

Similarly to what previous studies suggested,³³ also in this case it seems that the combination of the same matrix with soft fibers (Hi-Nicalon), giving high $\text{Ematr}/\text{Efiber}$ ratio, results in composites with higher strength and toughness. Definitely, a high fiber Young's modulus promotes a high tensile thermal residual stress into the matrix. At the light of our findings, therefore, it seems that high ratio between the matrix and fiber Young's modulus must be preferred in order to have composite with high fracture performances, at least in composites with a matrix/fiber interface as strong as that observed in the composites at hand.

Table 4: Overview of thermo-mechanical properties of Hi-Nicalon and Hi-Nicalon S fibers.³⁴

Property	Hi-Nicalon	Hi-Nicalon S
Diameter, μm	14	12
Composition, wt%	62 Si, 32 C, 0.5 O	68.9 Si, 30.9 C, 0.2 O
Density, g/cm^3	2.74	3.10
β -SiC grain size, nm	5-10	20
Elastic Modulus, GPa	270	420
Strength, GPa	2.8	2.6
CTE, $10^{-6}/\text{K}$ (25-500°C)	3.5	-
K_{TH} , $\text{W}/\text{m}\cdot\text{K}$ (25-500°C)	7.77-10.1	18.4-16.3

Fiber coating: naked vs BN

The interposition of a weak interface between fiber and matrix, such as BN or pyrolytic carbon, is a common technological expedient used in CMC production to retard reactions between fiber and matrix during high thermal treatments and to trigger relevant toughening mechanisms, such as fiber pullout.^{35,36} However, deposition of a BN coating is a very expensive procedure and not all the coatings are suitable for these composites. Indeed preliminary

results performed on chopped BN-coated fibers in our labs revealed that amorphous BN coating tends to detach from the fiber during milling and crystallize during sintering, forming phases that weaken the whole microstructure.²⁸ As for pyrolytic carbon, again, preliminary results did not evidence any benefits over uncoated fibers.²⁸ Comparing the fiber sections in Fig. 24a-d it is clear that the coating, even if not continuous, retards the fiber degradation, especially above 1700°C, but the resulting fracture toughness doesn't increase with the least fiber damage.

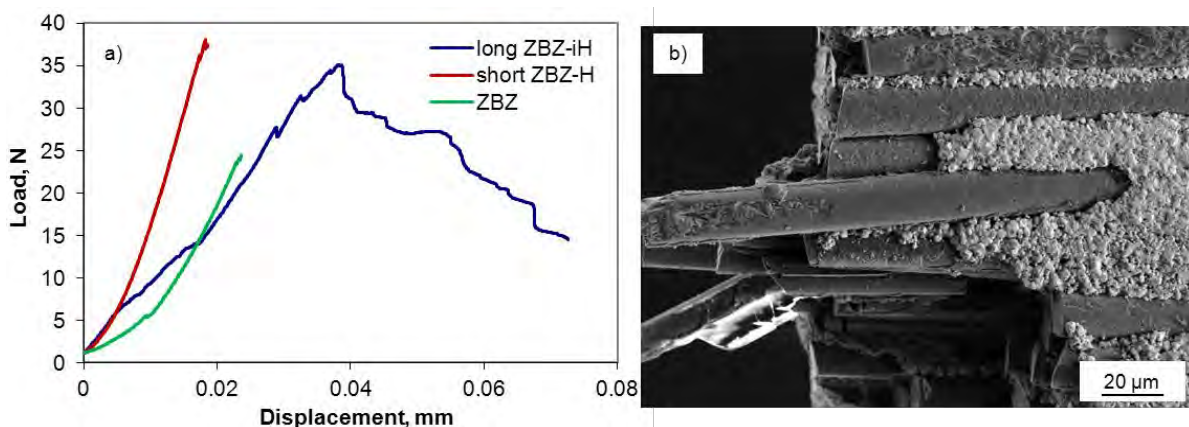
Also in the case where the fiber coating is smooth, continuous and with homogeneous thickness, Fig. 24e, and the fracture shows pullout, no significant toughness improvement is observed. Therefore, the use of naked partially amorphous SiC fibers, seems at present the most preferable solution to achieve a fracture toughness between 5-6 MPa·Vm and a reliable strength with very narrow standard deviation around 400 MPa up to 1200°C.

Fiber length: short vs long

Although data on long fiber-ZrB₂ composites are still very scanty, the experiments at hand didn't manifest the superiority of long-fiber composite over short-fiber ones. Examples of load-displacement curves during CN tests of unreinforced, long- and short fiber-reinforced composite are displayed in Fig. 25a and evidence the typical feature of the good CN behavior: the pop-in, the slow crack growth of the advancing crack and then the catastrophic failure.

In the case of long fiber composite, we clearly see a highly non brittle failure: the curve shows a nonlinear slope, achieves a maximum and then a reduction of the applicable load follows, which reflects the stable character of the final crack growth up to final fracture of the composite. The profile of the broken bar is shown in Fig. 25b where fiber pullout is evident. Although the higher amount of fiber, 25 vol%, the goodness and efficiency of the coating in protecting the fiber and promoting relevant toughening mechanisms, the obtained fracture toughness value is in the same range of short-fiber composites, but a more failure-tolerant behavior is achieved.

Figure 25: a) Load-displacement curves recording during CNB tests of unreinforced, chopped- or long-fiber reinforced ZrB₂ composites and b) fiber pullout in ZBZ-iH* after flexural test.



3.2.5. Conclusions on ZrB₂ + fibers

DATE	03/06/15
------	----------

A new series of ZrB_2 ceramics containing short or long, BN-coated or naked SiC fibers have been produced and characterized. The use of 3rd generation SiC fiber, Hi-Nicalon S, proved the non-equilibrium state of these fibers in ZrB_2 matrices. Similarly to previous generation fibers, they tend to strongly interact with sintering additive and undergo notable microstructural modification, especially above 1700°C. TEM analyses evidenced the microstructure at nanoscale level inside the fiber and revealed the chemistry and nature of the trapped particles.

The application of a BN coating for processing of long fibers resulted effective in blocking any reaction and structural modification of Hi-Nicalon fiber. The use of BN-coated long fiber instead of short naked fiber didn't prove significant improvement in fracture toughness of ZrB_2 , but resulted in a more damage tolerant composite.

TaC-based ceramics

The carbides of the group IV-VI transition metals have extremely high melting points (3000-4000°C) and are commonly referred to as "ultra-refractory carbides". Beside their stability at high temperatures, these compounds possess extremely high hardness, thus finding industrial use in cutting tools and wear-resistant parts.³⁷ In particular tantalum carbide (TaC) is an emerging material for use in the propulsion sector, where thermal solicitations are active, but the environment is reducing, so the pesting oxidation featuring the carbides is not the main issue.³⁸ On the contrary, thermal shock resistance and low damage tolerance are two impelling problems. In this respect, this work is focussed on methods for improving the fracture toughness of TaC-based composites. TaC is known to have a more metallic nature, compared to the other covalent compounds like Zr- and Hf-borides, thanks to the d-shell containing one electron more³⁹ and this generally results in less brittle materials. As most of refractory ceramics, TaC can achieve high strength values, up to 900 MPa,¹⁶ but still too moderate toughness to allow a safe use in various application fields.

In this work, different approaches were explored, mainly through addition of reinforcing phases as suggested by previous works: metal disilicide particles with suitable thermo-elastic properties,¹⁶ SiC particles,⁴⁰ SiC platelets,⁴¹ SiC fibers^{1,28} and C fibers.²⁸ Results are compared to unreinforced matrices, with and without sintering aids.

Transition metal disilicides ($MeSi_2$) were added to ZrB_2 and carbides mainly with the purpose of densification.^{16,17} They cannot be considered as solely sintering aids because they significantly modify the microstructure and properties especially when their content is raised over some 5 vol%. SiC addition to TaC was tested by Liu et al., who reported fracture toughness overpassing 6 MPa·m^{1/2} for addition of 20 vol% SiC particles.⁴⁰ As for platelets, one possible approach to introduce this kind of reinforcement is to exploit the $\beta \rightarrow \alpha$ SiC polytypic transformation enabling to pass from rounded particles to platelets, as previously experimented for ZrB_2 -composites.⁴¹ Addition of chopped fibers gave promising results in the case of borides.^{1,28}

When fiber or platelets were added, the sintering additive had to be accurately selected. $TaSi_2$ was used to decrease the densification temperature of TaC^{16,17} and inhibit SiC fiber damages.^{1,28} However this additive, and

silicides in general, cannot be used in combination with C fiber owing to an excessive reaction leading to the fiber degeneration into SiC agglomerates, therefore Si_3N_4 was employed. Lastly, MoSi_2 was used to promote transient liquid phase sintering of TaC matrix and enable $\beta \rightarrow \alpha$ SiC transformation without leaving glassy amorphous phase.⁴¹ Also in this case TaSi_2 could not be used owing to its volatility in reducing environment at high temperatures and low pressure.^{16,17}

The purpose of this study is hence to explore the addition of suitable secondary phases able to trigger efficient toughening mechanisms. Specifically, the effect of the introduction of secondary phases in form of particle, platelet or fiber to TaC matrix will be discussed in relationship to the microstructure evolution and the resulting mechanical properties.

Figure 26: SEM image of reinforcing phases: a) SiC particles, b) Hi-Nicalon, c) Tyranno SA3, d) C fiber.

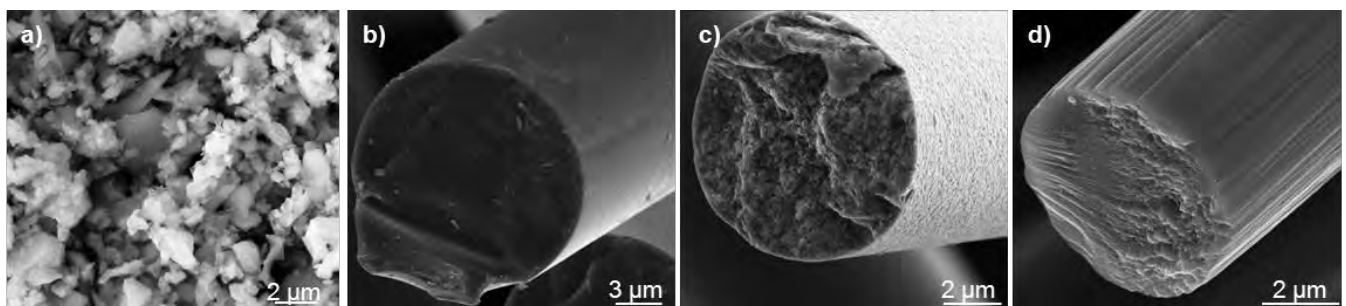


Table 5: Label, composition, sintering parameters, density, mean grain size (m.g.s.) and size of the reinforcing phases before and after sintering. HP: hot pressing, PS: pressureless sintering, AR: aspect ratio.

Label	Sint. add. (vol%)	Reinforce (vol%)	Reinforce size (μm)	Sintering (°C, MPa, min)	Rel. density (%)	TaC m.g.s. (μm)	Reinforce after sintering (vol%)	Reinforce size after sintering (μm)
T	-	-	-	HP:1900,30,15	94.0	4.0±0.8	-	-
TS	5 Si_3N_4	-	-	HP:1850,30,10	96.5	2.5±0.6	5 SiC	1.0
TS-S	5 Si_3N_4	15 β -SiC	0.6	HP:1850,50,10	97.5	1.2±0.4	20 SiC	1.5
TT	-	15 TaSi_2	2.0	HP:1750,30,10	97.1	2.5±0.5	10 TaSi_2	3-8
TM-S	5 MoSi_2	15 β -SiC	0.6	PS:2100,-,180,Ar	96.5	7.8±2.8	15 SiC_{pl}	AR: 1.8
TT-HN	10 TaSi_2	20 SiC Hi-Nicalon	\varnothing : 15, l=500	HP:1750,30,8	98.1	2.5±0.7	15 SiC Hi-Nicalon + 5 SiC_{pl}	\varnothing : 7.0, l: 80, AR: 2.5
TT-T	10 TaSi_2	15 SiC Tyranno SA3	\varnothing : 7.5, l=200	HP:1700,40,9	97.9	2.4±0.7	15 SiC Tyranno SA3	\varnothing : 7.5, l: 200
TS-C	5 Si_3N_4	20 Cfiber	\varnothing : 7.0, l=200	HP:1900,50,12	97.8	0.6±0.2	15 Cfiber + 5 SiC	\varnothing : 6.2, l: 200, 1.5

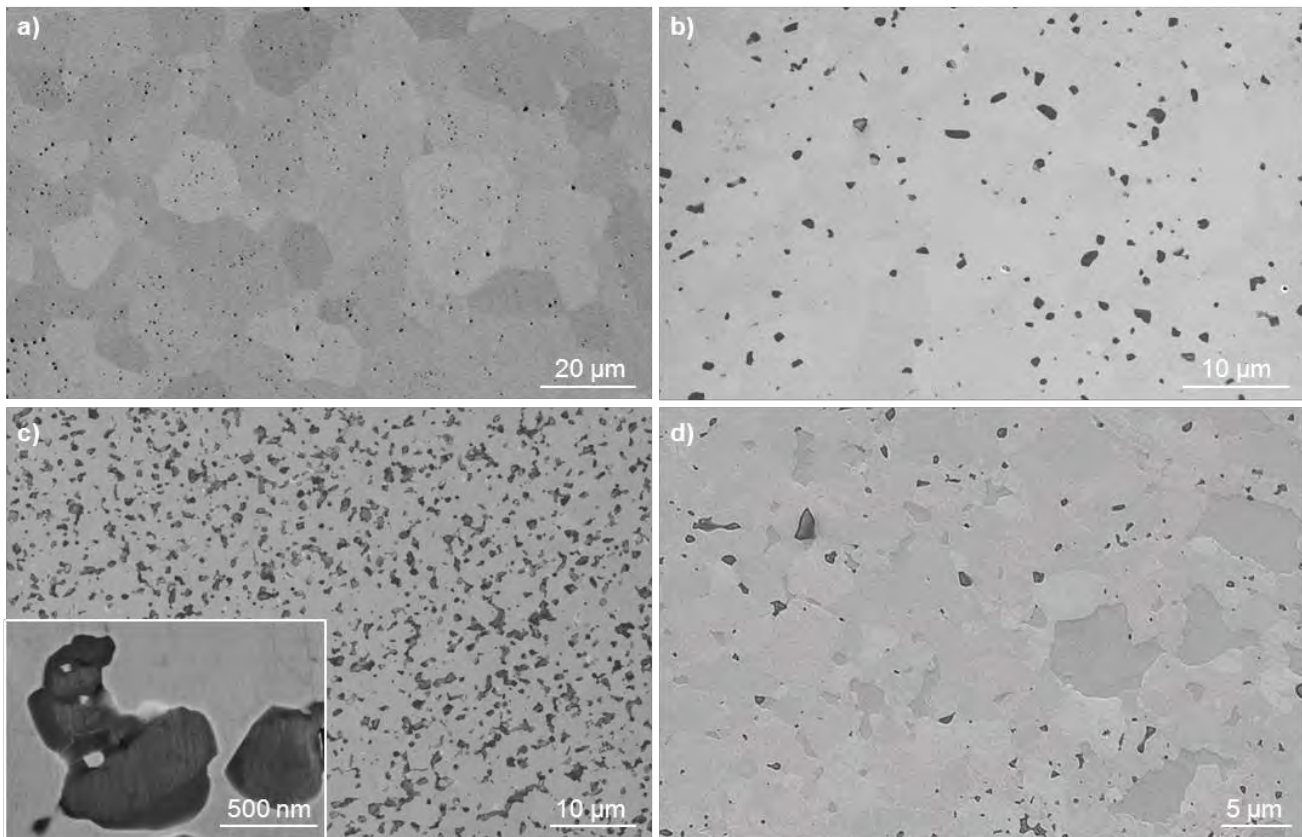
3.3. TaC baselines

An additive free pure TaC ceramic was prepared as reference value (T). As expected, TaC was 94% dense after sintering at 1900°C for 15 minutes. The microstructure was spatially uniform and consisted of faceted equiaxed grains with mean grain dimensions in the range of 5-7 μm (Fig. 27a). Occasionally, oxide phases were detected along the

DATE	03/06/15
------	----------

grain boundaries by SEM/EDS analysis and residual porosity ~5 vol % was confirmed. In order to enable complete densification, 5 vol% Si_3N_4 was added to TaC (Fig. 27b). The sintering temperature for this composite (TS) was 1850°C held for 10 minutes. The ceramic resulted fully dense with rounded grain size of about 2.5 μm and around 3 vol% SiC particles in place of Si_3N_4 , owing to its dissociation in the hot pressing chamber.

Figure 27: SEM images of a) pure TaC (T), b) TaC+ Si_3N_4 (TS), c) TaC+ Si_3N_4 +SiC particles (TS-S), d) TaC+ TaSi_2 (TT).



3.4. Reinforced TaC-composites

3.4.1. TaC + SiC particle

Despite the addition of Si_3N_4 as sintering additive, this ceramic required 1850°C to achieve full density. A picture of the polished section is shown in Fig. 27c. The sintering additive was difficult to detect in the final microstructure, as it reacted with the carbide to form additional SiC phase, giving a final total amount of SiC around 20 vol%. Agglomeration of SiC particles was frequent, but the size of these agglomerates was around 1.5-2.0 μm , i.e. in the order of TaC mean grain size, Table 5.

3.4.2. TaC + TaSi₂

This composite, was densified at 1750°C and SEM observation confirmed a pore-free microstructure (Fig. 27d). TaC had mean grain size around 2.5 µm with larger grains, up to 6-7 µm. TaSi₂ grains tended to form large pockets as wide as 3-8 µm. Other spurious phases formed upon decomposition of the additive, were identified as SiC, Si-C-O and SiO₂ and Ta_xSi_yC_z.^{16,17}

3.4.3. TaC + SiC platelet

Pressureless sintering of TaC-MoSi₂ system generally requires a temperature around 1950°C,⁴² but in this case it was set at 2100°C for 3 hours in order to let the $\beta \rightarrow \alpha$ SiC polytypic transformation to completely occur. The pellet resulted almost fully dense, around 97%, but the mean grain size of TaC was notably coarsened, around 7 µm, with grains up to 16 µm. SiC showed the typical elongated shape of hexagonal α -polytype and the platelets were homogeneously distributed in the matrix, Fig. 28a. SiC platelet pullout often occurred during polishing procedure, Fig. 28b. Residual MoSi₂ phase was found in amount below 3 vol%, in its typical appearance, grey contrast and low dihedral angles, Fig. 28c. TEM analysis confirmed that SiC platelets were often flanked by triangular secondary phases containing Co traces, owing to powder impurities, or based on TaSi₂, owing to mutual cation exchange between matrix and sintering additive, or based on silicon, owing to the high sintering temperature favorable to silicides dissociation, Fig. 29. SiC particles displayed a core-shell structure, typical of Ostwald-Ripening grain growth and coalescence, with the core composed by SiC separated through a defective structure by the rim composed of SiC with oxygen traces, as confirmed by EDS spectra in Fig. 30. SiC-SiC and TaC-SiC interfaces were however found to be non-wetted (Fig. 31 and Fig. 32, respectively), as previously found for similar systems containing SiC and MoSi₂.⁴¹

Figure 28: SEM images of polished section of TM-S showing a) platelets distribution, b) platelets pullout occurred during polishing and c) magnification of a platelet with Co and Si phases at the triple junctions.

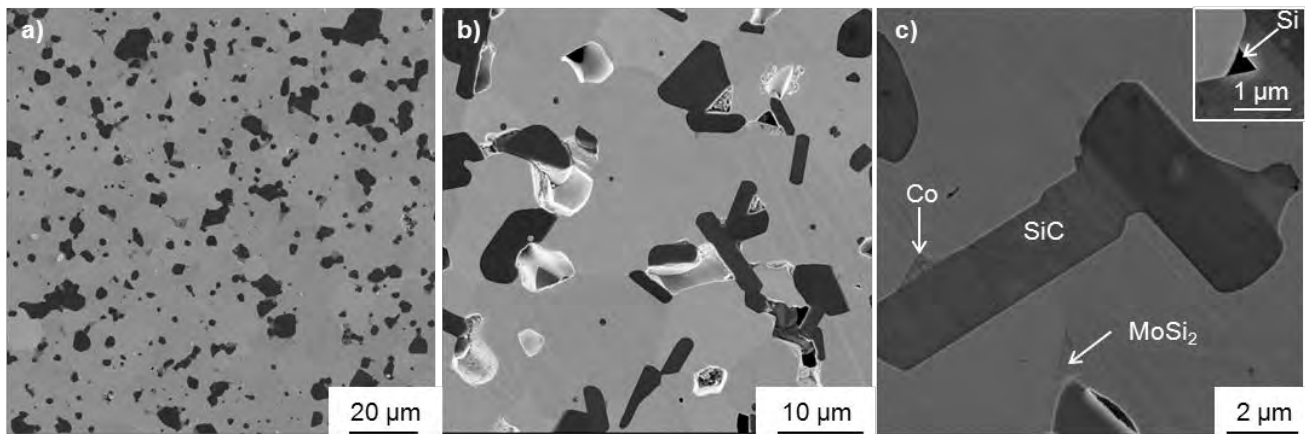


Figure 29: TEM images of TM-S showing adjacent SiC platelets and secondary phases at the triple junctions.

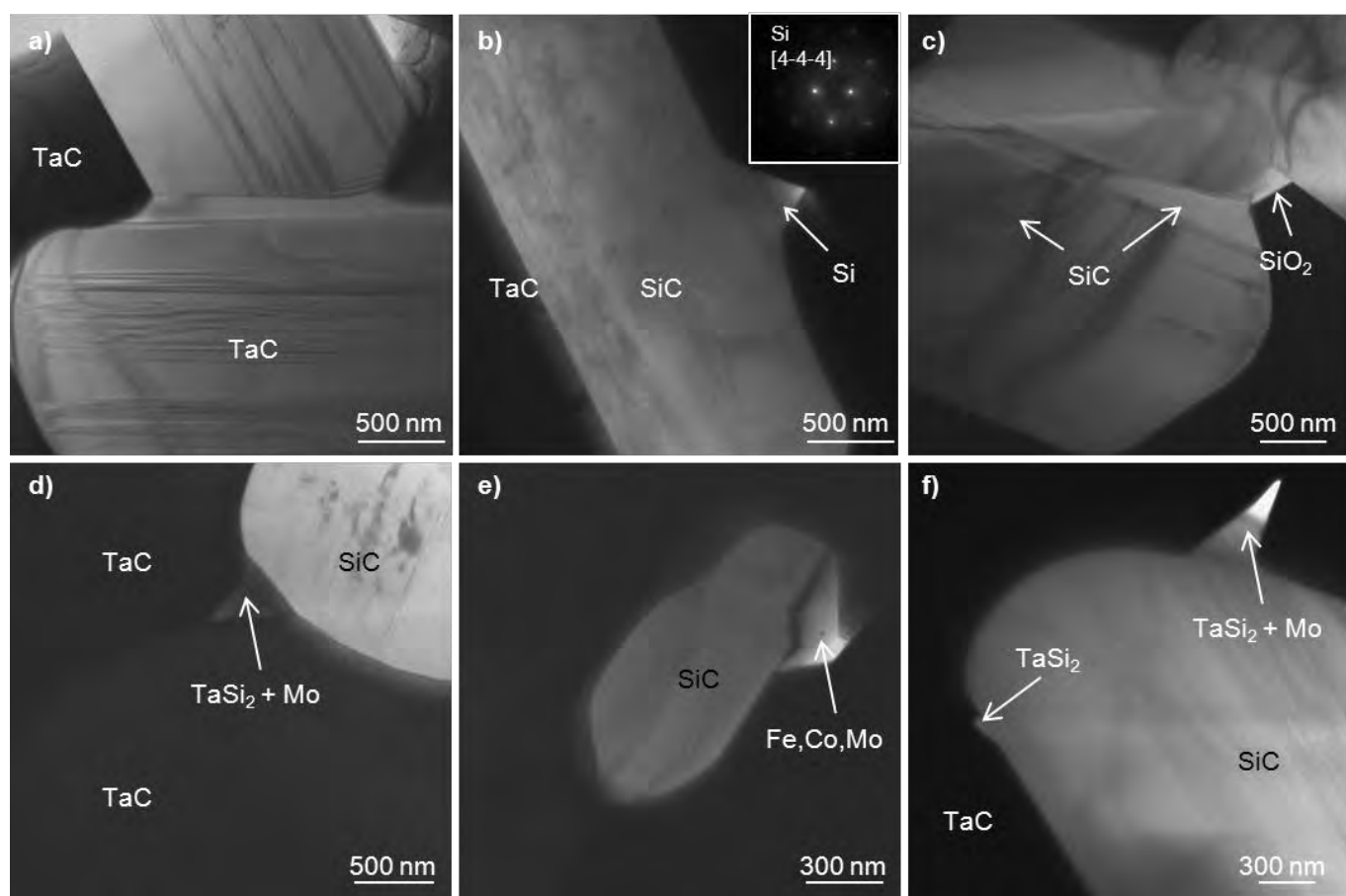


Figure 30: Examples of a),b) SiC platelets with corresponding EDS spectra in c) showing the core-rim morphology and chemistry.

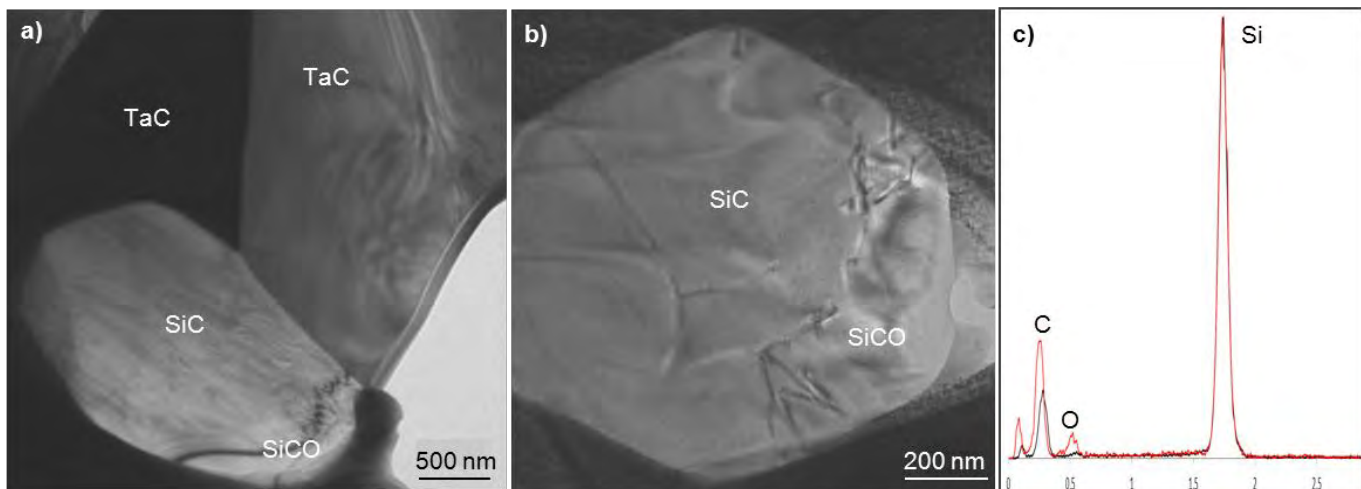


Figure 31: a) TEM and b) HR-TEM images of adjacent SiC platelets with EDS spectra and diffraction pattern in the insets.

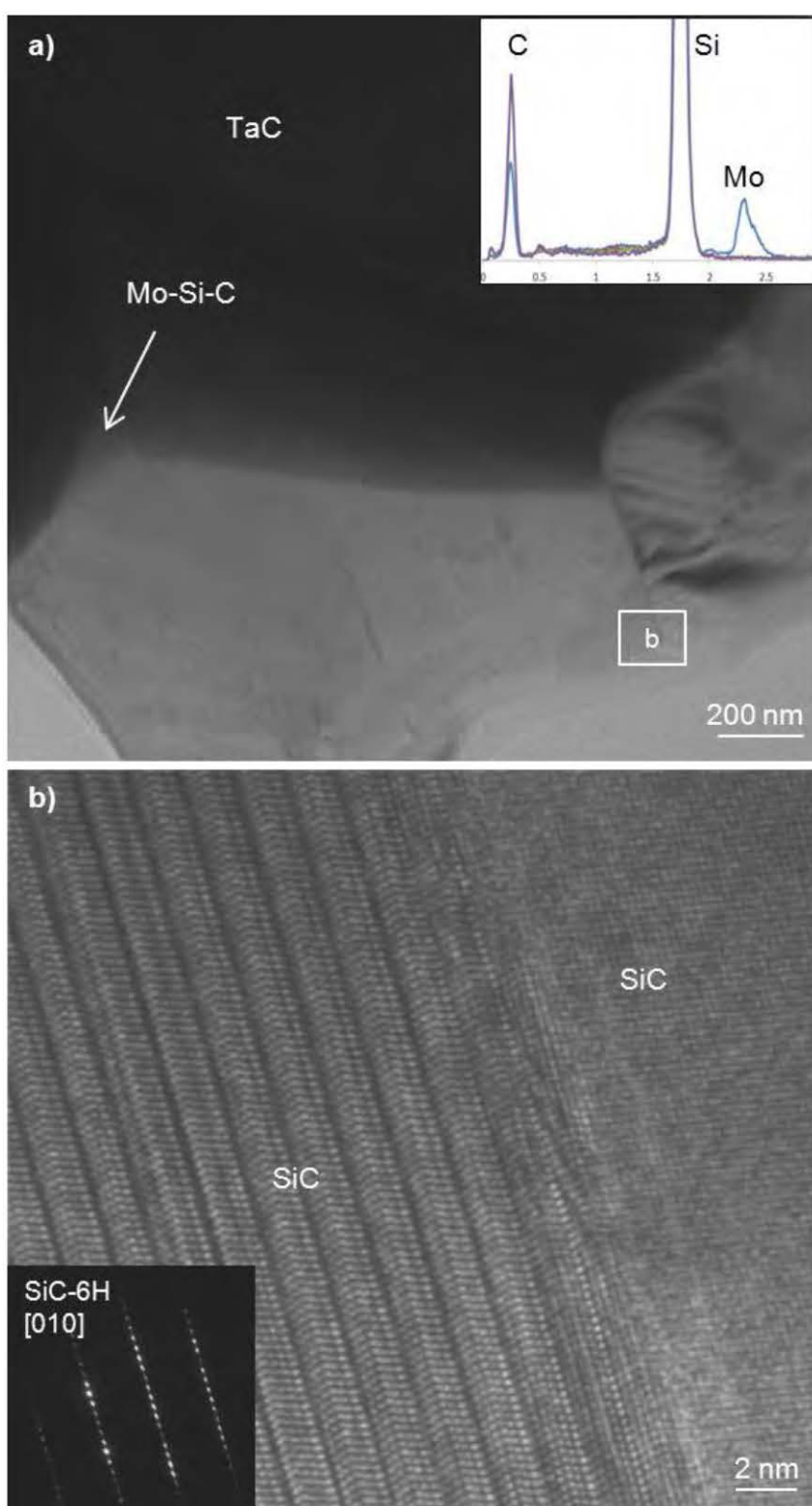
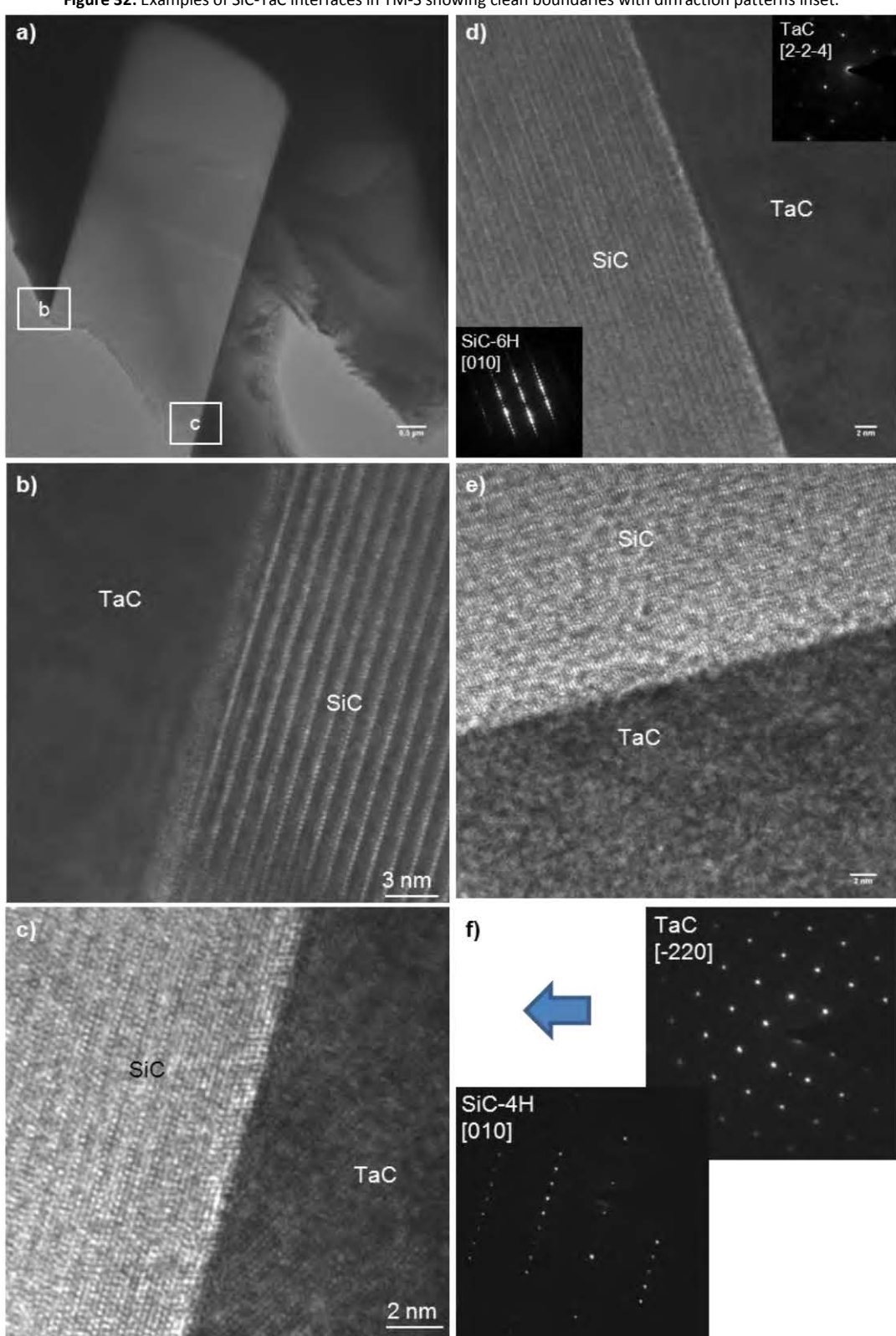


Figure 32: Examples of SiC-TaC interfaces in TM-S showing clean boundaries with diffraction patterns inset.



3.4.4. TaC + Hi-Nicalon fiber

The composites containing SiC Hi-Nicalon chopped fiber and sintered with 10 vol% TaSi₂ was fully densified at 1750°C. In the polished section in Fig. 33a it can be observed that no fiber agglomeration occurred and the fibers were distributed almost isotropically in the section plane perpendicular to the hot pressing direction, however their diameter was notably decreased, as the SiC core was around 7 µm compared to the initial diameter of 15 µm; the same occurred on the longitudinal direction, which was reduced to 50 µm-length from the 1 mm initial length, Fig. 33b,c. In the cross section of Fig. 33d, an inner SiC core with irregular edge can be recognized; moving outwards, TaC bright particles as small as 300 nm and coarsened SiC constitute a jagged rim. Beyond this layer, another 2 µm bright stratum of coarser TaC grains is found, in turn surrounded by coarse SiC platelets with squared shape and grain size around 2-4 µm. TEM images disclosed the fiber morphology in more details, Fig. 34-35: SiC crystallites in the core were up to 30 nm and immersed in partially amorphous phase and turbostratic carbon, Fig. 35. The interface between core and rim was separated by constellation of TaC particles, which tended to coalesce, Fig. 36a-b, and coarsened SiC grains, around 300 nm. Not far from the fiber, SiC platelets were found, standing adjacent SiO₂-based glass containing Ta traces, Fig. 36c-d.

Figure 33: SEM images of polished section of TT-H showing a) the overall microstructure, b) fiber deterioration and TaSi₂ aspect, c) a fiber section and d) the magnification fiber/matrix interface.

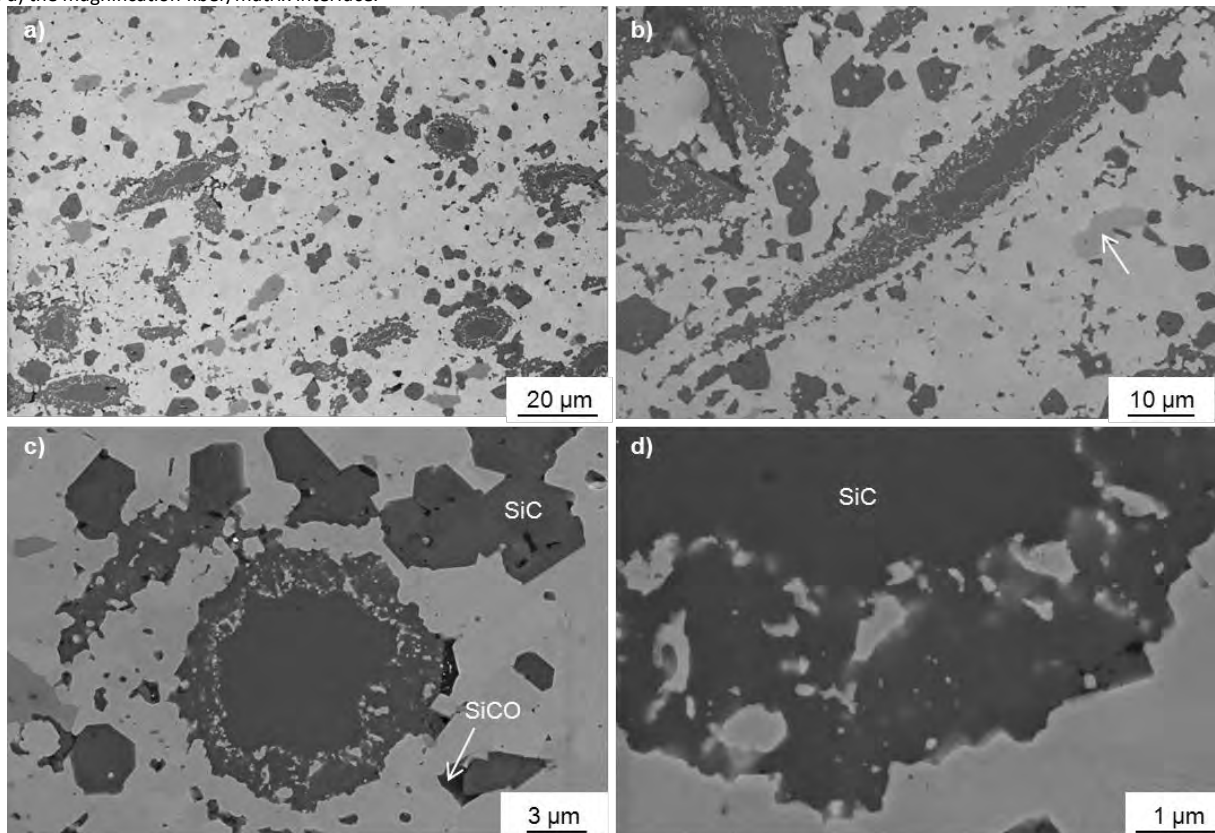


Figure 34: a) SEM image of a fiber section in TT-HN and b)-d) TEM images of a fiber at the interface with the matrix showing SiC coarsening and trapped dark TaC particles between core and rim.

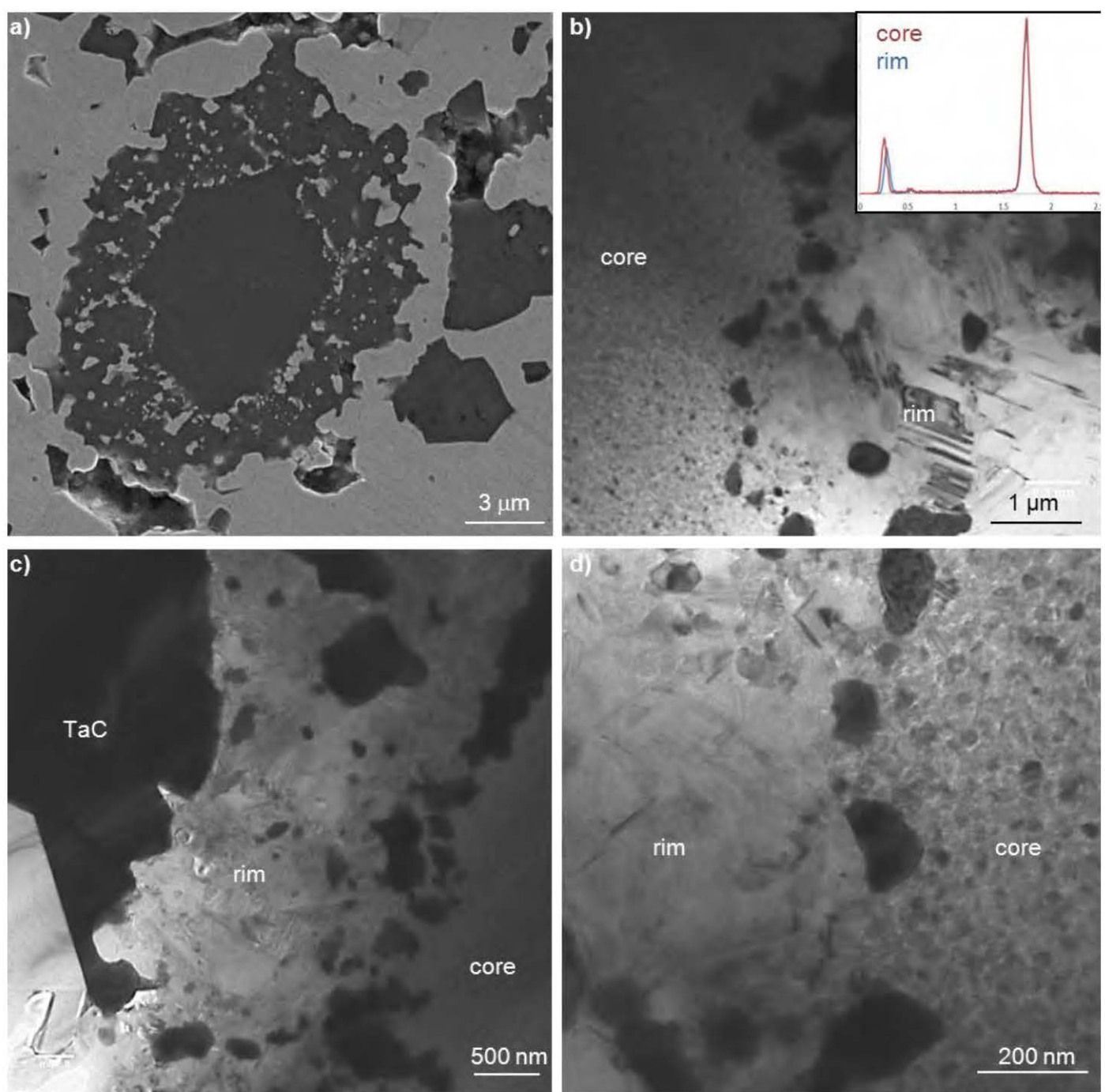


Figure 35: TEM images of fiber core with diffraction pattern showing the presence of amorphous phase and turbostratic carbon.

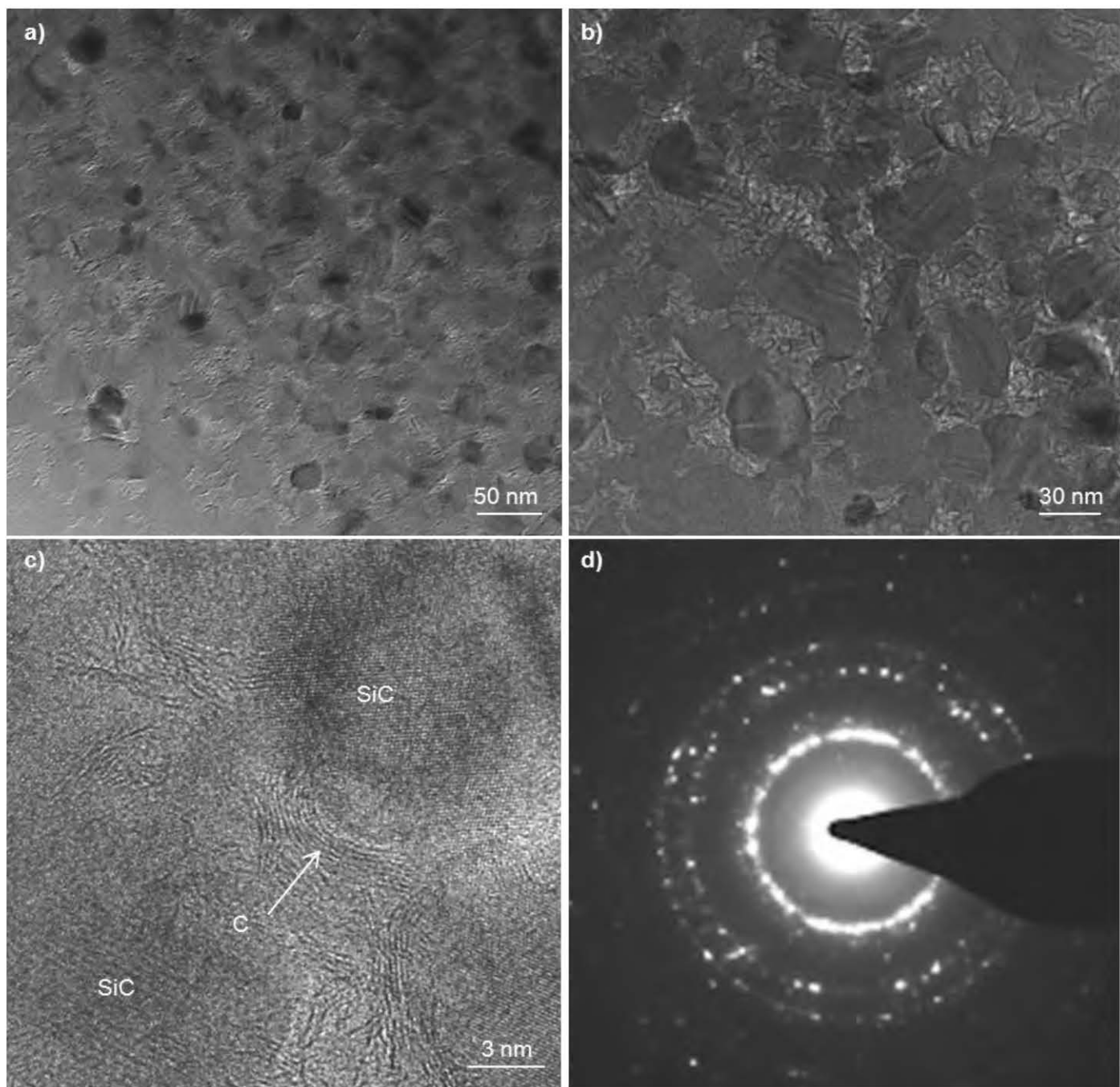
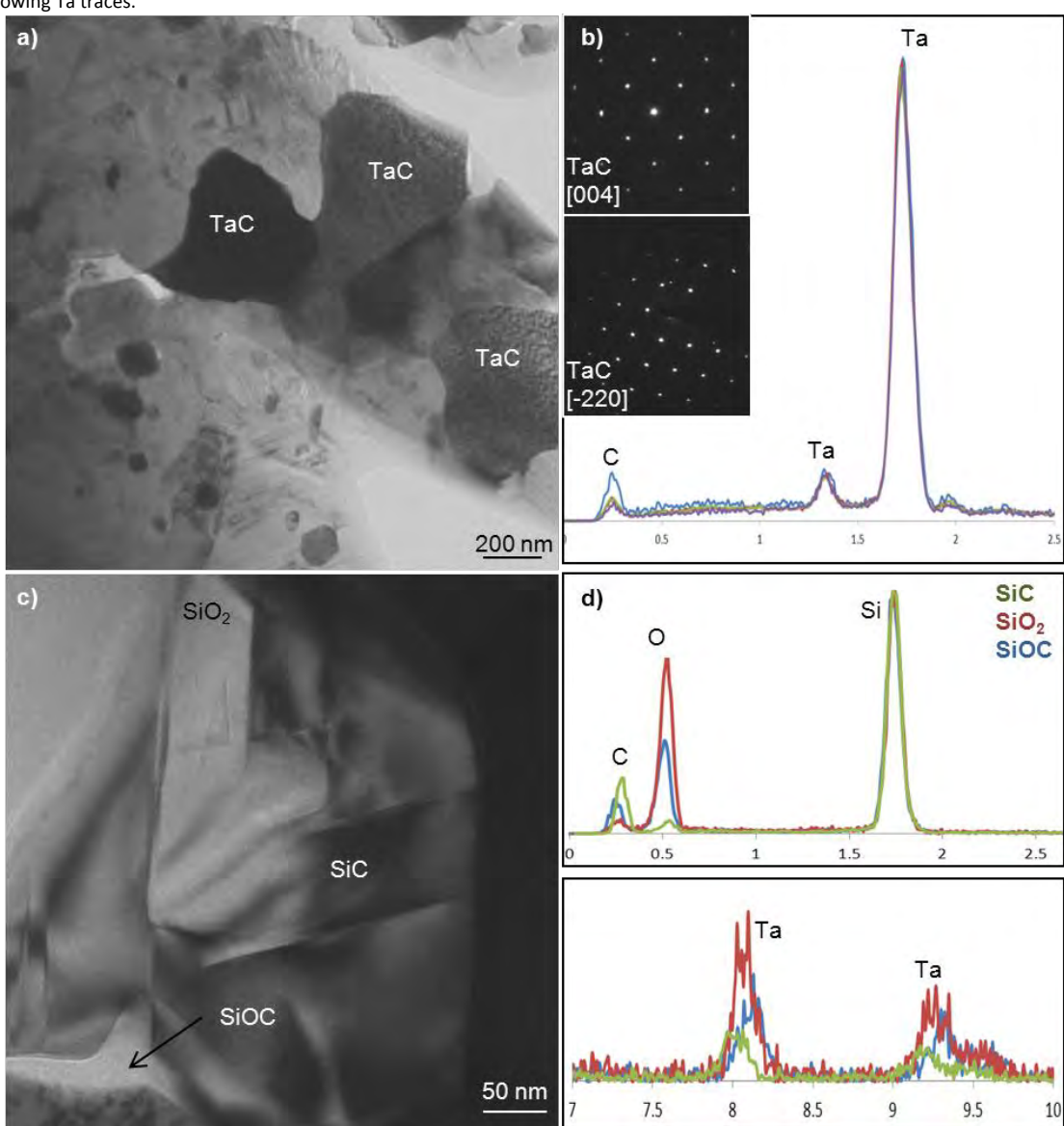


Figure 36: a) TEM image TaC particles at the core/rim interface with b) EDS and diffraction pattern, c) SiC platelets around the fiber with d) EDS spectra showing Ta traces.



3.4.5. TaC + Tyranno SA3 fiber

This composite was sintered at 1700°C with addition of TaSi₂ and reached a relative density of 97%. The fiber polished section is shown in Fig. 37: the matrix mean grain size is around 2 μm and porosity is almost absent. The fibers were well dispersed in the matrix and the maximum fiber length was 200 μm with fiber debris scattered throughout the matrix.

Large areas of TaSi₂, light gray phase with dimension 6-7 μm , were also observed in the matrix; occasionally these were intergranularly micro-cracked, Fig. 37d. Other secondary phases were SiC/Si-C-O and SiO₂ deriving both from the additive dissociation and from fiber. Indeed, the fiber/matrix adhesion was good, owing to silica-based zones at the

matrix/fiber interface, Fig. 37e. Fiber debris trapping metal impurities or oxides were also found, Fig. 37f. As for the reinforcement morphology, Tyranno fiber maintained an appearance closer to the pristine aspect, as compared to the Hi-Nicalon fiber. Coalescence of SiC crystallites took place in the rim, about 1.3 μm thick, leaving about 40% of the fiber with typical features of Tyranno SA3 fibers, i.e. dark carbon-rich phase among crystallites. TEM images of the central and outer regions of the fiber are shown in Fig. 38. The difference between SiC crystallites in the core and in the fiber periphery was minor, around 110 nm in the core and around 120 nm in the rim, but both coarsened as compared to the starting 70 nm, and also little differences in the amount of amorphous phase could be detected by electron diffraction. In the core, the space between the crystallites was filled by carbon-rich partially amorphous phase, Fig. 39a-c, whilst in the rim, mostly clean junctions were found among SiC, Fig. 39d-f. On the contrary, the fiber/matrix interface was often wetted by Si-C-O glass, Fig. 40.

Figure 37: SEM images of polished section of TT-T showing a) the fiber distribution, b) the overall microstructure, c) formation of SiC, d) TaSi_2 cracking, e) a fiber section and f) metal impurities trapped in fiber debris.

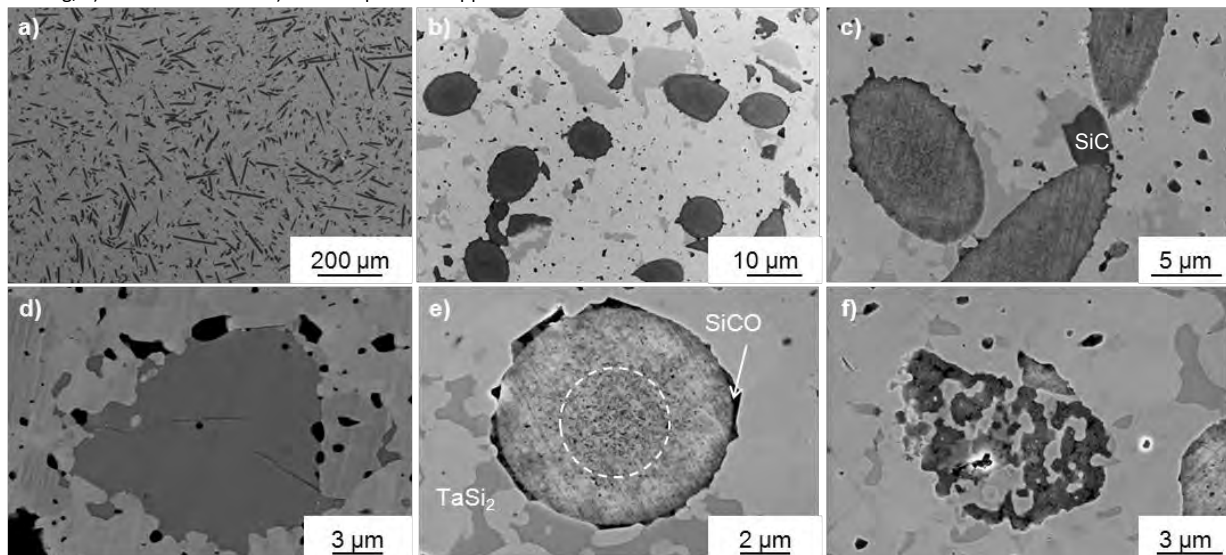
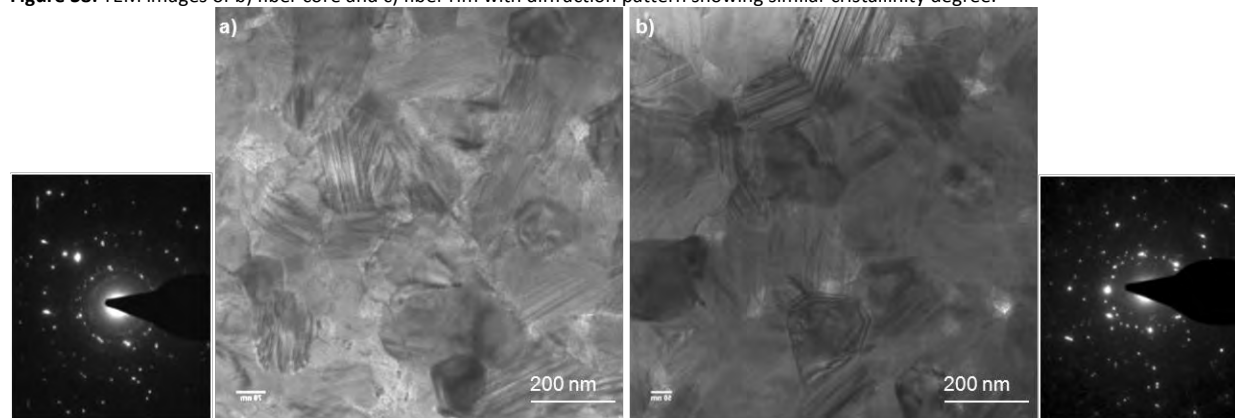


Figure 38: TEM images of b) fiber core and c) fiber rim with diffraction pattern showing similar crystallinity degree.



DATE	03/06/15
------	----------

Figure 39: a)-c) TEM images of the fiber core showing partially amorphous Si-C, and turbostratic carbon and d)-f) fiber rim showing clean grain boundaries.

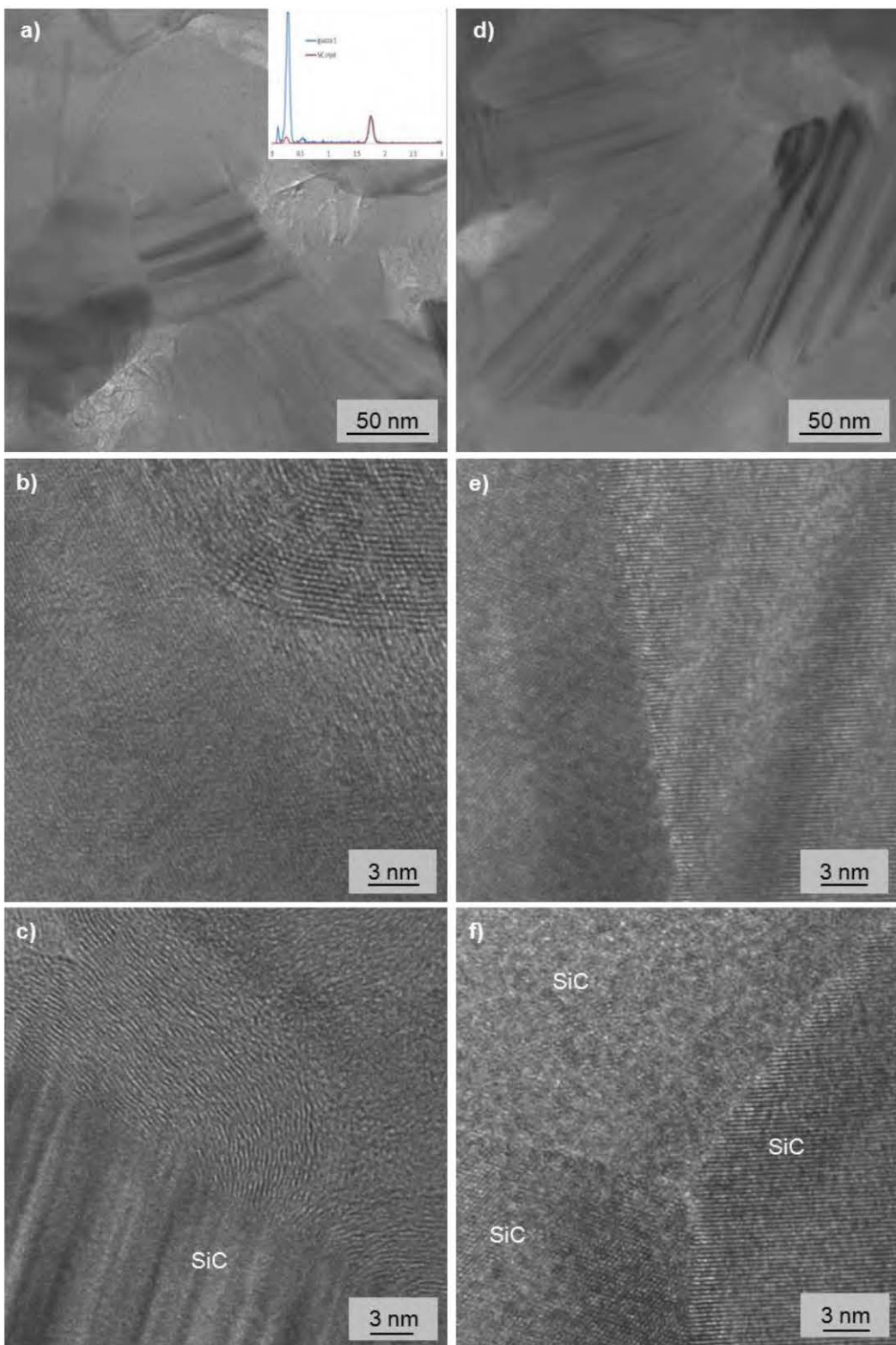
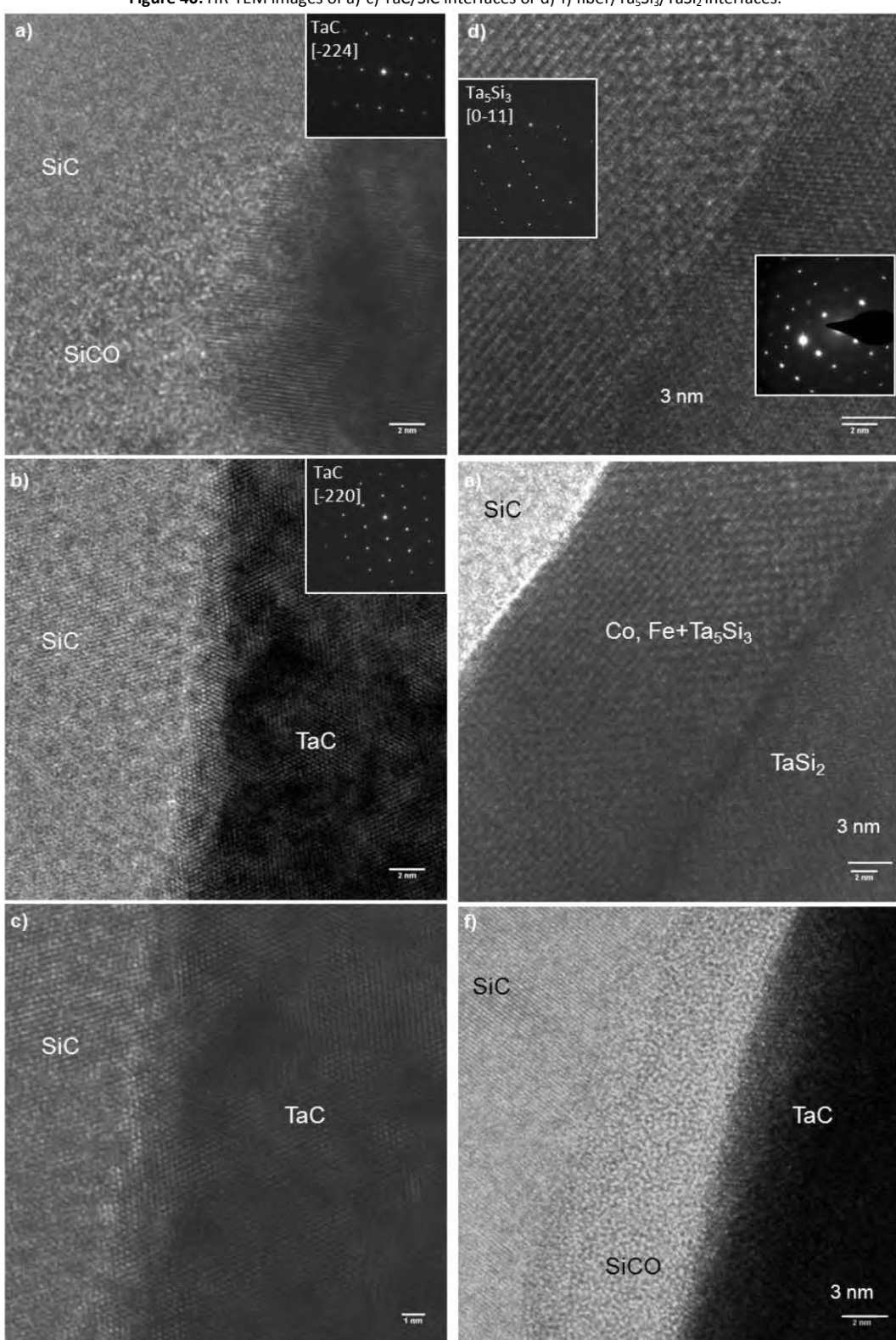


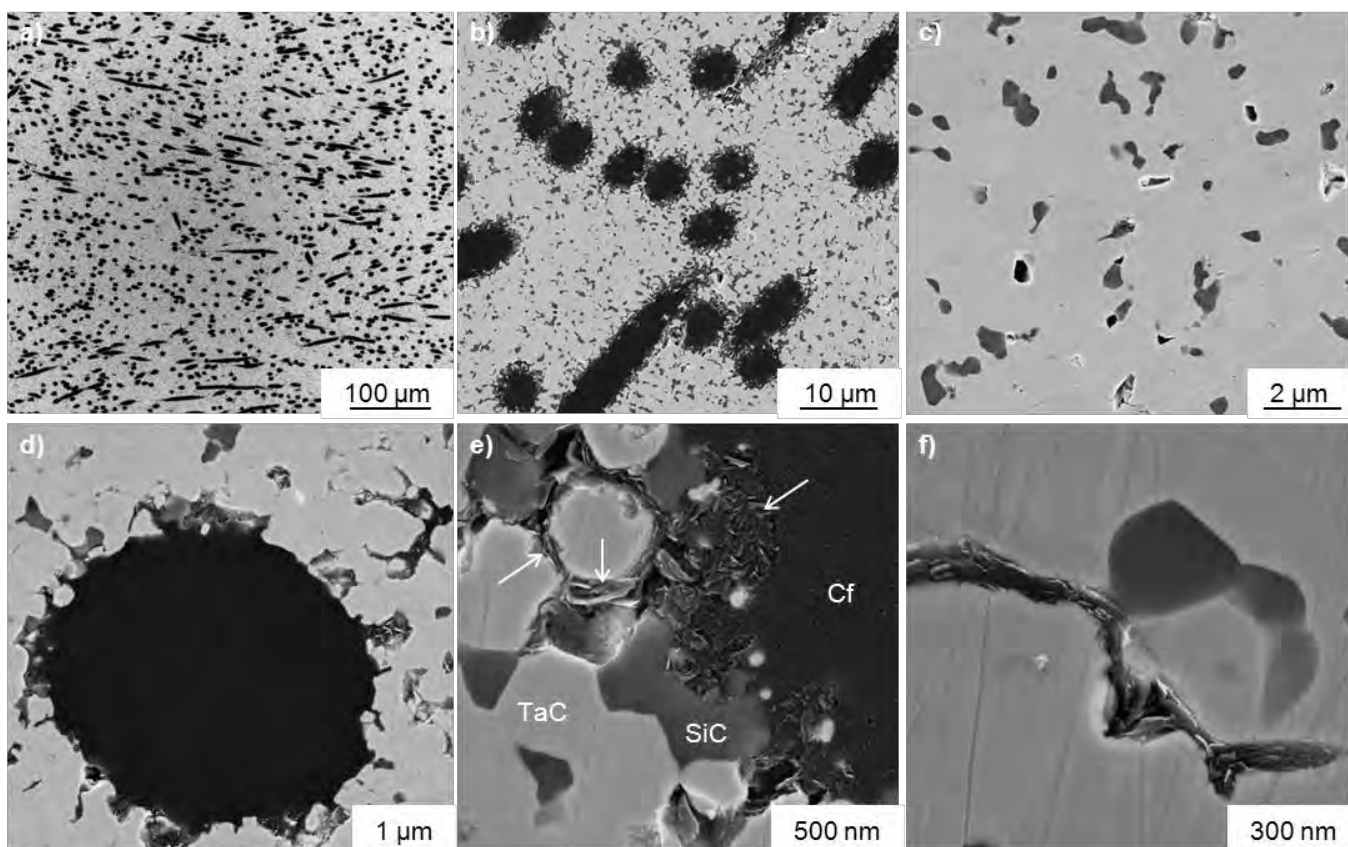
Figure 40: HR-TEM images of a)-c) TaC/SiC interfaces or d)-f) fiber/Ta₅Si₃/TaSi₂ interfaces.



3.4.6. TaC + C fiber

This composite with 15 vol% of C fiber and 5 vol% of Si_3N_4 was sintered at 1800°C and reached a relative density around 98%. Good fiber homogenization was achieved, as testified in Fig. 41a, with little residual porosity, mainly in proximity of the fiber. Fig. 41b. The sintering additive tended to react with the carbide matrix and the fiber and was mostly converted to SiC which was found spread throughout the matrix and at the TaC-fiber interface, Fig. 41c. An example of the fiber cross section is shown in Fig. 41d, where it can be seen that carbon branches started to depart from the fiber and incorporate either TaC or SiC grains, Fig. 41e. Graphitization of some regions of the fiber external part occurred and graphite pockets were occasionally found among TaC grains, Fig. 41f. TEM images of this composite are shown in Fig. 42 and revealed that the fiber almost lost its PAN-derived structure, graphite reflections were recognizable in the diffraction pattern of Fig. 42c, but a lot of amorphous phase was present too. On the other side, TaC matrix in high-resolution mode showed highly defective structure indicating lattice strain, Fig. 42d. High resolution images of the fiber-TaC interfaces were occasionally wetted by a Si-C-O amorphous phase, Fig. 43, whilst TaC/SiC showed mainly non-wetted grain boundaries, Fig. 44.

Figure 41: SEM images of polished section of TS-C showing a) the fiber distribution, b) the overall microstructure, c) scattered SiC in the matrix , d) a fiber section, e) a magnification of the fiber/matrix interface with arrows indicating graphite flakes and f) graphite sheets throughout TaC grains.



DATE	03/06/15
------	----------

Figure 42: a), b) TEM images of fiber debris with HR-TEM of c) C fiber with diffraction pattern showing graphite reflections and d) TaC matrix showing lattice strain.

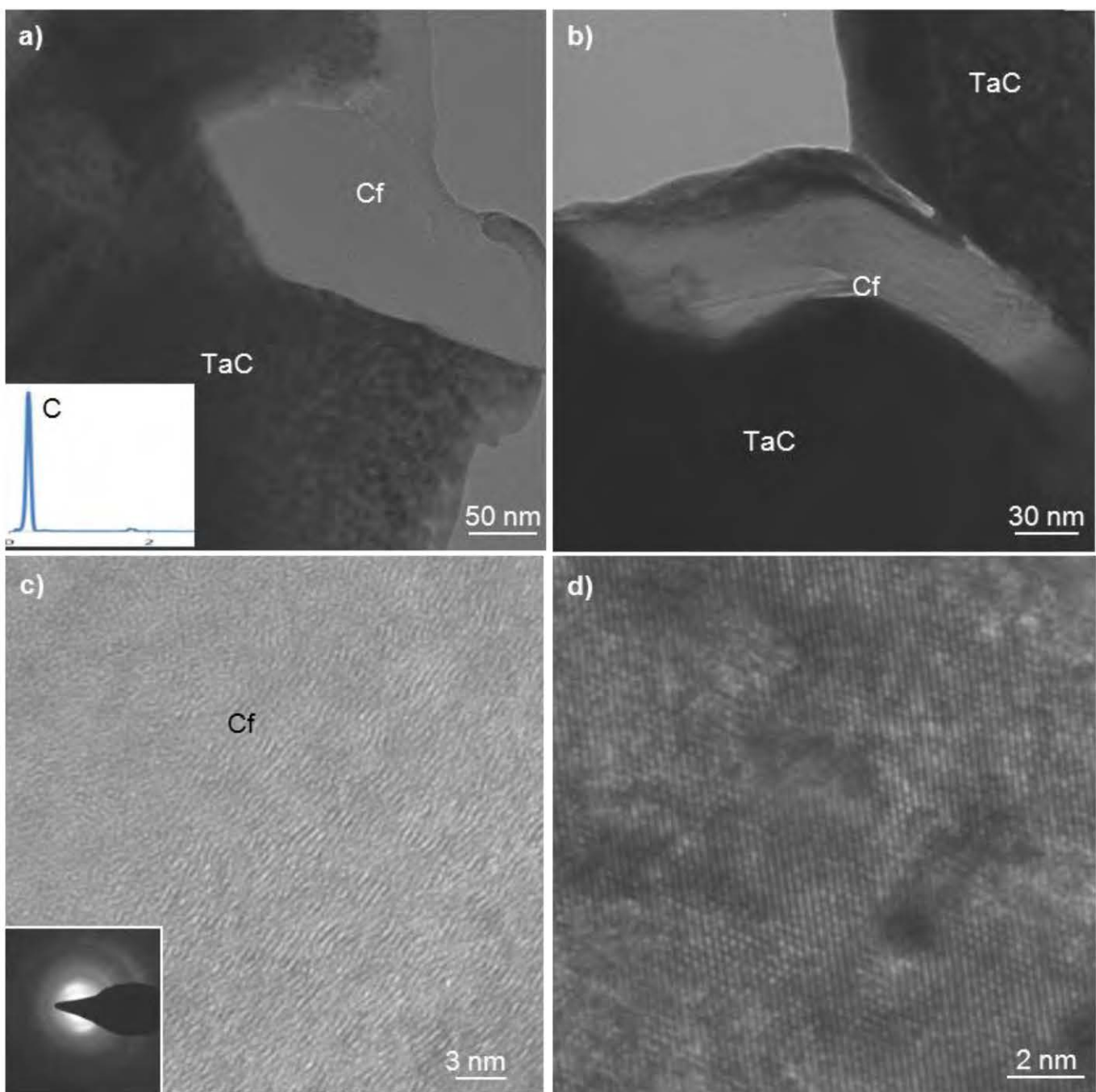


Figure 43: HR-TEM images of Cf/TaC interfaces showing a)-c) clean grain boundaries or d)-e) wetted interfaces with EDS spectrum of the amorphous Ta-Si-C-O phase.

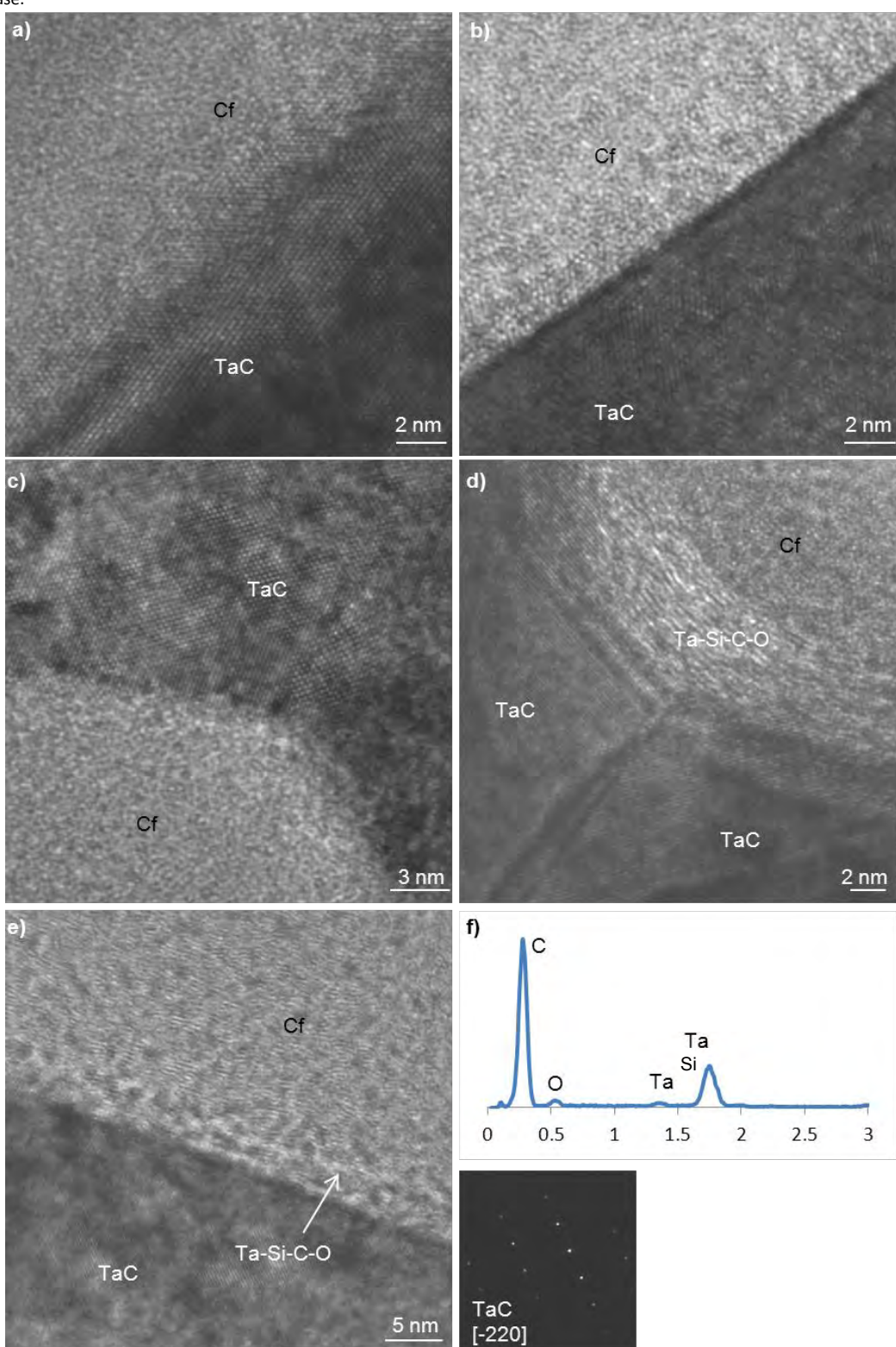
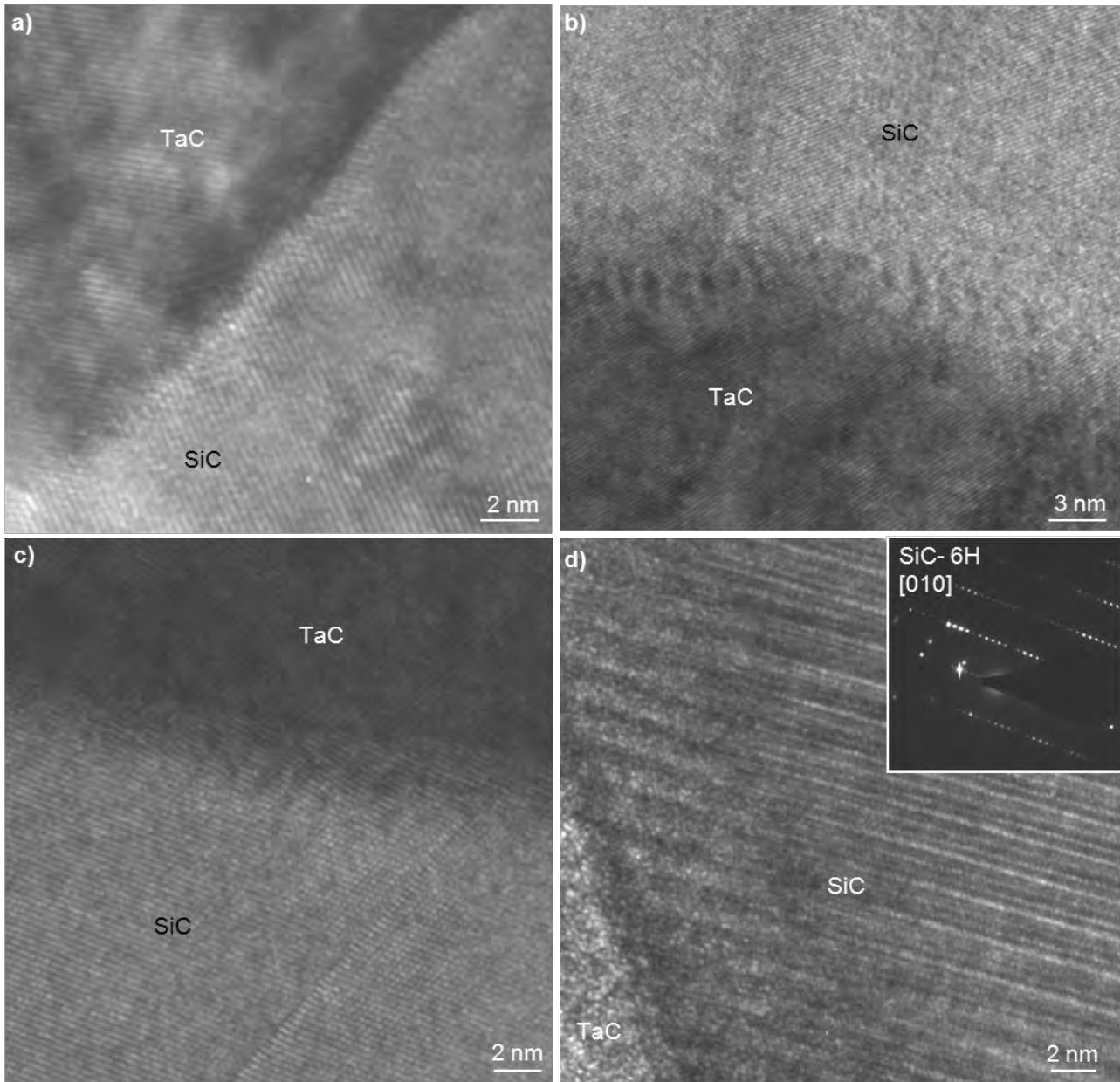


Figure 44: Examples of HR-TEM images of SiC/TaC interfaces showing clean grain boundaries.

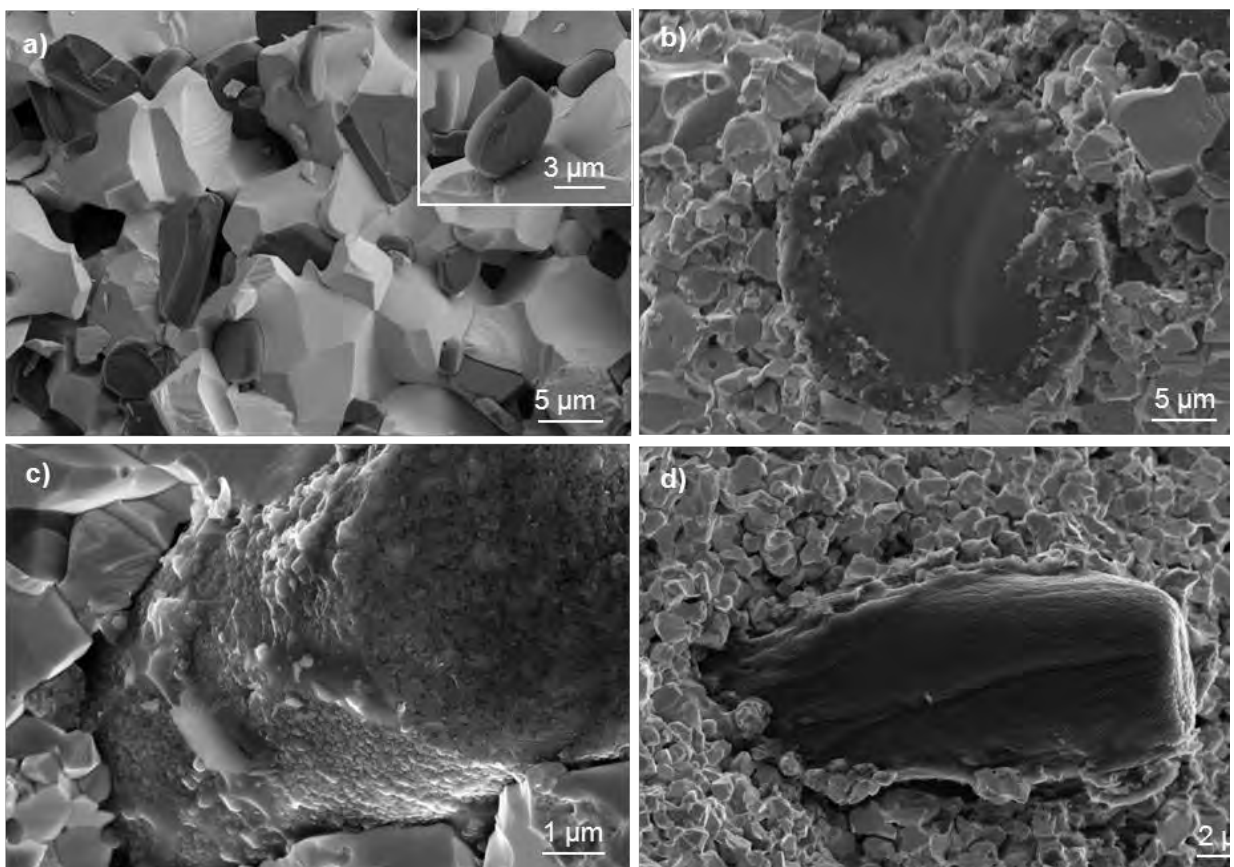


As for the fracture surface of the fiber and platelets composites, all of them showed interesting features, Fig. 45. For example, the fracture surface of in-situ grown SiC platelets, augmented the intergranular characteristics of the ceramic, Fig. 45a. Then, in the case of Hi-Nicalon fiber, Fig. 45b, fibers pullout was easily found even if a continuous rough layer surrounded the fibers. It seems that, in this case, the wide interface reaction phase was weakly bonded to the matrix and helped the fibers pullout, but at the same time diffused fibers degeneration occurred and thus the load transfer from the matrix was not as effective as hoped for. In the case of Tyranno SA3, Fig. 45c, the fibers were

DATE	03/06/15
------	----------

generally cut across, but also in this case it was not difficult to find some protruding fiber. Finally, when C fibers were added, carbon acted as weak interphase and fiber pullout or tearing were frequent, as Fig. 45d shows.

Figure 45: SEM images of fracture surfaces of TaC-based materials a) TM-S, b) TT-HN, c) TT-T, d) TS-C.



3.5. Morphology evolution of fibers and platelets

SiC platelets – The formation of SiC platelets is a consequence of prolonged thermal treatment at temperature above 1900°C to enable the $\beta \rightarrow \alpha$ SiC polytypic transformation. MoSi₂ was selected as sintering aid in view of its role in favoring the densification through formation of transient liquid phases^{16,17} and of its refractoriness at high temperature. Little amount of liquid phases formed at 2010°C, owing to the eutectic between MoSi₂ and SiC,⁴³ certainly helped the local rearrangement and agglomeration of SiC rounded particles and favored their evolution to platelets leaving clean grain boundaries with the matrix. According to the model proposed by Xu et al.⁴⁴ α -SiC nucleates heterogeneously at twin boundaries, stacking faults and twins, as these planar faults resemble local regions of α -SiC and therefore facilitate its nucleation. As thermal treatment proceeded, coarsening of SiC grains occurred by dissolution of the smaller β -SiC particles into the liquid and re-precipitation on the β/α -SiC composite

grain along the α -SiC side, owing to its higher stability at these temperature and higher growth rate as compared to that on the β -SiC regions. A sketch of the evolution of SiC particle to platelet during sintering is depicted in Fig. 46a.

Hi-Nicalon fiber – Comparing Fig. 26b and 34a, it is evident that remarkable reactions took place during sintering in presence of $TaSi_2$, even if the maximum temperature was relatively low, 1750°C. Similar sintering temperature were used for borides reinforced with the same SiC chopped fibers, but these resulted much less damaged,¹ therefore $TaSi_2$ and the carbide matrix seem to be responsible for the fibers degeneration. The instability of such kind of fiber is mainly due to the amorphous Si-C-O phase, decomposing above 1500°C into SiO/CO and SiC ,⁴⁵ and the presence of free turbostratic carbon; SiC nanocrystallites just tend to coarsen when exposed to high temperature.

The resulting fiber aspect is a combination of several factors. First $TaSi_2$ easy dissociates in reducing environment according to (6), favorable above 1100°C:^{16,17}



The formation of silicon is very probable and testified by the fact that the onset of densification temperature for this composite is very close to Si melting point, 1415°C. The decrease of $TaSi_2$ content after sintering and the presence of Si-based phases in the final microstructure are consistent with the occurrence of reaction (6). The formation of SiC phase could derive from the carburization of silicon according to (7):



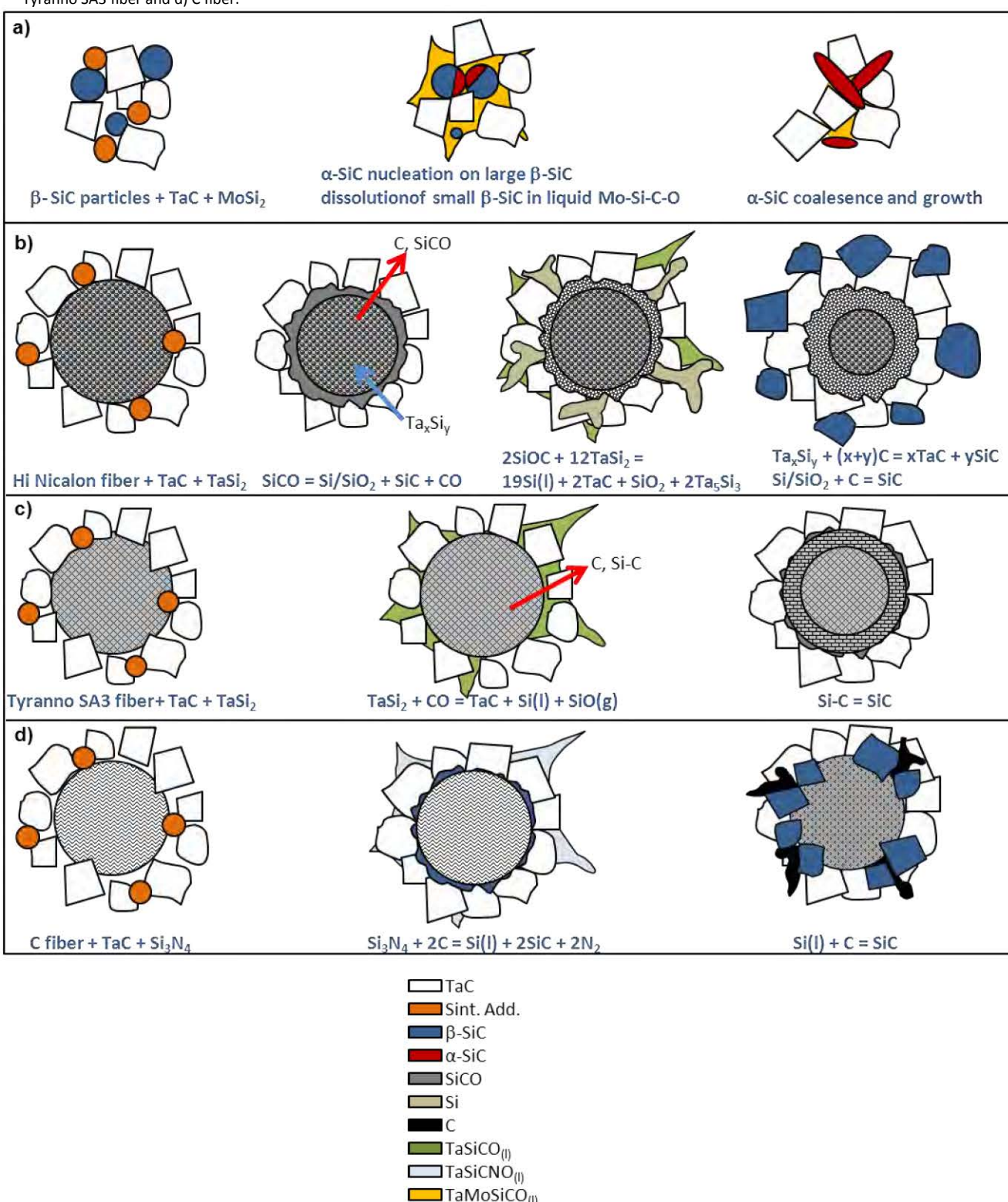
Other important players are the moving species in the fibers: C and SiCO. It is very probable that Ta-Si species and SiCO strongly interacted at the fiber/matrix interface, and that further Ta-Si phases were reduced to TaC by free carbon moving outwards from the fiber core. Possible reactions are then (8) and (9):



In addition, SiC crystallites of the fibers coarsened and provoked the fibers deformation and aperture. The coarse SiC particles which form a sort of crown surrounding the first TaC-ring might have origin from the liquid Si squeezed out from the fiber, which was carbo-reduced to SiC by the reducing atmosphere. A sketch of the evolution of Hi-Nicalon fiber during sintering is depicted in Fig. 46b.

Tyranno SA3 fiber – This type of fiber is more refractory and therefore more stable, SiC crystallites are coarser, less oxygen is present, only small amount of partially amorphous Si-C and intergranular carbon are present among the crystallites.³² As consequence, the differences between raw and sintered fiber, Fig. 26c and 37e, are not so dramatic as for Hi-Nicalon fiber. In the sintered fiber no particles were embedded into the fiber, just the outer part was C depleted and denser. SiCO-based glass pockets found at the interface can be due again to the reaction between $TaSi_2$ and its subproducts and the partially amorphous Si-C phase. A sketch of the evolution of Tyranno fiber during sintering is depicted in Fig. 46c.

Figure 46: Sketch of the morphology evolution of platelets and fibers in the TaC-matrix during sintering. a) SiC particles, b) Hi-Nicalon fiber, c) Tyranno SA3 fiber and d) C fiber.



Cfiber – Carbon fiber retained their shape close to the original one, Fig. 26d and 41d. No continuous SiC interlayer formed between fiber and matrix, just the fiber edges were irregularly open after reaction with silicon nitride to form silicon carbide and graphite, according to (10):

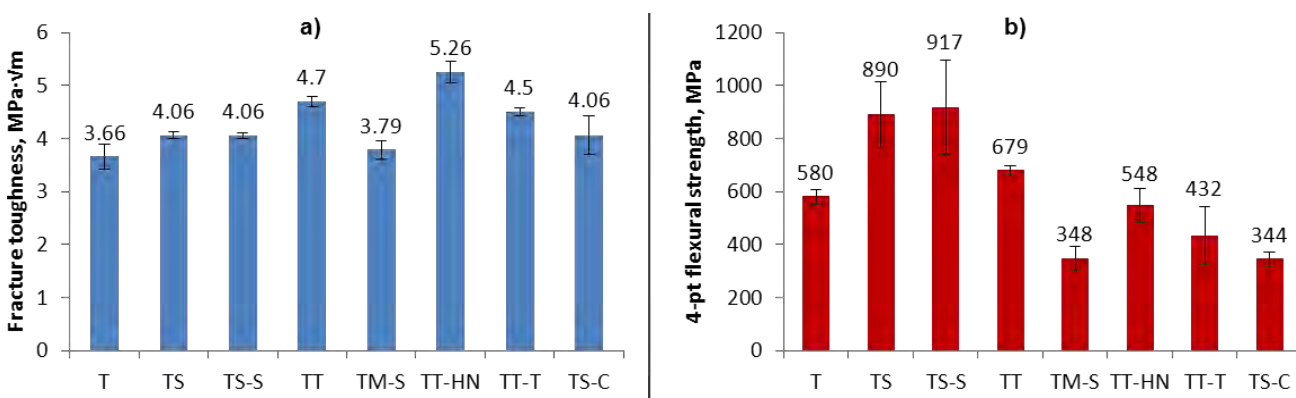


The evolution of nitrogen possibly slowed down the densification process, owing to the increased viscosity of the Si-based liquid phase.⁴⁶ Clean grain boundaries enabled fiber pullout, especially in the areas where SiC was not present. High resolution TEM also evidenced that the PAN structure of the fiber was lost after sintering above 1800°C. The intrinsic change of the fiber morphology may have compromised the mechanical properties. The evolution of carbon fiber during sintering is sketched in Fig. 46d.

3.6. Mechanical properties

The properties of the composites are plotted in Fig. 47. It can be rapidly noticed that the fracture toughness and strength are dependent on the type of reinforcing agent used. Fracture toughness ranges from 3.7 to 5.3 MPa·Vm, Fig. 47a, whilst the strength ranges from 350 to 900 MPa, Fig. 47b. When solely Si_3N_4 was used as additive, TS, notably higher strength was obtained, exceeding 900 MPa, and the results were not significantly different from the addition of 15 vol% of SiC particles (TS-S), just the standard deviation increased owing to particulate agglomeration. However, in the case of carbon fiber addition, the strength decrease was definitely more dramatic, as it passed from 650 MPa for a volume of fiber of 30%, with a net decrease of 62%.

Figure 47: Plots of a) CNB fracture toughness and b) 4-point flexural strength for TaC-based composites.



As for the room temperature flexural strength, it passed from 650 MPa for the unreinforced TT material, to 550 MPa for the Hi-Nicalon fiber-containing composite, which is a decrease of less than 20%, and to 430 MPa for the Tyranno fiber-containing composites, that is a decrease around 34%. Compared to the ZrB_2 -composites containing 20 vol% of fibers and sintered with addition of either Si_3N_4 or ZrSi_2 , the strength decrease was of the order of 30-50%.^{1,28}

For the present composites, the lower strength reduction in the case of Hi-Nicalon fibers could be related to the multiple effect of a coarser TaC matrix, 3-7 μm , of a fibers thinning from 200 to 50 μm length and of the formation of SiC particulates of dimension around 10 μm , which is not extremely different from the dimension of TaC grains, fibers and the newly formed SiC particles. It follows that the fibers did not result so extremely bigger than the matrix and hence they did not constitute a defect population like it happened for the ZrB_2 -based composites.

3.7. Effect of reinforcing phase on fracture toughness and strength tradeoff

Bar plots of fracture toughness and strength in Fig. 47 evidence some differences amongst the composites analyzed and show that in most cases there is some tradeoff between these two properties. Several can be the toughening mechanisms taking place in composites: (I) pinning when the crack front bows in the matrix and remains pinned at the particles or fibers, (II) crack deflection or branching when the crack meets an obstacle and bifurcates or follows a more tortuous path reducing the stress intensity at the crack tip, (III) micro-cracking when the misfit between thermal expansion coefficients introduces a stress field which can produce spontaneous micro-cracks thus adsorbing energy during the fracture, (IV) crack bridging when the front of the crack passes beyond the reinforcing phase leaving it intact and bridging the fracture surfaces in the wake of the crack and (V) residual stress toughening if the particles have a higher thermal expansion coefficient than the matrix and create compressive local stress field in the matrix thus decreasing the stress intensity factor.

As for this last mechanism, thermal residual stresses in composites naturally arise owing to the coupling of different phases with different thermo-elastic properties. The magnitude of the residual stresses depends on the difference of elastic properties and coefficients of thermal expansion (CTE) between matrix and reinforcements multiplied by the temperature difference at which elastic stresses develop (ΔT). The proper evaluation of these tensile stresses in the matrix becomes particularly important when high temperature composites are considered, since ΔT for these types of composites is high enough to generate residual stresses in the order of the tensile strength of matrix itself. The evaluation of residual stresses in such types of composites is tricky and the results are not always in agreement with each other depending on the technique used. Measurements of residual stresses were performed through neutron diffraction, Raman spectroscopy and x-ray diffraction in ZrB_2 -SiC composites^{47,48} and pointed out that stresses begin to accumulate at $\sim 1400^\circ\text{C}$ during cooling from the processing temperature. Because of the fact that the CTE of the TaC matrix, $7.1 \cdot 10^{-6} \text{K}^{-1}$ ⁴⁹ is higher than that of SiC particles or fibers ($3.5 \cdot 10^{-6} \text{K}^{-1}$ for Hi-Nicalon fiber,³² $4.5 \cdot 10^{-6} \text{K}^{-1}$ for Tyranno SA3 fiber³² and particles⁵⁰), and even higher than that of carbon fibers, $2.5 \cdot 10^{-6} \text{K}^{-1}$ ⁵¹ as the composites are cooled from their final densification temperature, 1750 - 1900°C , TaC tends to shrink faster than the SiC/C particles or fibers. The result is a tensile stress state in the matrix, σ_m , and a corresponding compressive stress state in the reinforcing phases, σ_r , as calculated with Taya et al.'s model using the following relationships,⁵² plotted in Fig. 48.

$$\sigma_r = -\frac{(-f)\varepsilon^*}{f} \sigma_m \quad (11)$$

$$\sigma_m = E_m \frac{2f\beta\varepsilon^*}{(-f\beta + 2\beta + \nu_m + 3\beta(-\nu_m))} \quad (12)$$

where f is the reinforcement volumetric fraction and

$$\beta = \frac{1+\nu_m}{1-2\nu_r} \frac{E_r}{E_m} \quad (13)$$

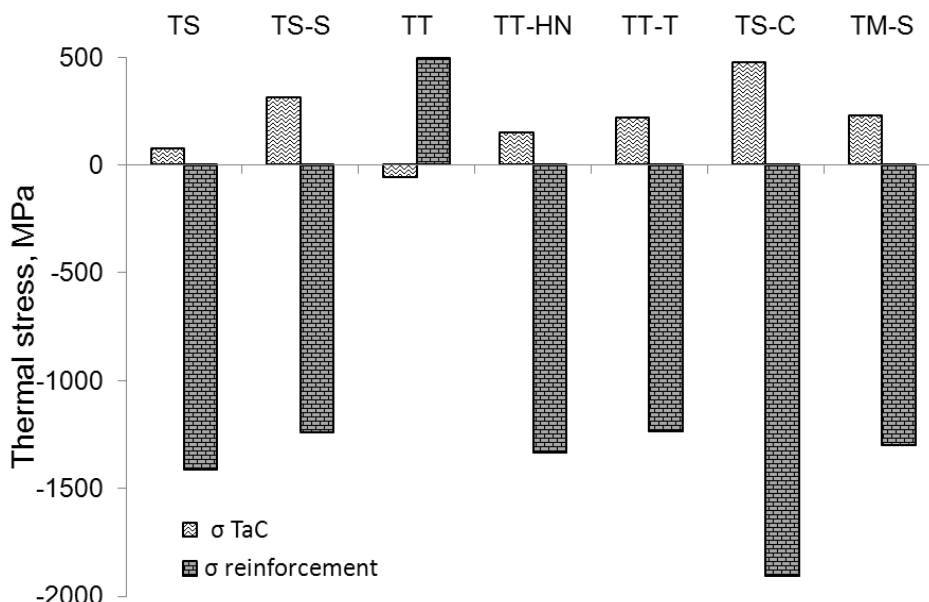
E_r , E_m , ν_r and ν_m are Young's modulus and Poisson ratio of reinforcement and matrix, respectively, and ε^* is the thermal expansion misfit strain given by:

$$\varepsilon^* = (\alpha_r - \alpha_m)\Delta T \quad (14)$$

where the α_r , α_m are the thermal expansion coefficients of reinforcement and matrix, respectively and ΔT is the temperature at which stresses begin to accumulate, set as 1400°C.⁴⁸

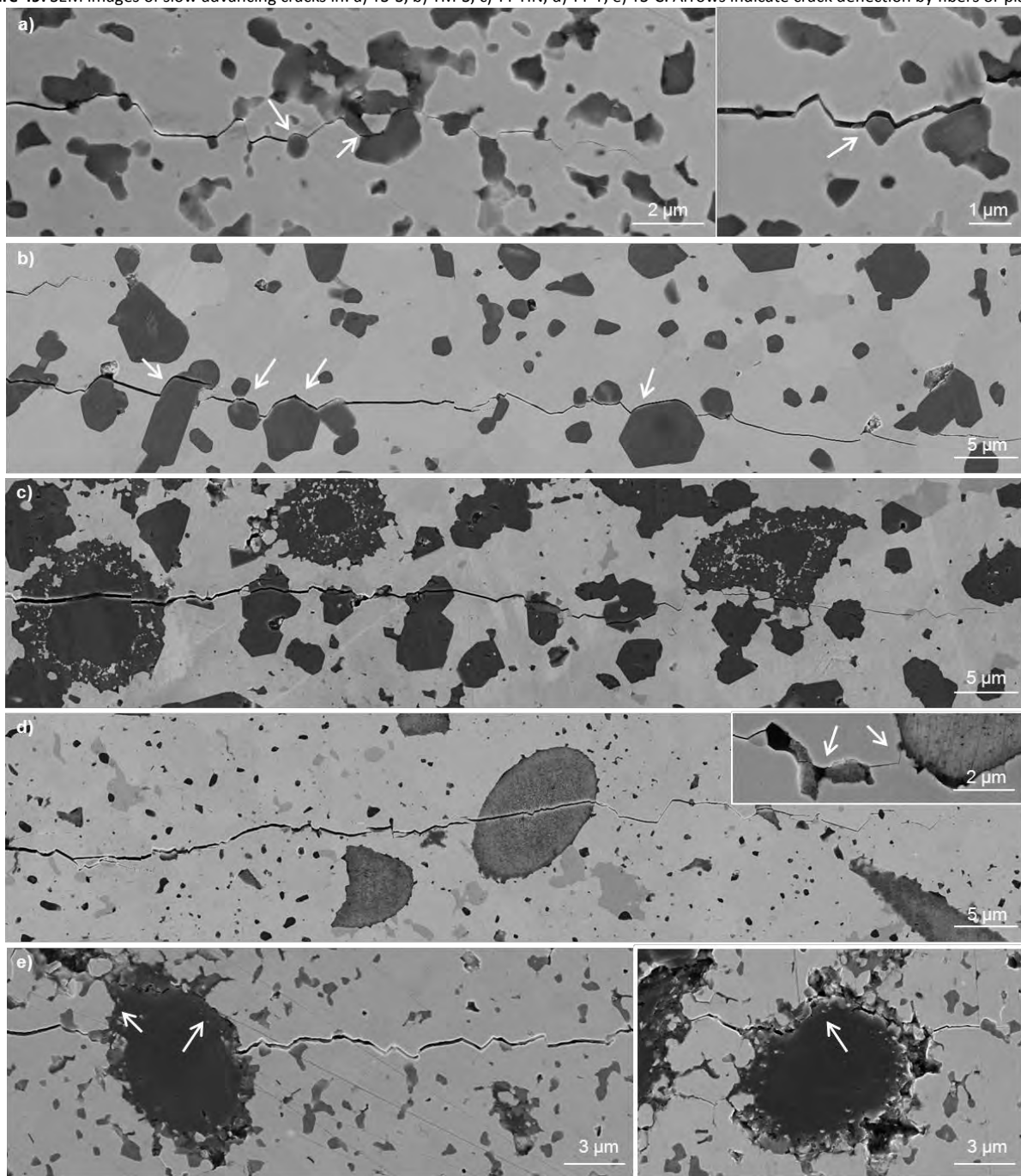
In the materials at hand, in most of the cases, the combination of TaC with the secondary phase implies a negative contribution to toughness due to the residual tensile stress in the matrix. The only case where the opposite conditions are verified is the combination of TaC with TaSi₂, which has a CTE of 8.2·10⁻⁶K⁻¹.⁵³ This material has in fact a higher fracture toughness than other TaC matrices, T or TS. The plot in Fig. 48 further evidences that tensile stress in the matrix increases increasing the amount of SiC particles (74 MPa in TS and 311 in TS-S) and also passing from partially amorphous fiber to a sintered one (148 MPa in TT-HN to 218 in TT-T). The worst case is the addition of C fiber which leaves a tensile stress of 477 MPa in the matrix.

Figure 48: Calculated thermal residual stresses in the TaC-based composites.⁵² $\Delta t=1400^\circ\text{C}$.



In order to understand if any positive contribute to toughness is active in the present ceramics, 98.1 N load indentations were introduced onto the polished surface to study the interaction of a slow advancing crack with the microstructure of the composites. Examples of this interaction are shown in Fig. 49.

Figure 49: SEM images of slow advancing cracks in: a) TS-S, b) TM-S, c) TT-HN, d) TT-T, e) TS-C. Arrows indicate crack deflection by fibers or platelets.



The crack propagation in pure TaC (material T) is mainly intergranular and its properties are mainly affected by its residual porosity and large grain size. Thus the addition of a sintering aid such as Si_3N_4 has the effect to improve the densification, decrease the matrix mean grain size and introduce small amount of SiC particles (material TS). As a consequence, the fracture toughness of TS is slightly higher than that of T, but its strength benefits of an increase of about 50% passing from 580 MPa to 890 MPa, Fig. 47b.

The addition of SiC particles to TS (material TS-S) does not produce further improvement either in strength or toughness. The crack path in Fig. 49a shows that SiC particles efficiently deflect the crack, so it is possible that the expected larger toughening contribution which derives from a larger quantity of the SiC phase is counterbalanced by the negative effect of increasing the residual tensile matrix stresses, Fig. 48.

The use of TaSi_2 as sintering aid (material TT) produces a different situation: the resulting composite is the only material with the TaC matrix under residual compressive stress, Fig. 48. The toughness is increased from $3.66 \text{ MPa}\cdot\text{m}^{1/2}$ of the pure TaC to $4.7 \text{ MPa}\cdot\text{m}^{1/2}$. A comparable increase in strength is also observed.

When MoSi_2 is used as sintering aid and SiC platelets formed after sintering (material TM-S), there was no improvement in toughness. Also for this composite, as for TS-S, the toughening due to crack deflection, see Fig. 49b, is counterbalanced by the tensile residual stress in the matrix. However, in this case, a drastic strength drop was measured. This is the result of the matrix grain coarsening and platelet agglomerations which acted as critical defects.

When Hi-Nicalon SiC fibers were added (material TT-HN), the crack proceeds straight through the fiber but it is deflected by the SiC platelets detached during sintering, Fig. 49c. The TaC matrix is under tensile residual stresses, however this composite was the toughest among those considered ($5.3 \text{ MPa}\cdot\text{m}^{1/2}$): its improvement with respect to pure TaC (T) is about 44% and of about 10% with respect to the starting matrix (TT). The fracture toughness value achieved well compares to the values measured for borides containing the same type of fiber.^{1,28} For those chopped Hi-Nicalon fiber- ZrB_2 composites, crack pinning was supposed to be the main mechanism that justified the observed increases in toughness from 3.5 to $5.3 \text{ MPa}\cdot\text{m}^{1/2}$ and overpassed the negative contribution given by residual stresses.^{1,28} The strength of composite TT-HN is however lower than that of TT. Very likely the size of the reinforcement now represents the dimension of the critical defects.

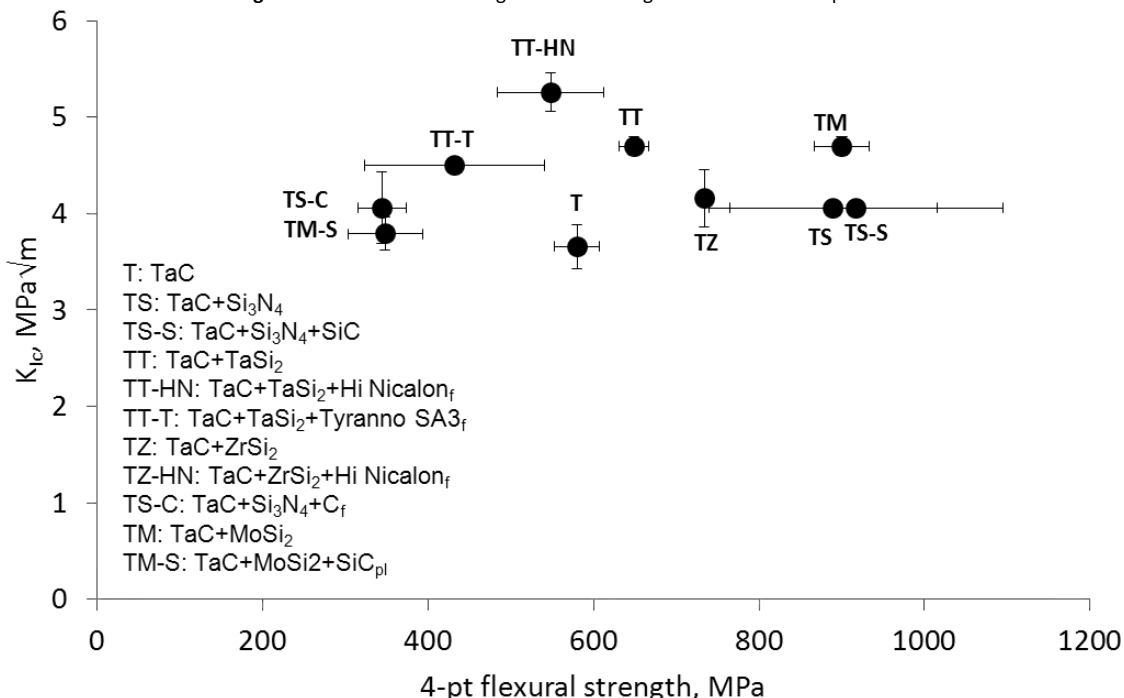
Similarly, in the case of Tyranno SA3 (material TT-T), most of the times the fibers are cut across, however, if the fiber is arranged along the longitudinal direction of the advancing crack, the fissure hits the fiber, proceeds along the fiber/matrix boundary and circumvents it, see the inset in Fig. 49d. As overall result toughness doesn't change, $4.5 \text{ MPa}\cdot\text{m}^{1/2}$, with respect to the starting matrix. The main difference between TT-HN and TT-T is the crystallinity degree of the reinforcement, as the final diameter of the fiber is nearly the same (about $7 \mu\text{m}$), Table 5. Since the toughness of TT-T did not change as compared to TT, we infer that the crystalline Tyranno SA3 must introduce more tension in the matrix compared to the Hi-Nicalon fibers. The estimations of the residual stresses reported in Fig. 48, are in fact based on the pristine values of the fiber. After sintering, however, they underwent different microstructural

modification so that the final properties of the fiber are definitely modified with respect to the starting ones. A more refractory fiber, as the crystalline Tyranno SA3, has more chance to maintain properties closer to the initial values and it is very likely that the calculated residual tensile matrix stress is closer to the true value than in the case of Hi-Nicalon fiber which is strongly modified after the sintering process. In addition, Hi-Nicalon fiber debris transformed into particles may have induced further toughening through crack deflection mechanism in TT-HN. These debris are not present in the case of Tyranno SA3.

When carbon fibers are added (material TS-C), the crack mostly goes around C fiber, Fig. 49e, but on the other side the graphite sheets and fragments spread among TaC grains weakens the overall microstructure, resulting in a null toughness increment. In addition the CTE of the C fiber is even lower than that of SiC and very different from that of TaC, so additional thermal residual stresses develop and adversely affect the toughness by counterbalancing any toughening mechanism. The strength is much lower than the starting matrix TS due to large fiber dimension which act as fracture origin.

The plot in Fig. 50 shows the relationship between strength and toughness of the just presented materials with other TaC-based ceramics available in the literature characterized with the same CNB method and 4-point flexural strength.¹⁶ It is apparent that TaC can achieve very high strength approaching 1 GPa, but in general the fracture toughness remains one key issue, as residual stress arising from the secondary phases prevents from notable improvements of the failure tolerance of these TaC-based ceramics.

Figure 50: Plot of fracture toughness and strength of TaC-based composites.



3.8. Conclusions on TaC based ceramics

In order to increase the fracture toughness of TaC, secondary phases were added: a transition metal disilicide, SiC in form of particles, platelets, and chopped fiber, or C short fibers. The microstructure of the ceramics and the evolution of the secondary phase added were studied by SEM and TEM and correlated to strength and fracture toughness. TEM analyses were essential to reveal the structural modification at nanoscale level of fiber and matrix.

A toughness increase was not always observed probably owing to the negative effect of thermal residual stresses, due to the introduction of lower CTE secondary phases. Conversely, high strength increase was obtained when SiC particles were added, approaching 1 GPa. TaSi₂ enabled a toughness increase up to 4.7 MPa·Vm, owing to suitable tensional state arising in the composite, and strength around 680 MPa was measured. The highest toughness was found for addition of Hi-Nicalon fibers, 5.3 MPa·Vm, coupled with a strength of 550 MPa. When Tyranno SA3 SiC fibers were introduced, no appreciable toughness increment was measured, again due to negative thermal residual stresses. The less favorable case was found for addition of C fiber that introduced too high tensile stress in the matrix and frustrated any positive contribution given by crack deflection and pinning of the fibers.

Oxide-based ceramics

Alumina and Zirconia are certainly not intended for application in ultra-high temperature environments, however two composites were produced with a twofold purpose. The first was to study the interactions between Hi-Nicalon fiber and the oxide matrix and the second was to obtain a material where the matrix possesses lower Young's modulus than the fiber. In this respect, two oxide-based composites, namely Al₂O₃ and ZrO₂ containing 15 vol% of Hi-Nicalon SiC chopped fiber, were hot pressed and characterized by scanning and transmission electron microscopy. Nanoindentation tests were performed to investigate the local properties of fiber and matrix. Fracture toughness and room temperature strength measurements are in progress.

3.9. Reinforced oxides

Table 6 summarizes the sintering parameters adopted for the hot pressing runs, the main microstructural features and the mechanical properties of the oxide based composites. Two baseline bulk oxides AO and ZO, were produced for reference.

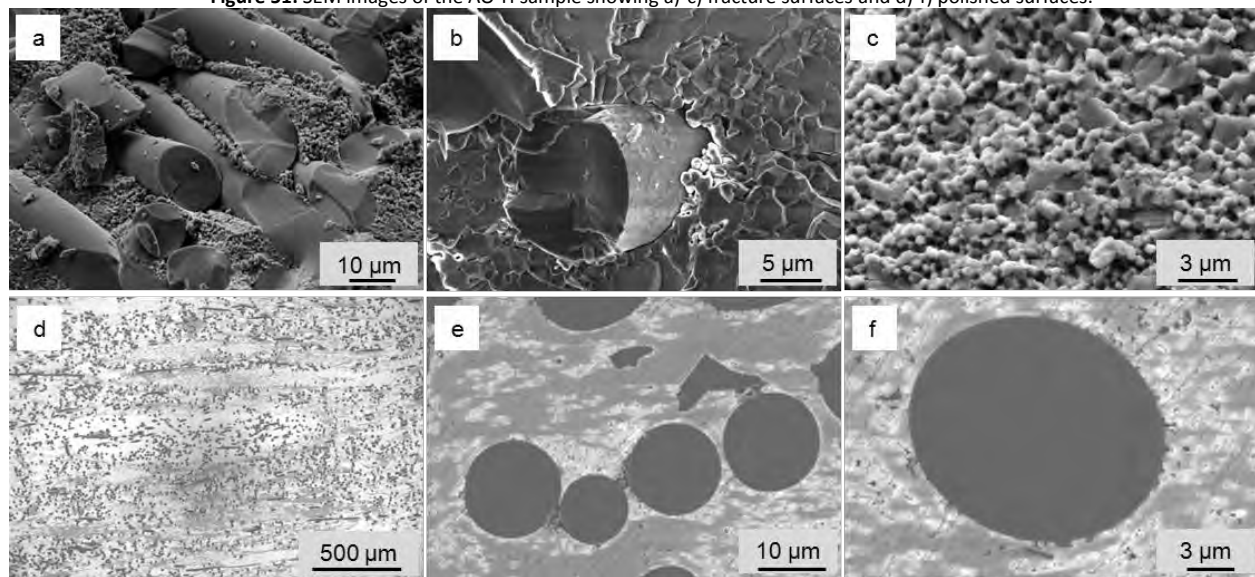
Table 6: Composition, sintering conditions, main microstructural features and mechanical properties of Al_2O_3 - and ZrO_2 -based composites. ρ : density, m.g.s.: mean grain size, E: indentation modulus, H: hardness.

Sample	Matrix	Reinforce vol%	Sintering °C, MPa, min	Exp. ρ , g/cm ³	Rel. ρ %	m.g.s. μm	$E_{(200 \text{ mN})}$ GPa	$H_{(200 \text{ mN})}$ GPa
AO	Al_2O_3	-	1550,30,4	3.90	99.9	-	-	-
AO-H		20 Hi-Ni	1550,40,10	3.65	99.8	1.45±0.55	m: 417±14 f: 310±29	m: 24.5±0.6 f: 28.9±2.9
ZO	ZrO_2	-	1500,30,5	5.96	98.5	-	-	-
ZO-H		20 Hi-Ni	1500,30,5	5.38	99.9	0.29±0.07	m: 264±5 f: 251±42	m: 16.9±0.4 f: 27.7±4.9

3.9.1. Al_2O_3 + Hi-Nicalon

The ceramic based on Al_2O_3 containing 20 vol% of SiC chopped fiber achieved a density of 3.65 g/cm³ after sintering at 1550°C, which represents a densification level of 99.8%. SEM images of the sintered samples are reported in Fig. 51. The fracture surfaces in Fig. 51a,b display interesting features as fiber pullout is well evident indicating weak interfaces between matrix and fiber. A magnification of the matrix in Fig. 51c reveals the good density level and a mean grain size around 1.45 μm , notably coarser than the starting powder, 300 nm. In the polished section of Fig. 51d a good dispersion of the fibers was ascertained and these were homogeneously scattered throughout the matrix with sharp interfaces, Fig. 51e,f.

Figure 51: SEM images of the AO-H sample showing a-c) fracture surfaces and d-f) polished surfaces.



Microcracking was frequently found, probably owing to the coefficient of thermal expansion mismatch between the SiC fiber, $3.5 \cdot 10^{-6}/^\circ\text{C}$,³² and the Al_2O_3 matrix, $8.9 \cdot 10^{-6}/^\circ\text{C}$.⁴ TEM investigations revealed clean grain boundaries in the Al_2O_3 matrix, as the examples displayed in Fig. 52 and 53. However at the fiber/matrix interface, a

Si-O rich phase was found, Fig. 54. This was contaminated by Cu and Mo during the thinning procedure, but no metal diffusion within the fiber could be found. Previous investigations led indeed to conclude that Hi-Nicalon fiber are very sensitive to metal impurities during sintering which tend to be trapped in the fiber core and reduced to the corresponding silicide or carbide.¹ In this case, it seems that the fiber remained unaffected by the surrounding oxide during sintering or any other impurity during the following thinning. A high resolution image of the fiber microstructure is shown in Fig. 55a, SiC crystallites maintained the original size, around 5 nm, amorphous phase was still present, as confirmed by the diffraction pattern in Fig. 55b, and EDS analysis revealed Al traces coming from the fiber processing, see the spectrum in pattern in Fig. 55b.

Figure 52: TEM images of the AO-H sample showing clean grain boundaries in the Al_2O_3 matrix.

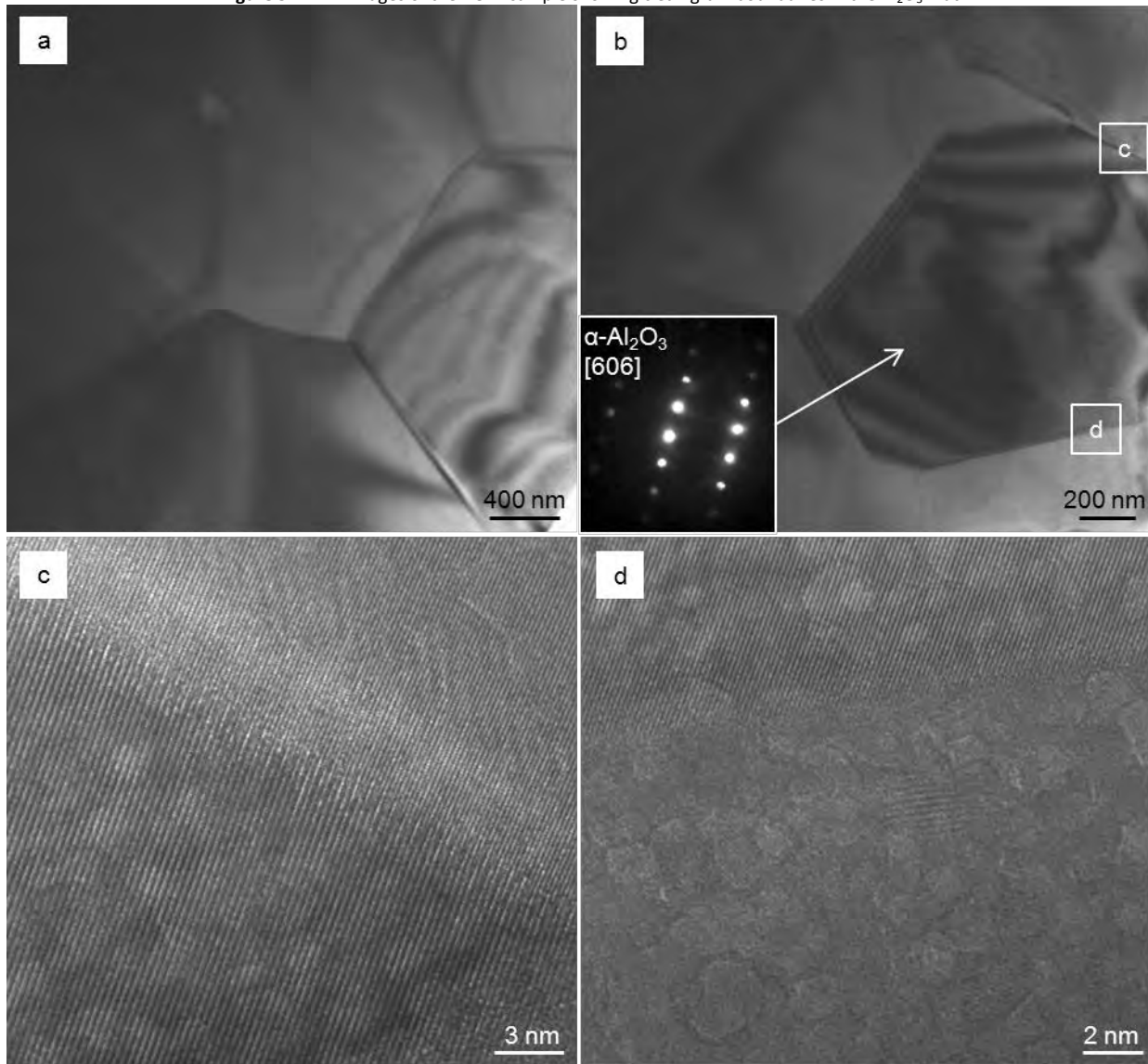


Figure 53: TEM images of the AO-H sample showing clean grain boundaries in the Al_2O_3 matrix.

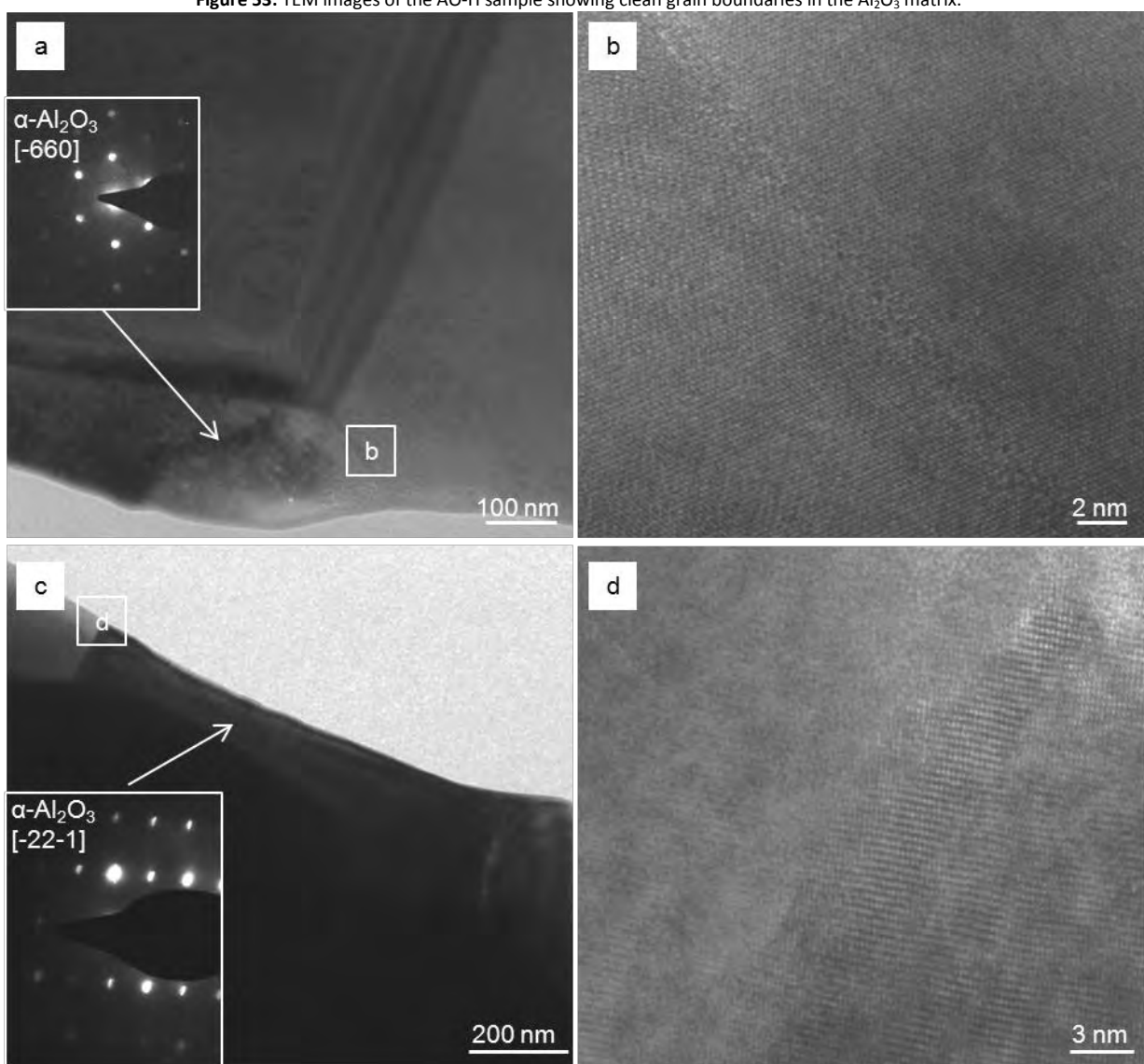


Figure 54: TEM images of the AO-H sample showing example of fiber/matrix interface with EDS spectra in c).

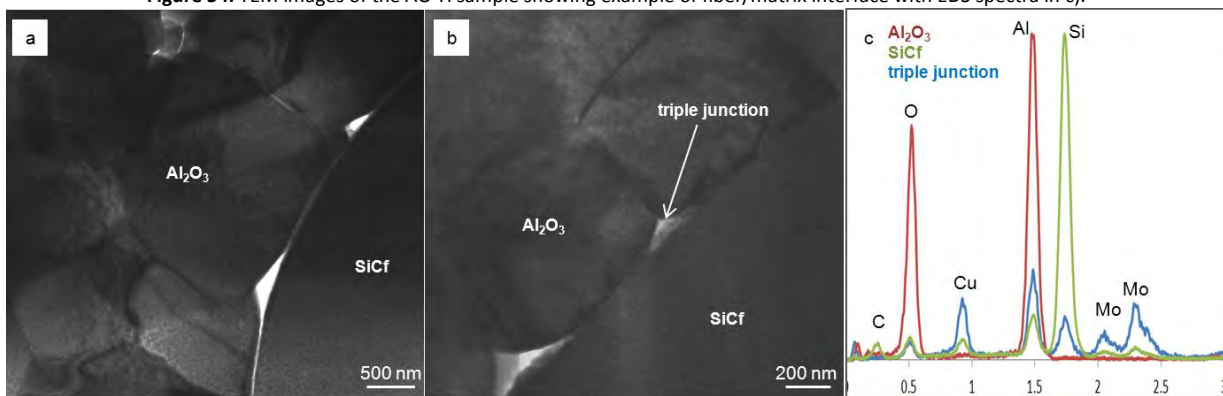
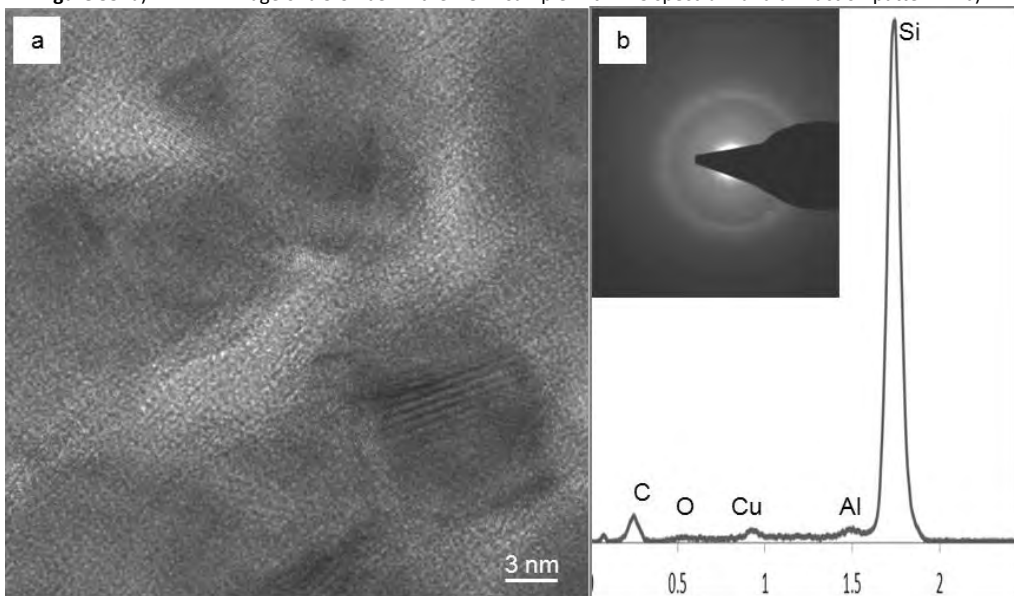


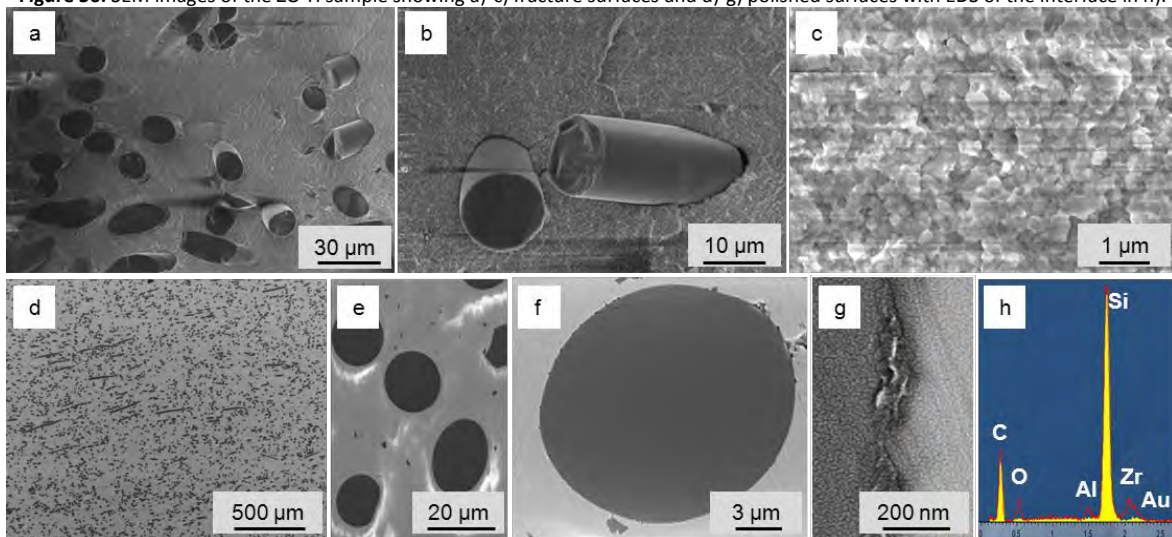
Figure 55: a) HR-TEM image of a SiC fiber in the AO-H sample with EDS spectrum and diffraction pattern in b).



3.9.2. ZrO₂ + Hi-Nicalon

The ceramic based on ZrO₂ containing 20 vol% of SiC chopped fiber achieved a density of 5.38 g/cm³ after sintering at 1500°C, which represents a densification level of 99.9%. SEM images of the sintered samples are reported in Fig. 56. Similar to the previous composite, also this one showed fiber pullout in the fracture surfaces of Fig. 56a,b and a fully dense matrix, Fig. 56c. In this case the mean grain size remained closer to that of the starting powder and resulted below 300 nm, compared to the initial 90 nm. In the polished section of Fig. 56d a good dispersion of the fibers was achieved and these were homogeneously scattered throughout the matrix with sharp edges, Fig. 56e,f.

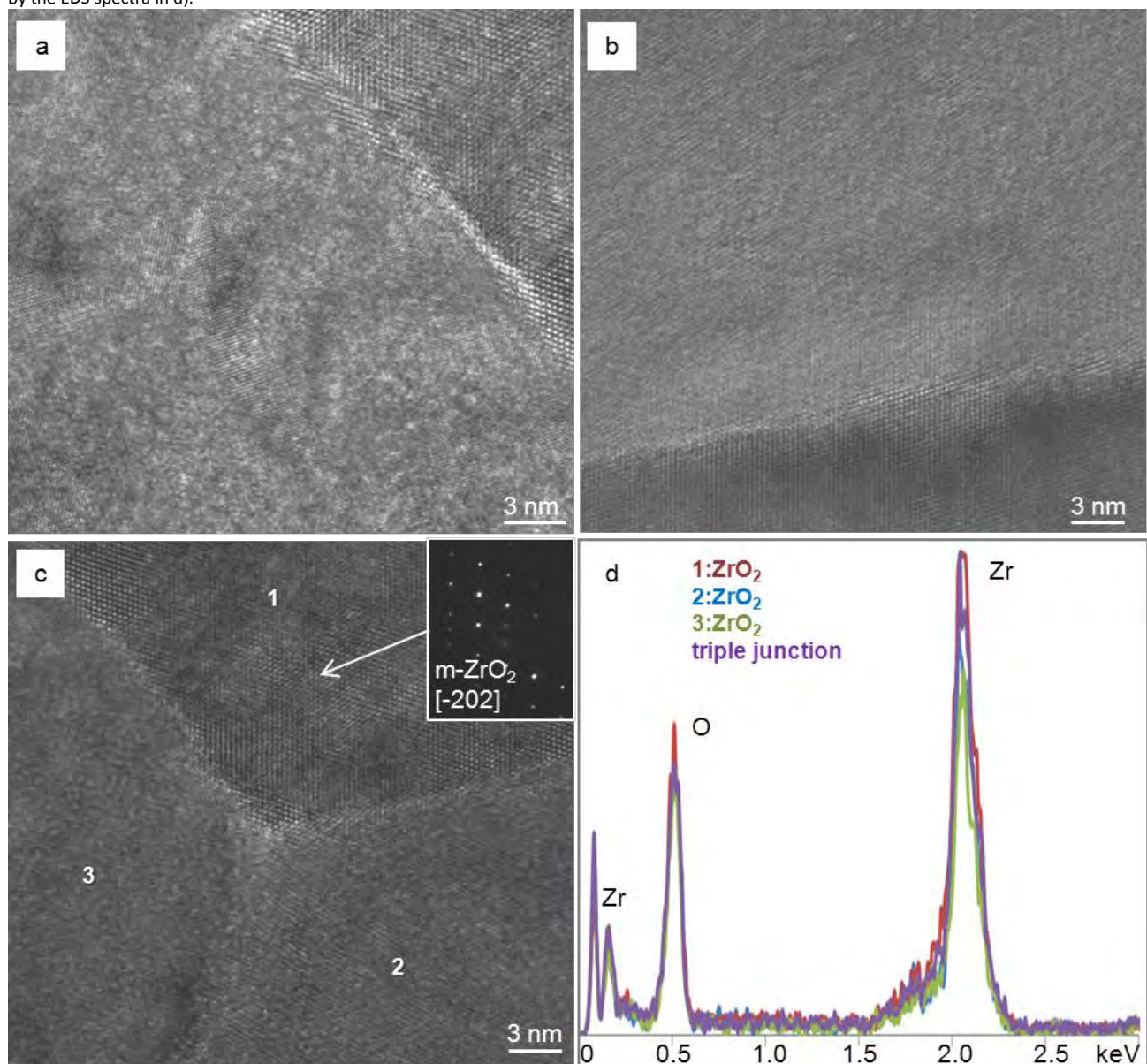
Figure 56: SEM images of the ZO-H sample showing a)-c) fracture surfaces and d)-g) polished surfaces with EDS of the interface in h).



At the fiber/matrix interface, some interphase was systematically found by SEM analysis, but EDS was not conclusive in defining its composition owing to the small area and the Au coating, Fig. 56g,h. Little dark particles were identified as fiber debris. The fiber didn't show any contrast or stratification, indicating that no substantial reaction occurred with the matrix, differently from what observed in borides and carbides with the same fiber type.^{1,28}

TEM analyses carried out in the matrix revealed clean grain boundaries among adjacent ZrO_2 grains and triple points free of secondary phases or impurities segregation, Fig. 57.

Figure 57: HR-TEM images of the ZO-H sample showing a)-b) clean grain boundaries and c) a triple point junction free of other phases, as confirmed by the EDS spectra in d).



The fiber morphology was confirmed to be homogeneous from the core to the periphery, with no phenomena of crystallization of the amorphous Si-C-O phase or coalescence of the SiC crystallites which remained in the range of 10 nm, Fig. 58. The matrix/fiber interface appeared sharp upon SEM inspection, but TEM revealed the presence of partially amorphous interfacial phase mainly based on C, as reported in the images and EDS spectra of Fig. 59. The presence of this C-rich phase could be a consequence of C migration from the fiber outwards, as previously observed for non-oxide ceramics. High resolution images of fiber/matrix interfaces are displayed in Fig. 60 and all show the interposition of a C phase with turbostratic features.

Figure 58: TEM images of the fiber in ZO-H sample showing the fiber morphology with β -SiC crystallites, turbostratic C and partially amorphous Si-C-O phase

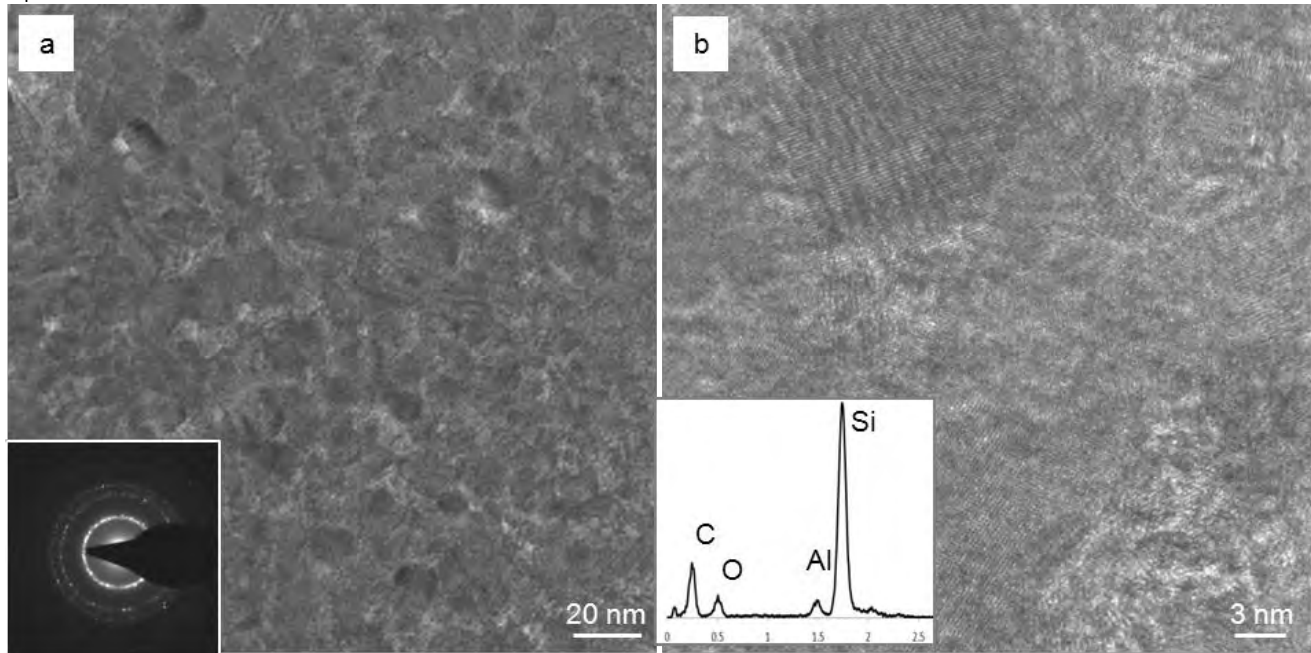


Figure 59: TEM images of the fiber/Matrix interface in ZO-H sample with HR-images and EDS spectra as indicated.

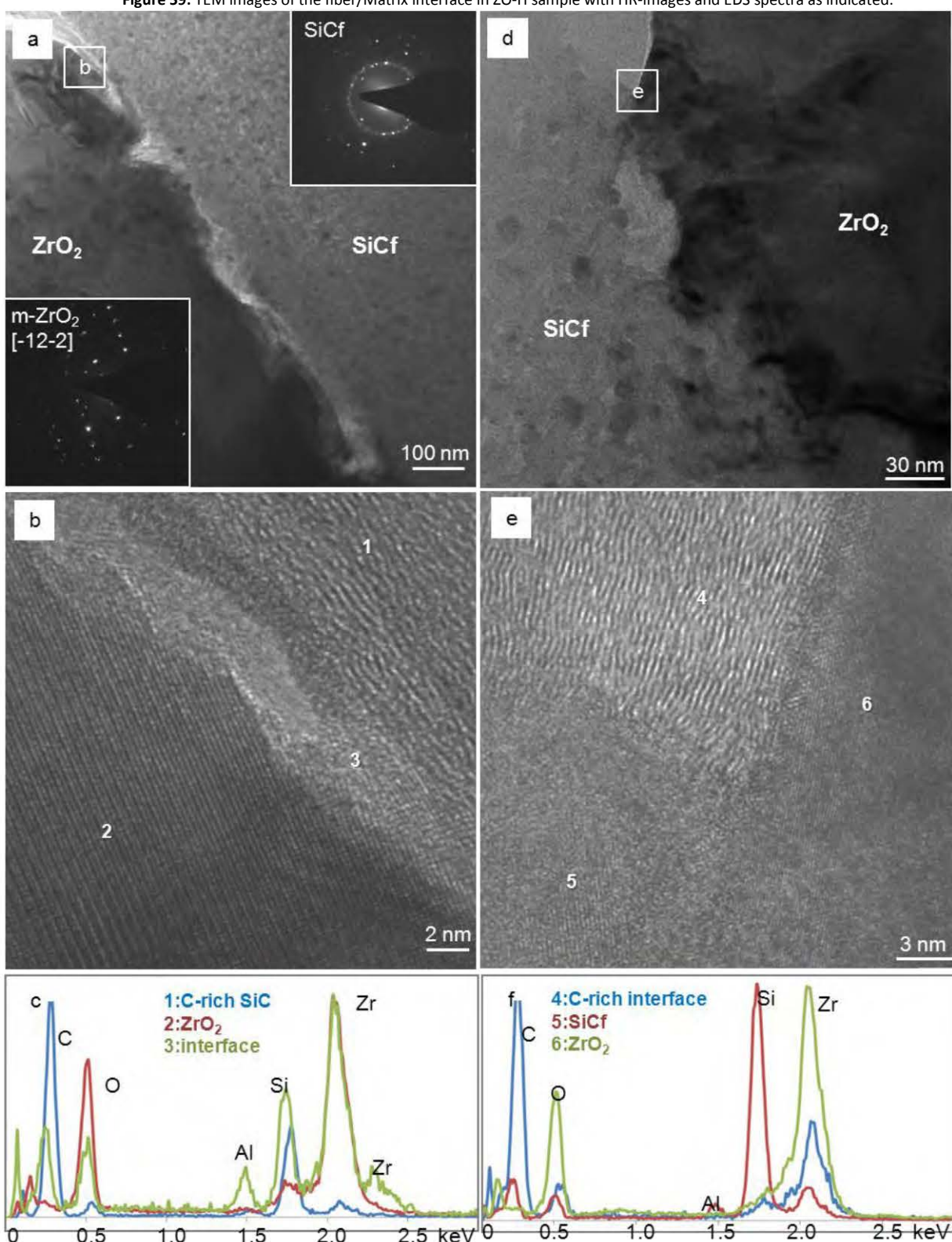
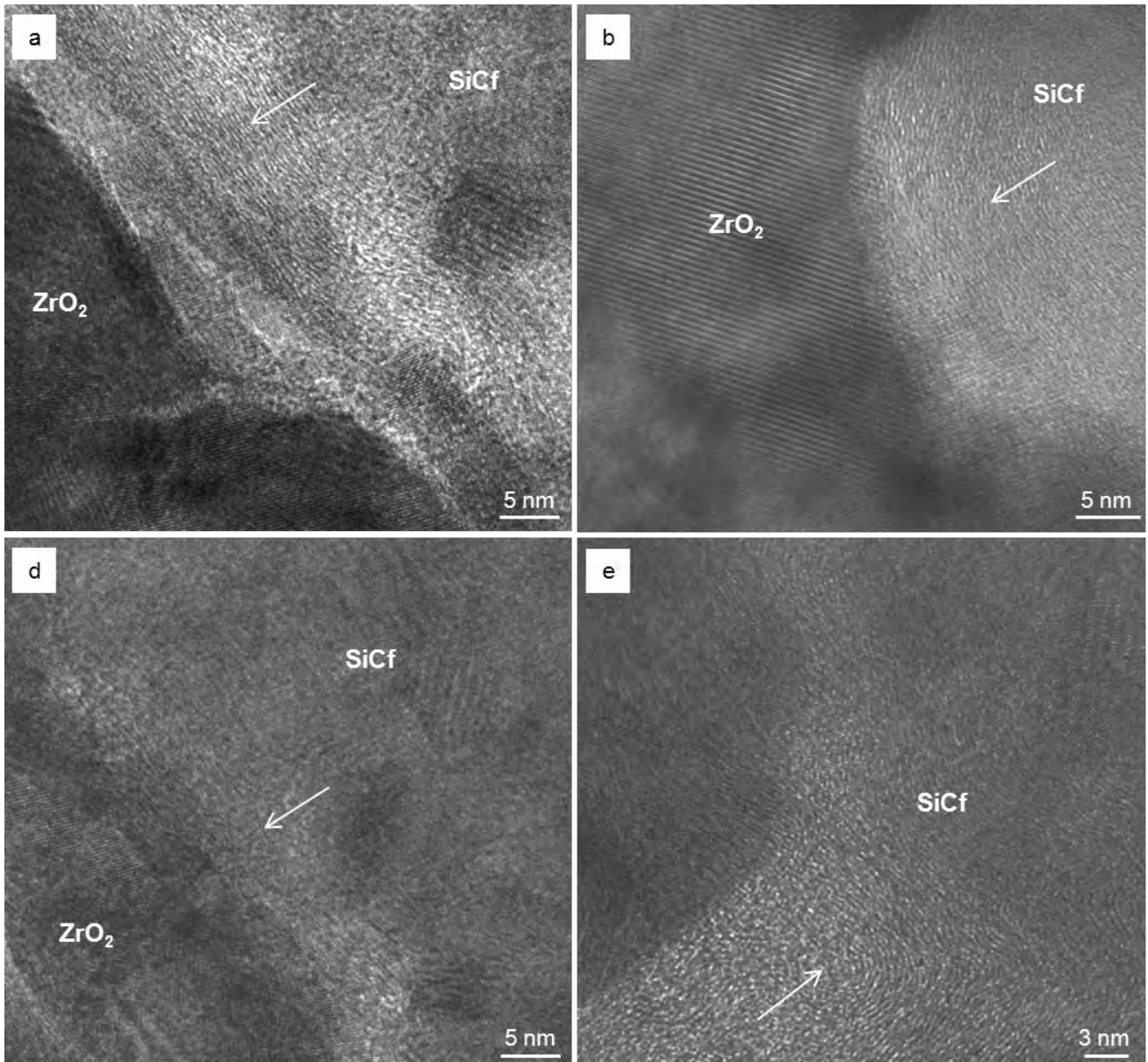


Figure 60: HR-TEM images of the fiber/matrix interface in ZO-H sample showing the presence of turbostratic carbon indicated by arrows.



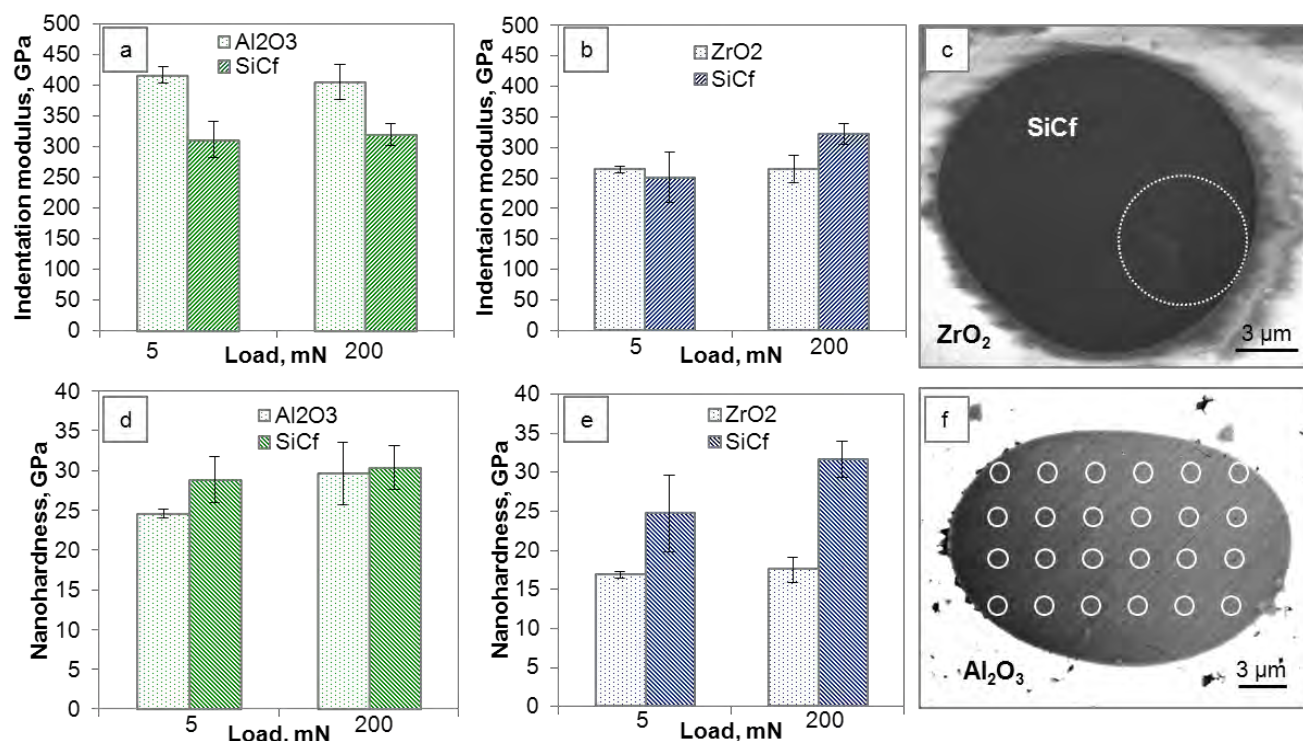
3.9.3. Nanoindentation

In order to investigate the mechanical behavior of the constituent phases, nanoindentation tests were carried out both on matrix and fibers. The purpose of using the 200-mN indentations was to measure the local mechanical properties (Young's modulus and hardness) of the matrix and fibers. The indentation results of Young's modulus and hardness for matrix and fiber are reported in Fig. 61a,b,d,e with an example of indentation on a fiber in Fig. 61c. The

DATE	03/06/15
------	----------

low-load tests were employed to detect any difference in the mechanical behavior across the fiber, see Fig. 61f for an example of the indentation grid used.

Figure 61: Nanoindentation results of the oxide reinforced composites. a), b) Young's modulus (E), d), e) nanohardness (H) with peak load equal to 200 and 5 mN. c) Example of a 200 mN indentation on a fiber in ZO-H and f) of an indentation grid in AO-H.



The histograms of Fig. 61a,b shows that the indentation modulus of the oxide matrices doesn't notably change increasing the load, 405-416 GPa for Al₂O₃ and 264 GPa for ZrO₂. As for the fiber, the indentation modulus is 310-320 in the Al₂O₃-based ceramic, always lower than the matrix, whilst varies from 250 to 320 in the ZrO₂-based, that is in the same range of the matrix values.

As for the hardness, Al₂O₃- matrix ranges from 25 to 30 GPa, ZrO₂ matrix is around 17 GPa and the fiber is around 29 in both composites, but with higher standard deviation in the ZrO₂-based one.

Nanoindentation results confirmed that no SiC coarsening or coalescence didn't occur during sintering, as the values of indentation modulus very well matched the reported Young's modulus for Hi-Nicalon fiber reported in the literature for raw Hi-Nicalon fiber, 270 GPa,³² and there was no significant difference between core and rim areas of the fiber, like previously observed for boride-matrices.¹

Measurements of fracture toughness and strength are in progress and will be correlated with the microstructural features and the local mechanical properties.

3.10. Conclusions on oxides

The study of two oxide-based composites, namely Al_2O_3 and ZrO_2 containing 15 vol% of Hi-Nicalon SiC chopped fiber, revealed interesting characteristics from the microstructural point of view. The fiber underwent no modification upon sintering at 1500-1550°C, maintained a well-rounded shape with sharp boundary and formed weak interfaces with the matrix, promoting intergranular fracture and extensive fiber pull-out. Totally different interactions between fiber and matrix were found for borides and carbides. Conditions for effective load transfer, i.e. matrix possessing lower Young's modulus than the fiber, were ascertained by nanoindentation. Preliminary mechanical results seem to indicate that the main obstacle to toughening of these oxides seems to be related to the negative contribution of residual stress arising from too different coefficients of thermal expansion of fiber and matrix.

4. Conclusive remarks

During the third year of contract, several ultra-high temperature ceramics and oxides were produced and characterized by transmission electron microscopy. The main outcomes are herein summarized.

- **$\text{ZrB}_2 + \text{WSi}_2$**

The sintering additive was suitable to enable a fully dense microstructure with clean grain boundaries and refractory phases at the triple junction that allowed to maintain a strength of 540 MPa at 1500°C in air. TEM was fundamental in revealing the core-shell morphology of the matrix grain and to disclose the nature and crystallinity of the secondary phases formed upon sintering.

- **$\text{ZrB}_2 + \text{refractory fibers}$**

Also 3rd generation SiC fiber, Hi-Nicalon S, are in non-equilibrium state in ZrB_2 matrices. Similarly to previous generation fibers, they tend to interact with sintering additive and undergo notable microstructural modification, especially above 1700°C. TEM analyses evidenced the microstructure at nanoscale level inside the fiber and revealed the chemistry and nature of the trapped particles. The application of a BN coating for processing of long Hi-Nicalon fiber resulted effective in blocking any reaction and structural modification, as the fiber maintained the pristine morphology. The use of BN-coated long fiber instead of short naked fiber didn't prove significant improvement in fracture toughness of ZrB_2 , owing to an unfavorable ratio between Young's modulus of matrix and fiber which didn't allow efficient load transfer. However, this composite resulted more damage tolerant showing non-catastrophic mode of failure.

- **$\text{TaC} + \text{reinforcements}$**

The microstructure of TaC materials containing different kinds of secondary phase (transition metal disilicide, SiC in form of particles, platelets, and chopped fiber, or C short fibers) was studied by SEM and TEM and correlated to strength and fracture toughness. TEM analyses were essential to reveal the structural modification at nanoscale level of fiber and matrix and to rebuild the microstructural evolution. Toughness and strength showed

a tradeoff trend. Toughness was mainly penalized by the negative contribute of thermal residual stresses, due to the introduction of lower CTE secondary phases. The highest toughness was found for addition of Hi-Nicalon fibers, 5.3 MPa·Vm, coupled with a strength of 550 MPa. The less favorable case was for addition of C fibers that introduced too high tensile stress in the matrix and frustrated any positive contribution given by crack deflection and pinning of the fibers.

- **Oxides + Hi-Nicalon fiber**

Preliminary studies on Al_2O_3 and ZrO_2 containing 15 vol% of Hi-Nicalon SiC chopped fiber revealed interesting characteristics from the microstructural point of view. The fiber underwent no modification upon sintering at 1500-1550°C, maintained a well-rounded shape with sharp boundary and formed weak interfaces with the matrix which enabled extensive fiber pull-out. Totally different interactions between fiber and matrix were found compared to borides and carbides. Although the suitable conditions for effective load transfer, i.e. with matrix possessing lower Young's modulus than the fiber, no notable fracture increase was measured, owing to the negative contribution of residual stress arising from too different coefficient of thermal expansion of fiber and matrix.

References

- 1 Technical report: L. Silvestroni, D. Sciti, "Characterization of Ultra High Temperature Ceramics via Transmission Electron Microscopy. ZrB₂ and HfB₂ composites containing Hi-Nicalon SiC fibers", Technical report for The Air Force Office of Research and Development FA8655-12-1-3004, TR-2012/88, December 2012.
- 2 D.G. Munz, J.L.Jr. Shannon, R.T. Bubsey, "Fracture toughness calculations from maximum load in four point bend tests of chevron notch specimens", *Int. J. Fract.* 16 (1980) R137-141.
- 3 W. C. Oliver, G. M. Pharr, "An improvement technique for determining hardness and elastic modulus using load and displacement sensing indentation experiments", *J. Mater. Res.*, 7 [6] 1564-82 (1992).
- 4 "Part 2: Data Reviews, Section I: High Alumina Ceramics," R. Morrell, *Handbook of Properties of Technical and Engineering Ceramics*, Vol. 2, pp. 13-35 (1987), published by Her Majesty's Stationery Office (London).
- 5 R. Stevens, "Engineering Properties of Zirconia", in *Engineered Materials Handbook*, Vol. 4, pp. 775-786 (1991), edited by S.J. Schneider, Jr., published by ASM International.
- 6 M. Takeda, J. Sakamoto, A. Saeki, H. Ichikawa, in: *Ceramic Engineering and Science Proceedings* vol. 17, No. 4 (American Ceramic Society, Westerville, OH, 1996) p. 35.E.
- 7 Wuchina, M. Opeka, S. Causey, K. Buesking, J. Spain, A. Cull, J. Routbort, F. Gutierrez-Mora, "Designing for ultrahigh-temperature applications: The mechanical and thermal properties of HfB₂, HfC_x, HfN_x and α Hf(N)", *J. Mater. Sci.* 39 (2004) 5939-5949.
- 8 A.L. Chamberlain, W.G. Fahrenholtz, G.E. Hilmas, D.T. Ellerby, "High Strength ZrB₂-Based Ceramics", *J. Am. Ceram. Soc.* 87 (2004) 1170-1172.
- 9 W.W. Wu, Y. Sakka, M. Estili, T.S. Suzuki, T. Nishimura, G.J. Zhang, "Microstructure and high-temperature strength of textured and non-textured ZrB₂ ceramics", *Sci. and Techn. Adv. Mater.* 15 (2014) 014202.
- 10 D. Sciti, L. Silvestroni, C. Melandri, G. Celotti, S. Guicciardi, "Sintering and mechanical properties of ZrB₂-TaSi₂ and HfB₂-TaSi₂ ceramic composites", *J. Am. Ceram. Soc.* 91 (2008) 3285-3291.
- 11 J. Zou, G.J. Zhang, C.F. Hu, T. Nishimura, Y. Sakka, J. Vleugels, O. Van der Biest, "Strong ZrB₂-SiC-WC Ceramics at 1600°C", *J. Am. Ceram. Soc.* 95 (2012) 874-878.
- 12 S.C. Zhang, G.E. Hilmas, W.G. Fahrenholtz, "Improved oxidation resistance of zirconium diboride by tungsten carbide additions", *J. Am. Ceram. Soc.* 91 (2008) 3530-3535.
- 13 M. Kazemzadeh Dehdashti, W.G. Fahrenholtz, G.E. Hilmas, "Effects of temperature and the incorporation of W on the oxidation of ZrB₂ ceramics", *Corr. Sci.* 80 (2014) 221-228.
- 14 D.G. Barton, S.L. Soled, G.D. Meitzner, G.A. Fuentes, E. Iglesia, "Structural and Catalytic Characterization of Solid Acids Based on Zirconia Modified by Tungsten Oxide", *J. Catalysis* 181 (1999) 57-72.
- 15 G. Sauthoff, *Intermetallics*. Weinheim, New York: VCH Publishers, 1995, p. 115.
- 16 L. Silvestroni, D. Sciti, "Effect of transition metal silicides on microstructure and mechanical properties of ultra-high temperature ceramics", in: J. Low, Y. Sakka, C. Hu (Eds.), *MAX Phases and Ultra-High Temperature Ceramics for Extreme Environments*, IGI Global, Hershey (PA), 2013, pp. 125-179.
- 17 D. Sciti, L. Silvestroni, V. Medri, F. Monteverde, Chapter 6: "Sintering and densification of ultra-high temperature ceramics" in "Ultra-High Temperature Ceramics: Materials for Extreme Environment Applications", Ed. by W. G. Fahrenholtz, E. J. Wuchina, W. E. Lee and Y. Zhou, Wiley, Inc., ISBN 0-471-9781118700785, in press (2014).
- 18 H. Pastor, R. Meyer, "An investigation of the effect of additions of metal silicides on titanium and zirconium borides from the point of view of their sintering behavior and their resistance to oxidation at high temperature", *Rev. Int. Haut. Temp. Refract.* 2 (1974) 41-54.
- 19 Z. Guo, W. Yuan, Y. Sun, Z. Cai, Z. Qiao, "Thermodynamic Assessment of the Si-Ta and Si-W Systems", *J. Phase Equilib. Diff.* 30 (2009) 564-570.
- 20 E. Rudy, "Experimental phase equilibria of selected binary, ternary, and higher order systems, part V. The phase diagram W-B-C". AFML-TR-69-117 (1969).
- 21 L.Y. Chang, M.G. Scroger, B. Phillips, "Condensed Phase Relations in the Systems ZrO₂-WO₂-WO₃ and HfO₂-WO₂-WO₃", *J. Am. Ceram. Soc.* 50 (1967) 211-215.
- 22 J. Zou, G.J. Zhang, Y.M. Kan, "Formation of tough interlocking microstructure in ZrB₂-SiC-based ultrahigh-temperature ceramics by pressureless sintering", *J. Mater. Res.* 24 (2009) 2428-2434.
- 23 F.F. Lange, "Compressive surface stresses developed in ceramics by an oxidation-induced phase-change", *J. Am. Ceram. Soc.* 63 (1980) 38-40.
- 24 A.G. Evans, A. Rana, "High temperature failure mechanisms in ceramics", *Acta Metall.* 28 (1979) 128-141.
- 25 A. Rezaie, W.G. Fahrenholtz, G.E. Hilmas, "Evolution of Structure During the Oxidation of Zirconium Diboride – Silicon Carbide in Air up to 1500°C", *J. Eur. Ceram. Soc.* 27 (2007) 2495-2501.
- 26 S.N. Karlsdottir, J.W. Halloran, "Oxidation of ZrB₂-SiC: influence of SiC content on solid and liquid oxide phase formation", *J. Am. Ceram. Soc.* 92 (2009) 481-486.
- 27 C.M. Carney, T.A. Parthasarathy, M.K. Cinibulk, "Oxidation Resistance of Hafnium Diboride Ceramics with Additions of Silicon Carbide and tungsten boride or tungsten carbide", *J. Am. Ceram. Soc.* 94 (2011) 2600-2607.
- 28 Technical report: L. Silvestroni, D. Sciti, "Characterization of Ultra High Temperature Ceramics via Transmission Electron Microscopy. ZrB₂ composites containing different kinds of fibers". Technical report for The Air Force Office of Research and Development FA8655-12-1-3004, RT-2013/105, December 2013.
- 29 B.J. Lai, J.L. Watts, G.E. Hilmas, W.G. Fahrenholtz, "Development of Novel Processing Methods for Next Generation Ultra-High Temperature ZrB₂-SiC Fiber Reinforced Composites", 37th International Conference and Expo on Advanced Ceramics and Composites, 2013.

30 L. Pienti, D. Sciti, L. Silvestroni, S. Guicciardi, "Effect of milling on the mechanical properties of chopped SiC fiber-reinforced ZrB₂", Materials, 6, 1980-1993 (2013), doi:10.3390/ma6051980.

31 L. Silvestroni, E. Landi, K. Bejtka, A. Chiodoni, D. Sciti, "Oxidation and kinetic of ZrB₂ containing chopped SiC fibers", submitted to Corrosion.

32 Ishikawa T. "Advances in Inorganic fibers", Adv Polym Sci 2005;178:109-44.

33 L. Silvestroni, D. Sciti, C. Melandri, S. Guicciardi, "Tyranno SA3 fiber - ZrB₂ composites Part II: mechanical Properties", Materials & Design, 65, 1253-1263 (2015).

34 J.A. DiCarlo, H.M. Yun, "Non-oxide (Silicon Carbide) Fibers", in Handbook of ceramic Composites, Ed. by N.P. Bansal, 2005.

35 K. Xia, T. G. Langdon, "The toughening and strengthening of ceramic materials through discontinuous reinforcement", J. Mat. Sci., 29 5219-5231 (1994).

36 W. Krenkel, "Ceramic Matrix Composites: Fiber Reinforced Ceramics and their Applications". Wiley-VCH Verlag GmbH & Co. KGaA, Weinheim, Germany, 2008.

37 Pierson HO, "Handbook of refractory carbides and nitrides". Norwich, NY: William Andrew publishing, 2001.

38 Johnston JR, Signorelli RA, Freche JC, "Performances of rocket nozzle material with several solid propellants", NASA technical note / D: 3428, National Aeronautics and Space Administration, 1966.

39 Dashora A, Ahuja BL. Electronic structure, "Compton profiles and optical properties of TaC and TaN", Radiat Phys Chem 2010;79(11):1103-10.

40 Liu L, Ye F, Zhang Z, Zhou Y, "Microstructure and mechanical properties of the spark plasma sintered TaC/SiC composites", Mat Sci and Eng 2011;A529:479-84.

41 Sciti D, Silvestroni L, Medri V, Guicciardi S. "Pressureless sintered in-situ toughened ZrB₂-SiC ceramics", J Europ Ceram Soc 2011;31(12):2145-53.

42 Silvestroni L, Sciti D. "Sintering Behavior, Microstructure, and Mechanical Properties: A Comparison among Pressureless Sintered Ultra-Refractory Carbides", Adv Mater Sci and Eng. doi:10.1155/2010/835018.

43 Tilly DJ, Löfvander JPA, Levi CG. "Solidification Paths and Carbide Morphologies in Melt-Processed MoSi₂ -SiC In Situ Composites", Metall and Mater Trans A 1197;28A:1889-900.

44 Xu H, Bhatia T, Deshpande SA, Padture NP, Ortiz AL, Cumblera FL. "Microstructural Evolution in Liquid-Phase-Sintered SiC: Part I, Effect of Starting Powder", J Am Ceram Soc 2001;84(7):1578-84.

45 Silicon Carbide Ceramics – 1 Fundamental and solid reaction. Ed. by S. Sōmiya, Y. Inomata, ceramic research and development in Japan, Elsevier Science Publisher Co. Inc. , New York (1991).

46 Ortiz AL, Bhatia T, Padture NP, Pezzotti G. "Microstructural Evolution in Liquid-Phase-Sintered SiC: Part III, Effect of Nitrogen-Gas Sintering Atmosphere", J Am Ceram Soc 2002;85(7):1835-40.

47 Ghosh D, Subhash G, Orlovskaya N. "Measurement of scratch-induced residual stress within SiC Grains in ZrB₂-SiC composite using micro-Raman spectroscopy", Acta Mater 2008;56(18):5345-54.

48 Watts J, Hilmas GE, Fahrenholtz WG, Brown D, ClausenB. "Measurement of thermal residual stresses in ZrB₂ -SiC composites", J Europ Ceram Soc 2011;31(9):1811-20.

49 Holleck H. "Material Selection for Hard Coatings", J Vacuum Sci and Techn A 1986;4(6):2661-9.

50 Li Z, Bradt RC. "Thermal Expansion of the Hexagonal (6H) Polytype of Silicon Carbide", J Am Ceram Soc 1986;69(12):863-6.

51 Rogers KF, Kingston-Lee DM, Phillips LN, Yates B, Chandra M, Parker SFH. "The thermal expansion of carbon-fibre reinforced plastics", J Mater Sci 1981;16(10): 2803-18.

52 Taya M, Hayashi S, Kobayashi AS, Yoon HS. "Toughening of a Particulate Ceramic-Matrix Composite by Thermal Residual Stress", J Am Ceram Soc 1990;73:1382-91.

53 Verkhorobin LF, Matyushenko NN. "The thermal expansion of disilicides of some transition metals", Soviet Powder Metall and Metal Ceram 1963;2(6):468-9.

List of Symbols, Abbreviations and Acronyms

UHTC: ultra-high temperature ceramic

SEM: Scanning electron microscopy

TEM: Transmission electron microscopy

STEM: Scanning transmission electron microscopy

EDS: energy dispersive spectroscopy

ZZ: $\text{ZrB}_2 + \text{ZrSi}_2$

ZZ-HN: $\text{ZrB}_2 + \text{ZrSi}_2 + \text{SiC}_{\text{Hi-Nicalon}}$

ZZ-T: $\text{ZrB}_2 + \text{ZrSi}_2 + \text{SiC}_{\text{Tyranno SA3}}$

ZZ-iHN: $\text{ZrB}_2 + \text{ZrSi}_2 + \text{SiC}_{\text{B(Si)N - Hi-Nicalon S}}$

ZZ-TZ: $\text{ZrB}_2 + \text{ZrSi}_2 + \text{SiC}_{\text{Tyranno ZMI}}$

ZS: $\text{ZrB}_2 + \text{Si}_3\text{N}_4$

ZS-HN: $\text{ZrB}_2 + \text{Si}_3\text{N}_4 + \text{SiC}_{\text{Hi-Nicalon}}$

ZS-T: $\text{ZrB}_2 + \text{Si}_3\text{N}_4 + \text{SiC}_{\text{Tyranno SA3}}$

ZS-iHN: $\text{ZrB}_2 + \text{Si}_3\text{N}_4 + \text{SiC}_{\text{B(Si)N - Hi-Nicalon S}}$

ZS-C: $\text{ZrB}_2 + \text{Si}_3\text{N}_4 + \text{C}_{\text{fiber}}$

ZT: $\text{ZrB}_2 + \text{TaSi}_2$

ZT-T: $\text{ZrB}_2 + \text{TaSi}_2 + \text{SiC}_{\text{Tyranno SA3}}$

T: TaC

TS: $\text{TaC} + \text{Si}_3\text{N}_4$

TS-S: $\text{TaC} + \text{Si}_3\text{N}_4 + \text{SiC}_{\text{particle}}$

TT: $\text{TaC} + \text{TaSi}_2$

TM-S: $\text{TaC} + \text{MoSi}_2 + \text{SiC}_{\text{particle}}$

TT-HN: $\text{TaC} + \text{TaSi}_2 + \text{SiC}_{\text{Hi-Nicalon}}$

TT-T: $\text{TaC} + \text{TaSi}_2 + \text{SiC}_{\text{Tyranno SA3}}$

TS-C: $\text{TaC} + \text{Si}_3\text{N}_4 + \text{C}_{\text{fiber}}$

AO: $\text{Al}_2\text{O}_3 + \text{SiC}_{\text{Hi-Nicalon}}$

ZO: $\text{ZrO}_2 + \text{SiC}_{\text{Hi-Nicalon}}$

Disclaimer

The results presented in this technical report are referred exclusively to the samples and to the specified procedures herein described. Any extrapolation or extension to other samples or other procedures is beyond the scope of this document.